

ABSTRACT

Title of dissertation: WAVE PROPAGATION IN RODS,
SHELLS, AND ROTATING SHAFTS
WITH NON-UNIFORM GEOMETRY

Mario Toso, Doctor of Philosophy, 2004

Dissertation directed by: Professor Amr Baz
Department of Mechanical Engineering

The propagation of waves in rods, shells and rotating shafts with variable thickness is studied through numerical models and experimental measurements. All numerical models are formulated using the Transfer Matrix approach, which accurately reproduces the dynamic behavior and wave propagation characteristics of the considered structures at each frequency. The numerical predictions show that exponential and linear thickness profiles generate a cut-off frequency, below which waves do not propagate along the structure. Hence, the considered rods and shells are capable of filtering out low frequency and they behave as high-pass mechanical filters. The filtering capabilities of the considered class of rods and shells are investigated for different types of profiles. Furthermore, the effect introduced by using periodicity and changing the material properties of the structure in a functionally graded manner is investigated.

The effect of linear profiles is practically evaluated by determining both the frequency and time response for excitations applied at one side of the structure. These results are compared to uniform profiles through the Wavelet Transform (WT), which visualizes the structure vibrational energy simultaneously in both the time and frequency domain. The agreement between the theoretical and experimental results validates the numerical models and demonstrates the effectiveness of the proposed design configurations in attenuating the propagation of waves especially in the low-frequency range.

The filtering characteristics are also investigated for rotating shafts with tapered and stepped geometry. It is found out that rotation at a constant speed does not significantly modify the flexural wave propagation characteristics of the system. Also, the interest is extended to studying the Campbell diagrams of tapered and periodically stepped profiles. Experiments on the propagation of vibration from a gearbox through rotating shafts prove that tapered and periodic profiles can effectively redistribute the energy spectrum by confining the propagation to specific frequency bands. Such characteristics become more evident when the shaft is provided with active periodic piezoelectric inserts.

The effectiveness of the constant axial loads and feedback control on the shaft performance is determined and compared to the alternative passive periodic treatments.

WAVE PROPAGATION IN RODS, SHELLS, AND ROTATING SHAFTS
WITH NON-UNIFORM GEOMETRY

by

Mario Toso

Dissertation submitted to the Faculty of the Graduate School of the
University of Maryland, College Park in partial fulfillment
of the requirements for the degree of
Doctor of Philosophy
2004

Advisory Committee:

Professor A. Baz, Chair
Professor B. Balachandran
Associate Professor D. Pines
Associate Professor D. DeVoe
Assistant Professor D. Robbins, Jr.

©Copyright by

Mario Toso

2004

DEDICATION

To the memory of my dearest professor,
Bruno Aristide Domenico Piombo.

ACKNOWLEDGEMENTS

First of all, I want to thank my parents, for being the most important people in my life and for letting me choose my way, always, even when it took me so far from Home.

My sincere gratitude goes to my advisor, Prof. Amr Baz, for his patience and his continuous support during these four years at University of Maryland. I am grateful to Prof. Massimo Ruzzene, for being a true friend and a superlative teacher.

Many thanks to all my colleagues at the SMSRC and the Vibration lab, for the competent discussions and moral support.

Finally, I would like to send a big hug to all the people I was lucky enough to meet during my staying, for all the good times, the laughs and the cheerful weekends.

TABLE OF CONTENTS

LIST OF TABLES.....	vi
LIST OF FIGURES	vii
NOMENCLATURE	xii
CHAPTER 1: INTRODUCTION AND OBJECTIVES	1
CHAPTER 2: WAVE PROPAGATION IN TAPERED RODS	5
2.1 Introduction.....	5
2.2 Equation Of Motion Of Rods With Variable Cross Section.....	6
2.3 Numerical Examples.....	9
2.3.1 Exponential Profile	9
2.3.2 Polynomial Profile	16
2.4 Experimental Characteristics Of Tapered Rods.....	22
2.5 Conclusions.....	27
CHAPTER 3: WAVE PROPAGATION IN PERIODIC SHELLS WITH TAPERED WALL THICKNESS AND CHANGING MATERIAL PROPERTIES	28
3.1 Introduction.....	28
3.2 Equation Of Motion For Shells Of Variable Material Properties And Geometry.....	31
3.3 Numerical Examples.....	39
3.3.1 Geometrically Tapered Profiles	40
3.3.1.1 Exponential Profile	41
3.3.1.2 Polynomial Profile	44
3.3.2 Functionally Graded Materials	48
3.3.2.1 FGM Effect: Exponential Grading.....	48
3.3.2.2 FGM Effect: Linear Grading	50
3.3.3 Combined Effect.....	52
3.4 Experimental Characteristics of Shells with Varying Geometry.....	55
3.5 Periodic Shells with Tapered Elements	58
3.6 Conclusions.....	63

CHAPTER 4: WAVE PROPAGATION IN PERIODIC ROTATING SHAFTS WITH DIFFERENT GEOMETRIES	64
4.1 Introduction.....	64
4.2 Lateral Shaft Problems.....	67
4.2.1 The disk.....	68
4.2.2 The shaft.....	69
4.2.3 Bearings and seals.....	69
4.2.4 Mass unbalance.....	70
4.3 Equations of Motion	70
4.4 Campbell Diagrams	74
4.5 Finite Element Formulation.....	76
4.5.1 Transfer Matrix	77
4.5.2 Campbell Diagram.....	79
4.6 Numerical Results.....	79
4.6.1 Tapered Shaft.....	80
4.6.2 Periodically Stepped Shaft.....	83
4.6.3 Optimized Geometry: Combined Effect	86
4.7 Experimental Results.....	88
4.7.1 Tapered Shaft.....	88
4.7.2 Periodically Stepped Shaft.....	91
4.8 Alternative Optimization: Effect of Viscoelastic Inserts.....	95
4.9 Conclusions.....	104
 CHAPTER 5: ACTIVE CONTROL OF PERIODIC SHAFTS.....	 105
5.1 Introduction.....	105
5.2 Characteristics of periodic shafts with piezoelectric actuators.....	106
5.2.1 Characteristics of the piezoelectric actuators.....	107
5.3 Numerical results.....	109
5.4 Experimental results	117
5.5 Comparisons between theory and experiments	124
5.6 Conclusions.....	128
 CHAPTER 6: SUMMARY AND RECOMMENDATIONS.....	 129
6.1 Summary.....	129
6.2 Recommendations.....	131
 APPENDIX A1: The Wavelet Transform	 132
 REFERENCES	 135

LIST OF TABLES

Table 2.1	PVC Rod Properties.....	11
Table 2.2	PVC Rod Properties.....	17
Table 2.3	PVC Prismatic Rod Properties.....	20
Table 3.1	PVC Shell Properties.	40
Table 3.2	Periodic Tapered Elements.	58
Table 4.1	Tapered Shaft Properties.....	81
Table 4.2	Periodic Shaft Properties.....	84
Table 4.3	Neoprene Properties.....	95
Table 5.1	Piezo-actuator PCB 712A02 data sheet.	108

LIST OF FIGURES

Figure 2.1:	Generic rod element.....	6
Figure 2.2:	Dispersion relation $k=k(\omega)$ for longitudinal wave in uniform rods (thin line) and tapered rods (thick line).....	12
Figure 2.3:	Propagation Constants α_i and β_i for uniform rods (thin line) and tapered rods (thick line).	13
Figure 2.4:	Rod aspect for different profiles.	14
Figure 2.5:	Propagation parameter $\mu=\alpha+i\beta$ and <i>cut-off frequency</i>	15
Figure 2.6:	Transmitted force: F_L/F_0	16
Figure 2.7:	Propagation constants $\mu=\alpha+i\beta$ and <i>cut-off frequency</i>	18
Figure 2.8:	Transmitted force: F_L/F_0	19
Figure 2.9:	Frequency response.....	21
Figure 2.10:	Frequency response and Wavelet transform of rods: (a) uniform thickness and (b) tapered profile.	22
Figure 2.11:	Tapered rod.	23
Figure 2.12:	Spectrum Analyzer.....	23
Figure 2.13:	Time history and wavelet transform of the response of a uniform rod: (a) full picture and (b) truncated wave	25
Figure 2.14:	Time history and wavelet transform of the response of a tapered rod: (a) full picture and (b) truncated wave	26
Figure 3.1:	Three-dimensional cylindrical shell.....	32
Figure 3.2:	Section of exponential-tapered shell.....	41
Figure 3.3:	Propagation constants of uniform (dash) and tapered (solid) shells: (a) longitudinal direction and (b) radial direction.....	43
Figure 3.4:	Cross-section of a linearly tapered shells.....	44

Figure 3.5:	Propagation constants of uniform (dash) and tapered (solid) shells: (a) longitudinal direction and (b) radial direction.....	46
Figure 3.6:	Frequency response and Wavelet Transform: (a) uniform thickness and (b) tapered profile.	47
Figure 3.7:	Propagation constants of uniform (dash) and exponential FGM (solid) shells: (a) longitudinal and (b) radial direction.....	50
Figure 3.8:	Propagation constants of shells with linearly varying Young's modulus: (a) longitudinal direction and (b) radial direction.	52
Figure 3.9:	Frequency response: (dash) uniform thickness, (solid) same slope, (dot) opposite slope.	54
Figure 3.10:	(a) uniform shell and (b) tapered shell.	55
Figure 3.11:	Experimental Time Response and Wavelet Transform of shells: (a) uniform thickness and (b) tapered profile.	57
Figure 3.12:	Propagation characteristics of a periodic tapered shell type (A).	59
Figure 3.13:	Transmitted force: type (A) tapered shell (solid) and uniform shell (dashed).	59
Figure 3.14:	Propagation characteristics of a periodic tapered shell type (B).....	60
Figure 3.15:	Transmitted force: type (B) tapered shell (solid) and uniform shell (dashed).	61
Figure 3.16:	Propagation characteristics of a periodic tapered shell type (C).....	62
Figure 3.17:	Transmitted force: type (C) tapered shell (solid) and uniform shell (dashed).	62
Figure 4.1:	Sketch of a complete rotor.	67
Figure 4.2:	Sketch of a periodic, uniform and tapered shaft.	70
Figure 4.3:	Schematic drawing of the tapered and uniform shaft.	81
Figure 4.4:	Propagation Constants: tapered profile (solid) and uniform profile (dash).	82
Figure 4.5:	Campbell Diagram of a tapered profile (solid line) and uniform profile (dash line).	83
Figure 4.6:	Schematic drawing of the stepped and uniform shafts.	84

Figure 4.7:	Propagation Constants: periodic profile (solid) and uniform profile (dash).....	85
Figure 4.8:	Sketch of the stepped profile and the stepped-tapered profile.....	86
Figure 4.9:	Propagation Constants with length mismatch: stepped-tapered profile (solid) versus stepped profile (dash).....	87
Figure 4.10a:	Experimental setup.....	89
Figure 4.10b:	Power Amplifier and Spectrum Analyzer.....	89
Figure 4.11:	Non-rotating shaft: frequency response of the tapered profile (solid) and uniform profile (dash).....	90
Figure 4.12:	Rotating shaft: Frequency response of the tapered profile (solid) and uniform profile (dash).....	91
Figure 4.13:	Experimental setup for the stepped and uniform shaft.....	92
Figure 4.14:	Non-rotating shaft: Frequency response of the periodic profile (solid) and uniform profile (dash).....	93
Figure 4.15:	Rotating shaft: Frequency response of the periodic profile (solid) and uniform profile (dash).....	94
Figure 4.16:	Experimental setup of the shaft with free-free boundary conditions.....	96
Figure 4.17:	Broadband frequency response and propagation characteristics of the non-rotating uniform shaft (dash), stepped periodic shaft (thin solid) and rubber-coated shaft (thick solid).....	97
Figure 4.18:	The rubber-coated rotor and the experimental setup for the rotating case.....	99
Figure 4.19:	Rotating shaft: Frequency response of the periodic profile (solid) and uniform profile (dash).....	100
Figure 4.20:	Attenuation factor and Average Power Spectrum of the rotating uniform shaft (dash), stepped periodic shaft (thin solid) and rubber-coated shaft (thick solid).....	101
Figure 4.21:	Wavelet Transform of the power density for the uniform shaft.....	102
Figure 4.22:	Wavelet Transform of the power density for the stepped shaft.....	102
Figure 4.23:	Wavelet Transform of the power density for the coated shaft.....	103

Figure 5.1:	Schematic drawing of the active shaft assembly.	106
Figure 5.2:	Piezoelectric actuator PCB Piezotronics Model 712A02.	108
Figure 5.3:	Actuator output force characteristics.	109
Figure 5.4:	Frequency response and Campbell diagram for a uniform shaft (thin) and the passive periodic shaft (thick).	110
Figure 5.5:	Frequency response and Campbell diagram for the active periodic shaft: compressive load (thin), tensile load (thick) at input location.	112
Figure 5.6:	Frequency response and Campbell diagram for the active periodic shaft: compressive load (thin), tensile load (thick) at midspan location.	113
Figure 5.7:	Frequency response and Campbell diagram for the active periodic shaft: compressive load (thin), tensile load (thick) at output location.	114
Figure 5.8:	Frequency response and Campbell diagram for the active periodic shaft: compressive load (thin), tensile load (thick) at all locations.	115
Figure 5.9:	Propagation coefficients for the active periodic shaft.	116
Figure 5.10:	Propagation coefficients for the passive periodic shaft.	117
Figure 5.11a:	Experiment setup.	118
Figure 5.11b:	Spectrum analyzer and active controller.	118
Figure 5.12:	Experimental frequency response and propagation coefficients of the passive periodic shaft.	120
Figure 5.13:	Experimental frequency response and propagation coefficients of the active periodic shaft.	121
Figure 5.14:	Control gain for the active shaft: piezo-actuator at input position.	122
Figure 5.15:	Control gain for the active shaft: piezo-actuator at midspan position.	123
Figure 5.16:	Control gain for the active shaft: piezo-actuator at output position.	123

Figure 5.17:	Experimental frequency response for the passive shaft (thin) and active shaft (thick): piezo-actuator at input position.....	124
Figure 5.18:	Theoretical frequency response for the passive shaft (thin) and active shaft (thick): piezo-actuator at input position.....	125
Figure 5.19:	Theoretical frequency response for the passive shaft (thin) and active shaft (thick): piezo-actuator at midspan position.	126
Figure 5.20:	Theoretical frequency response for the passive shaft (thin) and active shaft (thick): piezo-actuator at output position.....	127

NOMENCLATURE

A	Area
\mathbf{A}	State-space matrix
c	Characteristic wave speed
C^D	Piezo-actuator elastic modulus
D_o	Outer diameter
D_p	Electrical displacement of the piezo-actuator
D_t	Transverse elastic coefficient
E	Young's modulus of elasticity
E_p	Electrical field intensity of the piezo-actuator
F_0	Longitudinal force at the input location
F_p	Piezo-actuator longitudinal force
\mathbf{G}	Transformation matrix
g, q	Longitudinal and transverse rigidity
h	Shell thickness
h_p	Electro-mechanical coupling factor
\mathbf{I}	Identity Matrix
k	Wave number
K_t	Longitudinal elastic coefficient
M	Bending moment
m_b, m_D	Element bending and electric mass matrices, respectively
N	Longitudinal traction force
Q	Shear force
Q_p	Electrical charge
R, r	Shell radius
T	Kinetic energy
\mathbf{T}	Transfer matrix
T_p	Stress in piezo actuator
U	Potential energy
U, u	Longitudinal displacement
V	Volume
V, W, v, w	Transverse displacement
V_p	Applied voltage
W	External work
w_b, w_D	Nodal transverse and electric displacements, respectively
Y	Displacement vector
Z	State-space vector
ϑ	Angular coordinate
Λ	Eigenvalues matrix of the transfer matrix

α	Propagation constant amplitude
β	Propagation constant phase angle
$\partial(\cdot)$	Partial derivative
$\delta(\cdot)$	First variation
ε	Strain
ε^s	Electrical permittivity
γ	Shear strain
μ	Propagation constant
ρ	Mass density
σ	Stress
ν	Poisson's ratio
ω, Ω	Frequency
 <i>Subscripts</i>	
0	At location 0
D	Related to electric degrees of freedom
L	At location L
N	N elements
r, ϑ	In the r, ϑ direction
u	Relative to the uniform profile
$,x$	Derivative in the x-direction
$,y$	Derivative in the y-direction
$x y z$	Along the x, y, z directions, respectively
 <i>Superscripts</i>	
T	Matrix transpose
-1	Matrix inverse

CHAPTER 1: INTRODUCTION AND OBJECTIVES

The purpose of this work is to establish guidelines for controlling the wave propagation characteristics of rods, axial symmetric shells and rotating shafts, through proper design of their geometrical and material properties.

An interesting way to address the issue of shaping the wave propagation characteristics of the structure is by using *Functionally Graded Materials*. These materials allow for gradually varying the Young's modulus of the structure in a given direction, which changes the characteristic speed of sound in the material. Longitudinal compressional waves can be taken as a simple example. In the case that the Young's modulus of each section of the waveguide increases, also the propagating speed of the compressional wave increases as well, so that each sinusoidal component of the disturbance is shifted to higher frequencies. Depending on the section area and on the length of the waveguide, it is evident at this point that the waves with low frequencies will virtually disappear at the end tip of the waveguide, because they were shifted to higher frequencies.

Changing the geometry of the waveguide is another way to modify the propagation of waves inside the structure. The effect of stepped and tapered profiles can be investigated and compared to the behavior of uniform profiles. As an example, the same longitudinal compressional wave is considered at this point. In the case of a uniform rod, the characteristic speed of the wave and the section area do not change so

every frequency travels undisturbed along the waveguide. When a step is created in the section area, then a free body diagram can show how only in the inner core is still present a pure compressional wave while the outer part of the bigger section is subject to shear deformation. This implies that the compressional wave entering the bigger section creates an additional shear wave that absorbs part of the energy carried by the compressional wave. Hence, at the end tip of the bigger section, only a portion of the compressional wave is transmitted and it is clear that depending on the length and section ratio such wave can completely disappear from the spectrum.

In fact, it is generally understood that conical geometry acts as a natural mechanical high-pass filter for longitudinal waves [11 and 15]. They introduce the idea of *stop-bands* (as the set of frequencies where attenuation occurs) and *pass-bands* where propagation is not obstructed. The study of stepped profiles belongs to the more general field of research of *periodic structures*. For example, Brillouin [7] investigated the effect of periodicity on the propagation spectrum of crystals and electronic components; while other authors (Mead [32 and 33], Orris *et al.* [38], Roy and Plunkett [42]) focused on the property of periodic structures to act as mechanical broadband filters by redistributing the vibrational energy away from the particular regions of frequencies. Recent developments that expand the interest on periodic structures to the application of active control can be found in the works of Ruzzene *et al.* [43], and Baz [6].

In the case of helicopter design, one of the key problems is minimizing the vibration transmission levels generated by the gearbox-engine assembly. besides meeting all strict operational requirements, new designs must prove to be effective in increasing the crew comfort, improving the fatigue life of the structures, and extending flight

envelope. Works in this field traditionally concentrate on the helicopter frame and struts ([3], [35], [45], [48]), but they also recently focus on the tail rotor and transmission shaft as well [41].

In this work, the idea of periodicity is combined with the variable geometry and material properties, innovative damping coatings and active control in order to drastically improve the wave propagation characteristics of rods, shells and rotating shafts by optimizing the bandwidth and amplitude of the stop-bands.

After deriving the analytical model for the equation of motion from the balance of mechanical energy using Hamilton's Principle, solutions to the homogeneous system of equations are calculated by integrating the state matrix along the length of the structure. A coordinate transformation puts the system into the transfer matrix configuration. The eigenvalues of this matrix give a fundamental insight into the propagation characteristics of waves along the structure. These characteristics are discussed in details in order to discern what advantages tapered geometry can introduce. Furthermore, the predictions of the mathematical models are validated through experimental comparisons with prototypes of the structures. Finally, the effect of having different combinations of periodic and tapered elements is investigated.

The present dissertation is organized as follows. A general introduction has been given in this first chapter. In the second chapter, the wave propagation in one-dimensional rods is presented. The equations of motion and the "Transfer Matrix" are derived by using Hamilton's principle and a numerical solution for the wave propagation constants is given for different tapered geometries. The theoretical characteristics of longitudinal waves, generated by exponential and polynomial profiles, are compared to

those developed in uniform rods. Then, experiments are performed on a linearly tapered rod and its characteristics are compared with the numerical model by using the Wavelet Transform method.

In chapter three, the study is extended to axis-symmetric shells. Polynomial and exponential tapered profiles are investigated. Longitudinal and radial waves characteristics are discussed in comparison with corresponding characteristics of uniform cylinders of equivalent mass. Shells with functionally graded material properties (FGM) are also taken into consideration. An optimization process is attempted by combining the effect of tapered profiles with FGM or periodicity. Finally, the numerical predictions are confirmed with experiments on linearly tapered shells.

The problem of rotordynamics is addressed in the forth and fifth chapters. In chapter four, the focus is on different passive treatments, while the fifth chapter concentrates on actively applying additional control forces through piezoelectric actuators. Besides investigating how rotation modifies the flexural wave characteristics of shafts, the interest is extended to the comparison of the Campbell diagrams of tapered, stepped and uniform profiles. Periodicity as well as complex geometries are mixed together in order to improve the attenuation bandwidth and shift the stop bands to more convenient frequencies. Experiments on the propagation of the vibration of engine-gearbox demonstrate the effectiveness of tapered and periodic profiles with or without additional passive damping coating treatments. Additional experiments on a stepped active shaft prove the effectiveness of active control in attenuating the wave propagation as compared to various passive treatments. The contributions of this dissertation and suggestions for future work are summarized in the sixth chapter.

CHAPTER 2: WAVE PROPAGATION IN TAPERED RODS

2.1 Introduction

The vibration of non-uniform rods and beams is a subject of considerable scientific and practical interest because of its relevance to many structural, mechanical, and aeronautical engineering applications.

Closed-form solutions for conical rods and beams can be found in classic vibration books [15 and 22]. Also, Doyle [11] considered a spectral finite element formulation of the dynamics of viscoelastic, tapered rods. It was shown that the spectral formulation can model distributed mass more efficiently than a traditional finite element model formulation. Eisenberger [12] demonstrated that the natural frequencies are only slightly affected by the taper and that the equation of motion of rods with conical cross section can be reduced to the form of a wave equation by a mere variable transformation. Lau [27], Abrate [1], and Kumar and Sujith [25] investigated all the possible area variations (polynomial, exponential, catenoidal) for which exact analytical solutions for the problem can be obtained with a systematic approach. Bapat [5] combined the closed-form solution for uniformly tapered rods with the transfer matrix method and compared its performance to multi-step approximation and FEM results demonstrating that the transfer matrix solution can be a much more effective approach to the problem. In recent years, Wang [55] derived closed-form solutions for free longitudinal vibration of a rod with exponentially distributed stiffness and mass. Li [30] considered rods, whose mass

distribution is not necessarily assumed to be proportional to the stiffness distribution. Exact or approximate solutions for arbitrary mass-stiffness distributions are pursued.

The present chapter is organized as follows. A literature survey is presented in Section 2.1. In Section 2.2, the equations of motion and the mathematical model is derived for the two most common families of rod profiles, namely, polynomial and exponential profiles. In Section 2.3, an analytical solution is presented for a simple exponential profile in order to understand the concepts of propagation constant, stop bands, and cut-off frequency. Numerical solutions are finally presented for few examples of rod profiles in the same section. In Section 2.4, experiments are conducted on a linearly tapered rod and compared to numerical predictions. In Section 2.5, the conclusions are provided along with the explanations for the benefits of implementing tapered section versus uniform sections.

2.2 Equation Of Motion Of Rods With Variable Cross Section

The equation of equilibrium [15] for a generic rod is (Figure 2.1):

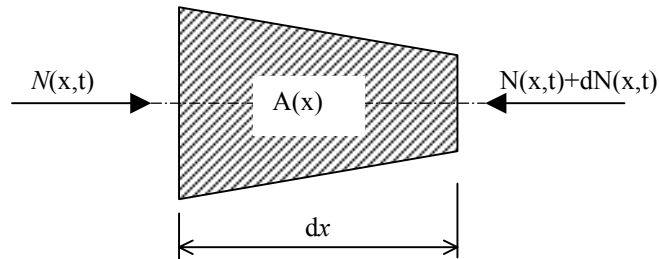


Figure 2.1: Generic rod element.

$$(N(x,t) + \frac{\partial N(x,t)}{\partial x} dx) - N(x,t) = \rho A(x) \frac{\partial^2 u(x,t)}{\partial t^2} \quad (2.1)$$

where $N(x,t) = EA(x) \frac{\partial u(x,t)}{\partial x}$ is the longitudinal force. For harmonic motion, at

frequency ω one obtains the ordinary differential equation:

$$\frac{d^2 u(x)}{dx^2} + \left(\frac{1}{A(x)} \frac{dA(x)}{dx} \right) \frac{du(x)}{dx} + k^2 u(x) = 0 \quad (2.2)$$

where $k = \frac{\omega}{\sqrt{E/\rho}}$ is the wave number. Hence, the equation of motion (2.2) can be cast in

a state-space formulation by defining the state vector $Z = \{u \quad u_{,x}\}^T$:

$$Z_{,x} = \begin{bmatrix} 0 & 1 \\ -k^2 & -\frac{A_{,x}}{A} \end{bmatrix} Z \Leftrightarrow Z_{,x} = \mathbf{A}(x) \cdot Z \quad (2.3)$$

The solution of equation (2.3) is given by:

$$Z(L) = e^{\int_0^L \mathbf{A}(x) dx} Z(0) \quad (2.4)$$

It is well-known that, for a linear elastic structure, the relation between the longitudinal force $N(x,t)$ and the displacement $u(x,t)$, is as follows

$$N(x, t) = EA(x) \frac{\partial u(x, t)}{\partial x} \quad (2.5)$$

Then we can easily compute the transfer matrix \mathbf{T} from

$$Y_L = \left[\mathbf{G}_L e^{\int_0^L \mathbf{A}(x) dx} \mathbf{G}_0^{-1} \right] Y_0 = \mathbf{T} Y_0 \quad (2.6)$$

where the new space vector Y at the two ends of the rod is given by

$$Y_0 = \begin{Bmatrix} u_0 \\ N_0 \end{Bmatrix} = \mathbf{G}_0 Z(0) = \begin{bmatrix} 1 & 0 \\ 0 & -EA(0) \end{bmatrix} \begin{Bmatrix} u(0) \\ u_x(0) \end{Bmatrix},$$

and

$$Y_L = \begin{Bmatrix} u_L \\ N_L \end{Bmatrix} = \mathbf{G}_L Z(L) = \begin{bmatrix} 1 & 0 \\ 0 & EA(L) \end{bmatrix} \begin{Bmatrix} u(L) \\ u_x(L) \end{Bmatrix}$$

The eigenvalues λ_i of the transfer matrix \mathbf{T} provide all the information about the propagation characteristics, that is

$$\lambda_i = e^{\mu_i} = e^{\alpha_i + i\beta_i} = e^{\alpha_i} e^{i\beta_i} \quad (2.7)$$

where μ_i is the *propagation parameter*, α_i and β_i are called the *attenuation factor* and the *phase angle*, respectively; they represent the real and imaginary portion of the propagation constant.

By recalling equations (2.6) and (2.7), each wave component can be written in indicial notation as

$$(Y_L)_i = e^{\alpha_i} (Y_O)_i e^{i\beta_i} \quad (2.8)$$

Equations (2.8) shows that the disturbance measured at location L is shifted in phase by the factor β with respect to the signal measured at location 0 and it is magnified or attenuated by factor α depending on the taper ratio.

In general, it can be stated that, when the phase β shifts 180° , destructive interference occurs between the traveling wave and the reflected wave so that no disturbance can propagate along the rod (STOP BAND). The frequency that sets the boundary of the stop band is called *cut-off frequency*. It will be explained in more details with an example in the next section.

2.3 Numerical Examples

Some examples are presented here for the two most common classes of rod profiles: *exponential profiles* and *polynomial profiles*.

2.3.1 Exponential Profile

The cross section is written as:

$$A(x) = A_0 e^{\frac{a}{L}x} \quad (2.9)$$

where A_0 and a are set constants. In the case of exponential cross section the system matrix \mathbf{A} , given by equation (2.3), does not depend on the variable x , which make all the calculations particularly easy as \mathbf{A} becomes as

$$\mathbf{A} = \begin{bmatrix} 0 & 1 \\ -k^2 & -\frac{a}{L} \end{bmatrix} \quad (2.10)$$

Solutions to the wave equation (2.2) can be written as $u(x) = Ue^{\lambda x}$ [11], where λ are solutions of the characteristic polynomial of \mathbf{A} , such that:

$$\lambda^2 + \frac{a}{L}\lambda + k^2 = 0 \quad (2.11)$$

The roots of (2.11),

$$\lambda_{1,2} = -\frac{a}{2L} \pm i\sqrt{k^2 - \left(\frac{a}{2L}\right)^2} \quad (2.12)$$

are such that:

- when $k^2 < (a/2L)^2$, ($\omega < \omega_c$), the roots are both real, so waves cannot propagate along the rod; this frequency range is called STOP BAND.

- when $k^2 > (a/2L)^2$, ($\omega > \omega_c$) , the roots become complex, so waves will propagate along the rod: PASS BAND.

The frequency ω_c correspondent to the particular wave number that sets the boundary between the two different behaviors, $k = (a/2L)$, is called *cut-off frequency* ,

namely $\omega_c = \frac{a}{2L} \sqrt{\frac{E}{\rho}}$.

The imaginary part of $\lambda_{1,2}$ gives the *Dispersion Relation* : a non-zero imaginary component means the wave is free to travel along the structure.

Consider a rod that has the characteristics listed in Table (2.1).

Table 2.1: PVC Rod Properties.

Parameter	Value
Young Modulus E [Pa]	3.2×10^8
Density ρ [Kg/m³]	1150
Length L [mm]	457.2 (18")
Area A_0 [mm²]	645.16 (2" * 1/2")
Taper parameter a	4

A plot of the wave number k versus the frequency ω quantifies the dispersion characteristics of the rod. Such characteristics are displayed in Figure (2.2) for uniform and tapered rods indicating a cut-off frequency of 2000 Hz for the tapered rod.

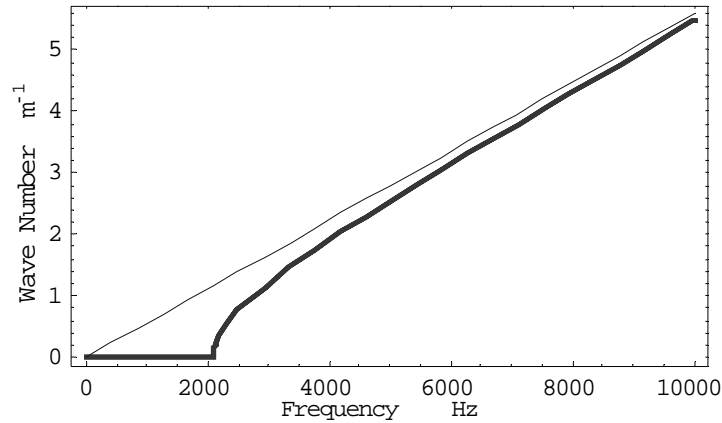


Figure 2.2: Dispersion relation $k=k(\omega)$ for longitudinal wave in uniform rods (thin line) and tapered rods (thick line).

The propagation characteristics of the uniform and tapered rods are obtained from the transfer matrix approach. In Figure (2.3), the propagation and attenuation parameters of both the uniform and tapered rods (α_i and β_i) are displayed. The figure clearly indicates that the propagation parameter α_i for the uniform rod is equal to zero, emphasizing the presence of a pass band over the entire frequency spectrum. The different behavior in the case of tapered rods, with the presence of stop and pass bands, is also clearly evident in Figure (2.3).

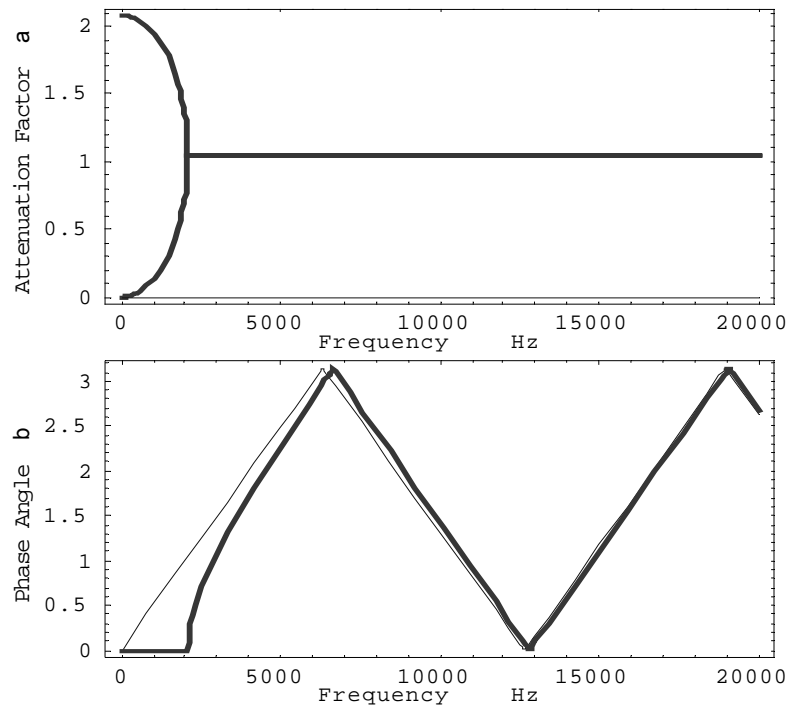


Figure 2.3: Propagation Constants α_i and β_l for uniform rods (thin line) and tapered rods (thick line).

Two different cases are considered and compared to the uniform rod, namely the cases of tapered rods with positive and negative taper parameter a . The three different shapes considered are shown in Figure (2.4):

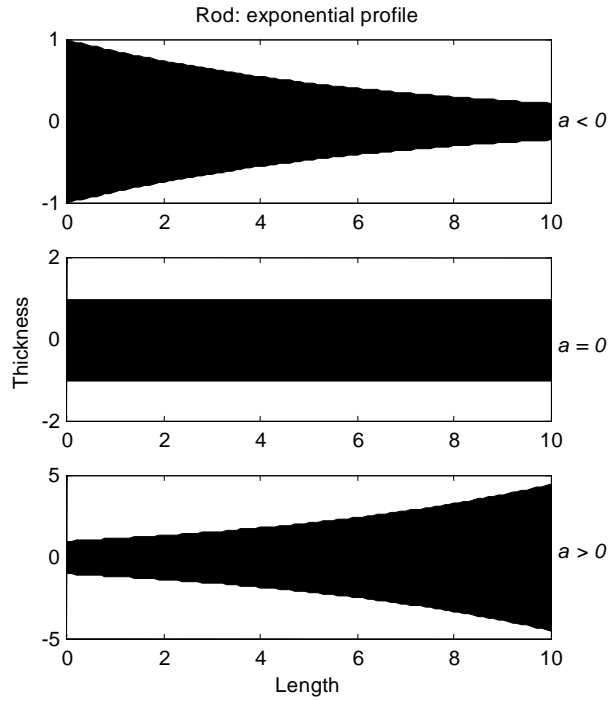


Figure 2.4: Rod aspect for different profiles.

For each of the considered cases, the propagating constants are computed and plotted in Figure (2.5). In the figure, the dotted line corresponds to the uniform rod and there is no attenuation as expected because the decaying amplitude α remains zero all the time. Also, the solid lines correspond to decreasing and increasing cross section. In this case, a stop band is developed making the rod act as a high pass filter.

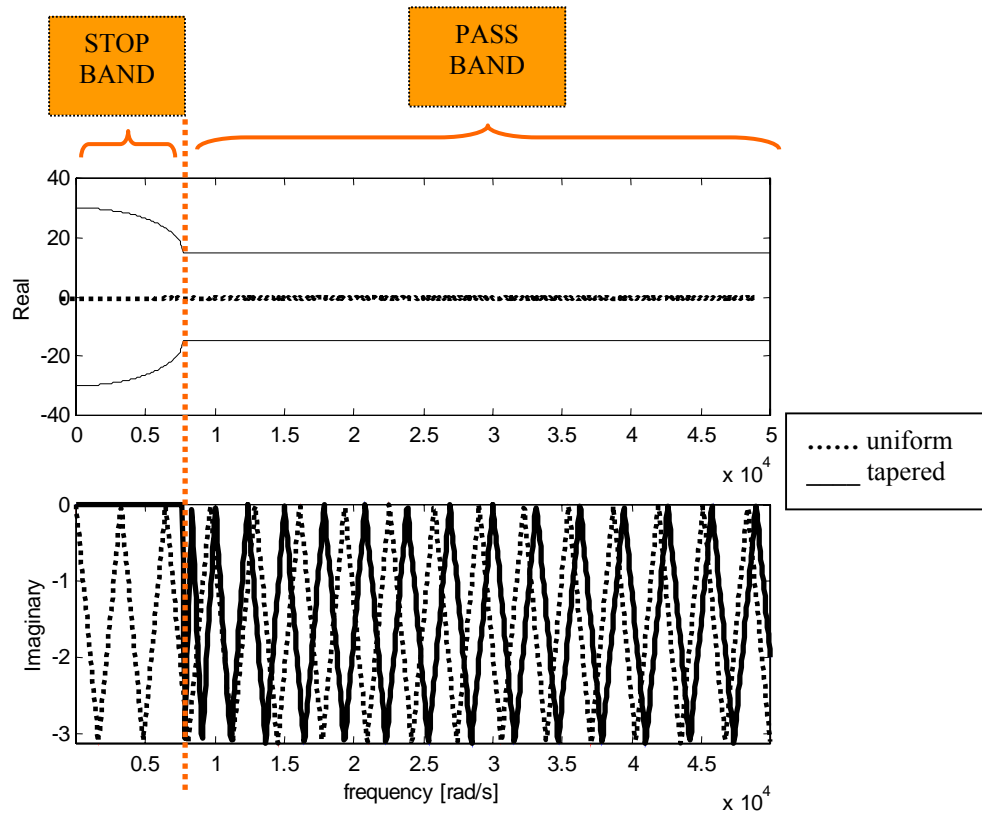


Figure 2.5: Propagation parameter $\mu = \alpha + i\beta$ and cut-off frequency.

It is important here to note that equation (2.6) can be also interpreted as the drive point impedance between the excitation location θ and the measuring point L . It is understood from Figure (2.6) that while the uniform profile feeds the disturbance through as it is, tapered profiles show a stop band at low frequencies so that only signals above the cutoff frequency are transmitted.

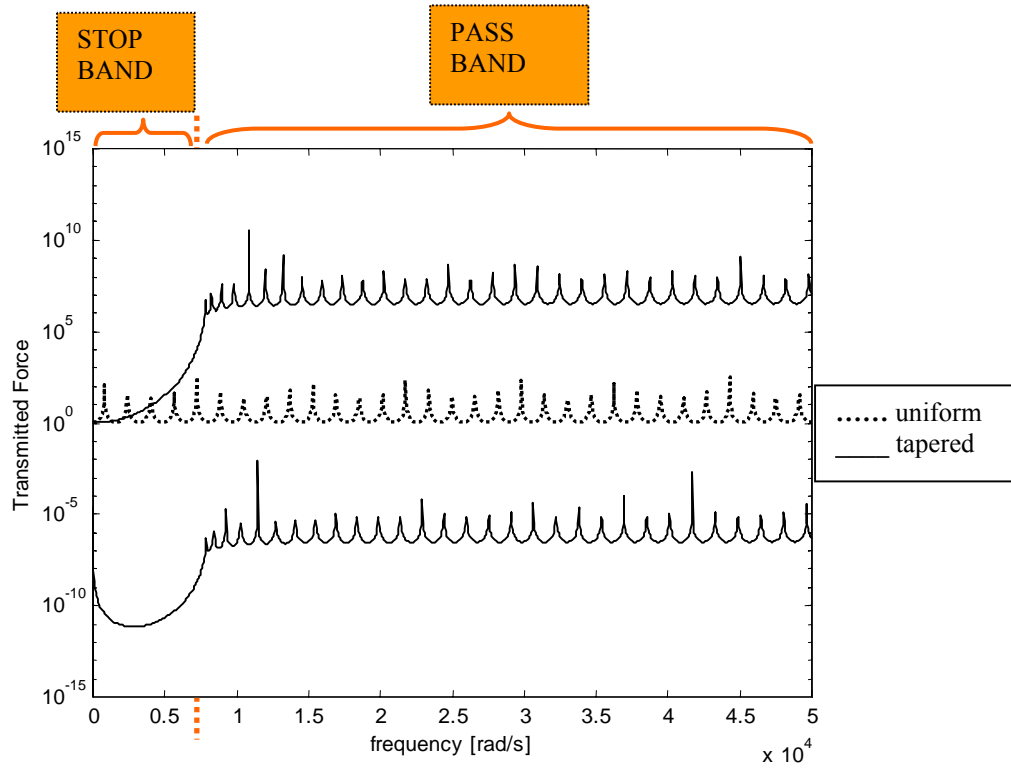


Figure 2.6: Transmitted force: F_1/F_0 .

2.3.2 Polynomial Profile

The cross section is modeled as:

$$A(x) = A_0 \left(1 + a \frac{x}{L}\right)^m \quad (2.13)$$

Polynomial taper is examined because it is more easily implemented for practical purposes, especially in the simplest configuration of linear taper ($m=1$). Note that A_0 and a are predetermined constants.

In this case, the matrix \mathbf{A} becomes:

$$\mathbf{A} = \begin{bmatrix} 0 & 1 \\ -k^2 & -\frac{am}{(L+ax)} \end{bmatrix} \quad (2.14)$$

The wave propagation characteristics for a tapered rod, whose characteristics are listed in Table (2.2), are shown in Figure (2.7) in comparison to the characteristics of the uniform rod.

Table 2.2: PVC Rod Properties.

Parameter	Value
Young Modulus E [Pa]	3.2×10^8
Density ρ [Kg/m³]	1150
Length L [mm]	457.2 (18")
Area A_0 [mm²]	645.16 (2" x 1/2")
Taper parameter a	10

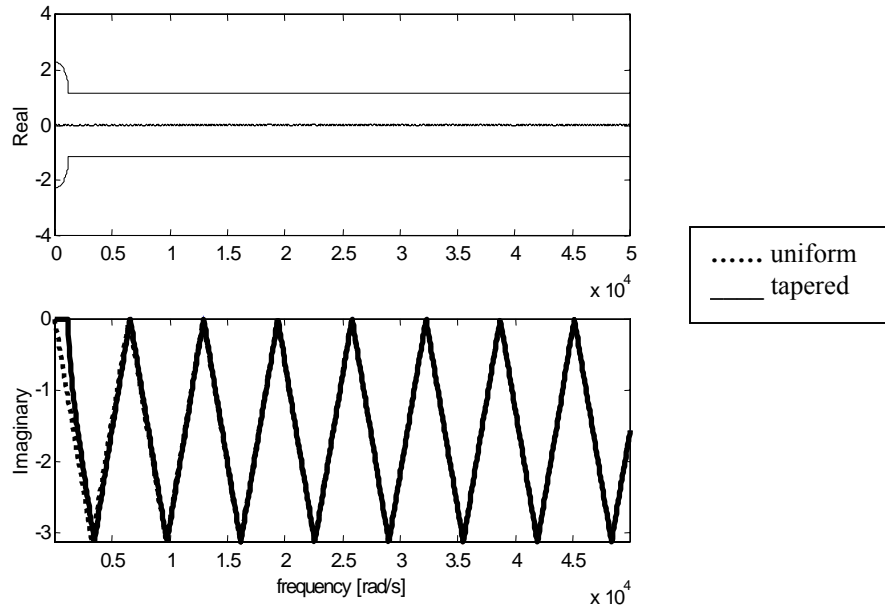


Figure 2.7: Propagation constants $\mu=\alpha+i\beta$ and cut-off frequency.

Note the presence of a cut-off frequency in the propagation characteristics at approximately 1000 Hz. Hence no disturbance lower than 1 kHz will propagate along the structure.

In other words, if the response of a point at location L is considered due to a disturbance exerted at location 0 , Figure (2.8) pictures the shift of the first peak to higher frequencies. This shift to higher frequency is proved to be directly dependent on the taper ratio, as it increases when the taper ratio gets more pronounced.

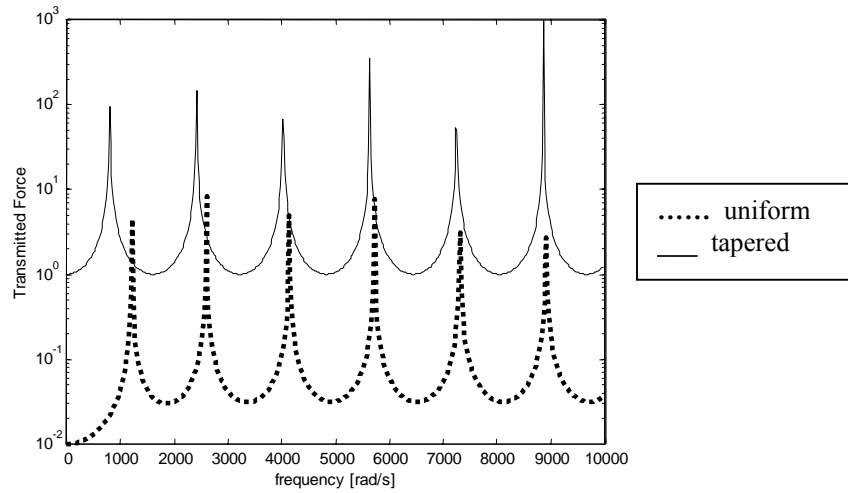


Figure 2.8: Transmitted force: F_1/F_0 .

Let us now write the coefficient a in terms of the more practical geometric aspect ratio of the rod:

1. Exponential profile:

$$a = \ln \frac{A_L}{A_0};$$

$$\omega_c = \frac{a}{2L} \sqrt{\frac{E}{\rho}} = \frac{\ln\left(\frac{A_L}{A_0}\right)}{2L} \sqrt{\frac{E}{\rho}} \quad (2.15)$$

2. Polynomial profile:

$$a = \sqrt[m]{\frac{A_L}{A_0}} - 1; \tag{2.16}$$

$$\omega_c = \frac{m \ln(1+a)}{2L} \sqrt{\frac{E}{\rho}} = \frac{\ln\left(\frac{A_L}{A_0}\right)}{2L} \sqrt{\frac{E}{\rho}}$$

It is interesting to see that in both cases the cut-off frequency exclusively depends on the cross section ratio A_L/A_0 and the length L of the rod, but different types of profile do not play any role.

Hence, because linear profiles ($m=1$) can be easily machined, linearly tapered rods with the material properties shown in Table (2.3) are used in the experimental study described in Section 2.4.

Table 2.3: PVC Prismatic Rod Properties.

Parameter	Value
Young Modulus E [Pa]	3.2×10^8
Density ρ [Kg/m³]	1150
Length L [mm]	457.2 (18")
Height h [mm]	50.8 (2")
Width b [mm]	12.7 (1/2")
Taper Ratio A_L/A_0	4

The transmissibility characteristics of the linearly tapered rod under consideration are displayed in Figures (2.9) and (2.10).

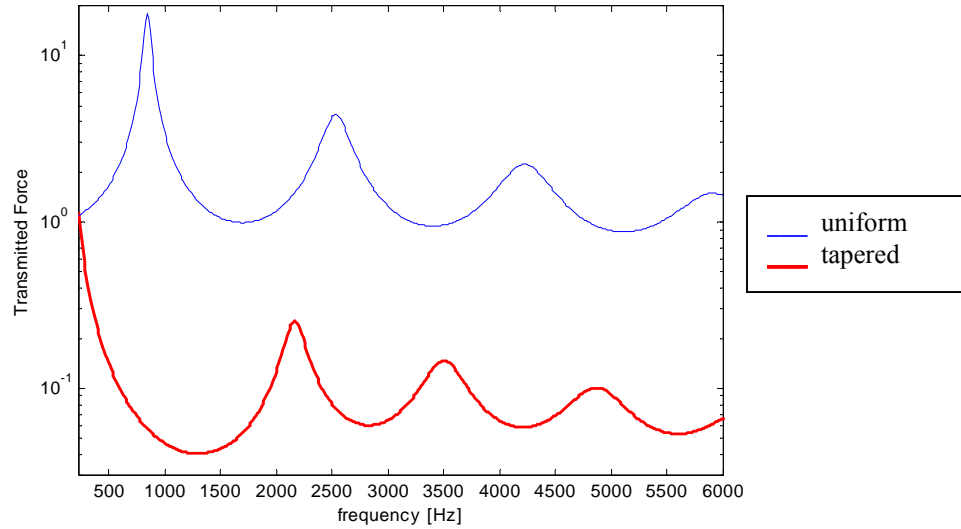
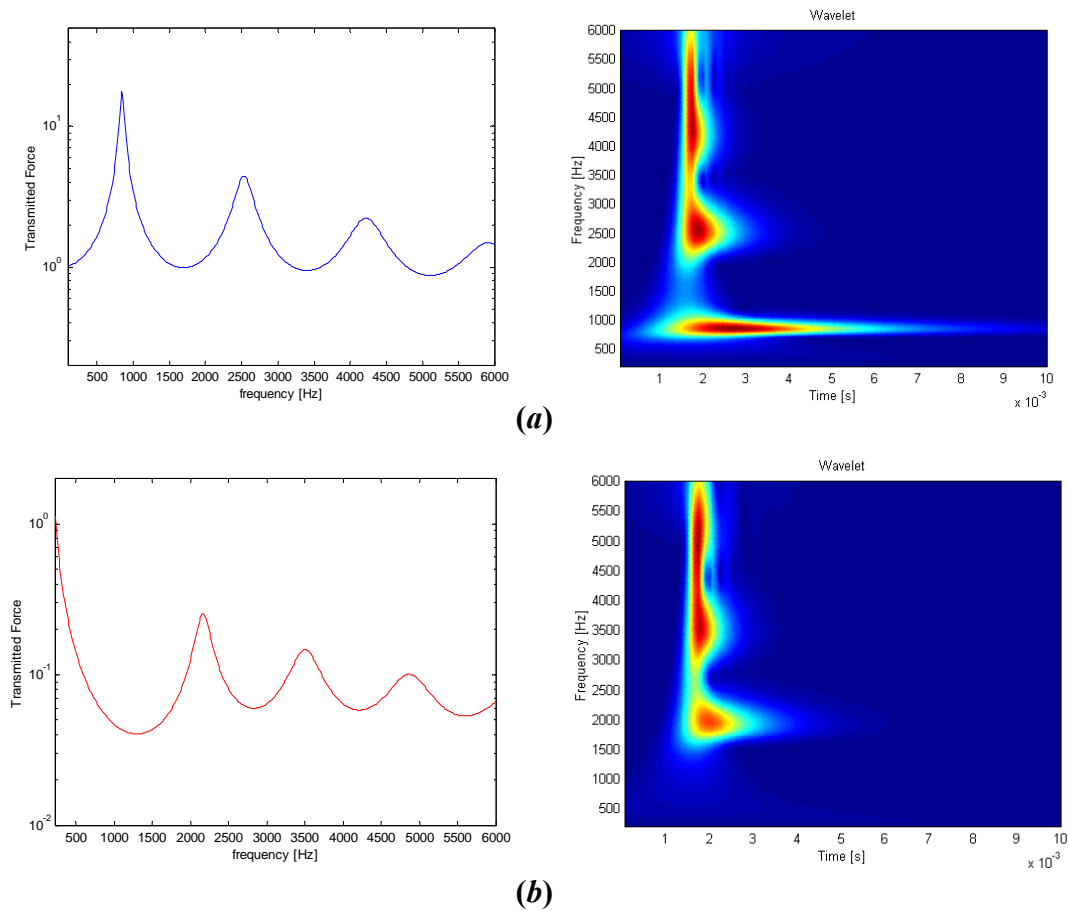


Figure 2.9: Frequency response.

Figure (2.9) presents a comparison between the frequency response of the tapered and uniform rods. The tapered rod exhibits a stop band for frequencies below 1500 Hz.

In order to gain a better understanding of the unique behavior of tapered rods, the Wavelet Transform technique, briefly described in Appendix A.1, is applied to the frequency response of figure (2.9). In figure (2.10), the presence of a stop band extending to 1.5 kHz for the tapered rod is noticeable, while in the case of the uniform rod a pass band over the entire frequency spectrum can be identified.



**Figure 2.10: Frequency response and Wavelet transform of rods:
 (a) uniform thickness and (b) tapered profile.**

2.4 Experimental Characteristics Of Tapered Rods

Experiments are carried out to validate the numerical results obtained in Section 2.3. The setup considered consists in two simple prismatic bars hung in a free-free configuration. The wave propagation characteristics and the transmitted force of the

tapered rod of Figure (2.11) are monitored and compared with the corresponding characteristics of rods with uniform profile. Dimensions and material properties of the rods used in the experiments have been summarized in Table (2.3). One of the two rods had uniform profile while the other was tapered with a geometric ratio $A_L/A_0 = 4$.



Figure (2.11): Tapered rod.

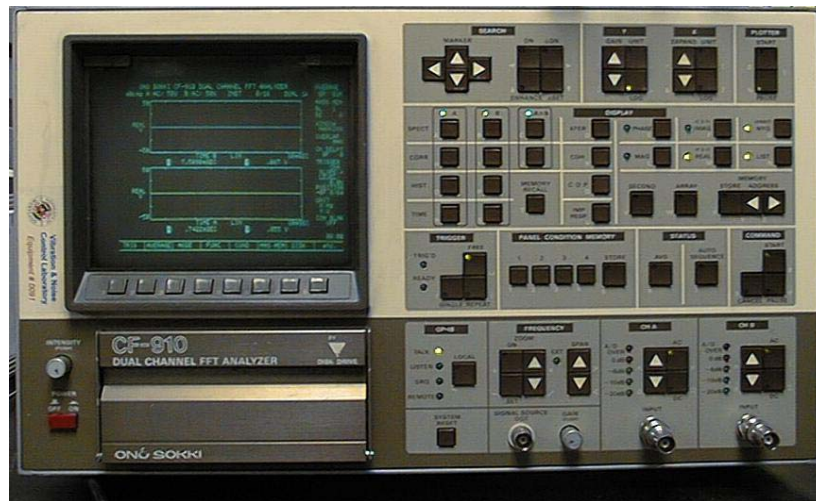


Figure 2.12: Spectrum Analyzer.

An impact hammer (PCB Model 086C02) is used to exert a longitudinal impulsive excitation on one tip of the rod. The longitudinal acceleration at the rod end opposite to the force location is captured by a piezoelectric accelerometer (PCB Model 303A03). The spectrum analyzer (ONO SOKKI Model CF910), in Figure (2.12), is triggered by the input force and records the signal coming from the accelerometer for 10 milliseconds. The stored transient response is analyzed through the Wavelet Transform (WT) in order to capture the pass and stop band characteristics. The WT allows for displaying the energy distribution simultaneously in the time and frequency domain and hence allows for fully describing the filtering characteristics of this class of structures. Results are collected in Figures (2.13) and (2.14).

The captured signal is also truncated at approximately 3 milliseconds in order to isolate the first traveling wave from all further reflections due to the finite length of the rod. This gives a sharper insight in the propagation characteristics of the considered rods.

From Figure (2.13b) it is clear that the impulse is captured without any dispersion occurring as the disturbances travels along the uniform rod. The energy looks equally distributed about the two most significant peaks at approximately 900 Hz and 2000 Hz.

On the other hand, the tapered profile pictured in Figure (2.14b) deforms the impulsive wave as time progresses. This reflects in a shift in frequency of the energy content represented by the WT plot. Note that most of the energy is about the 2000 Hz peak.

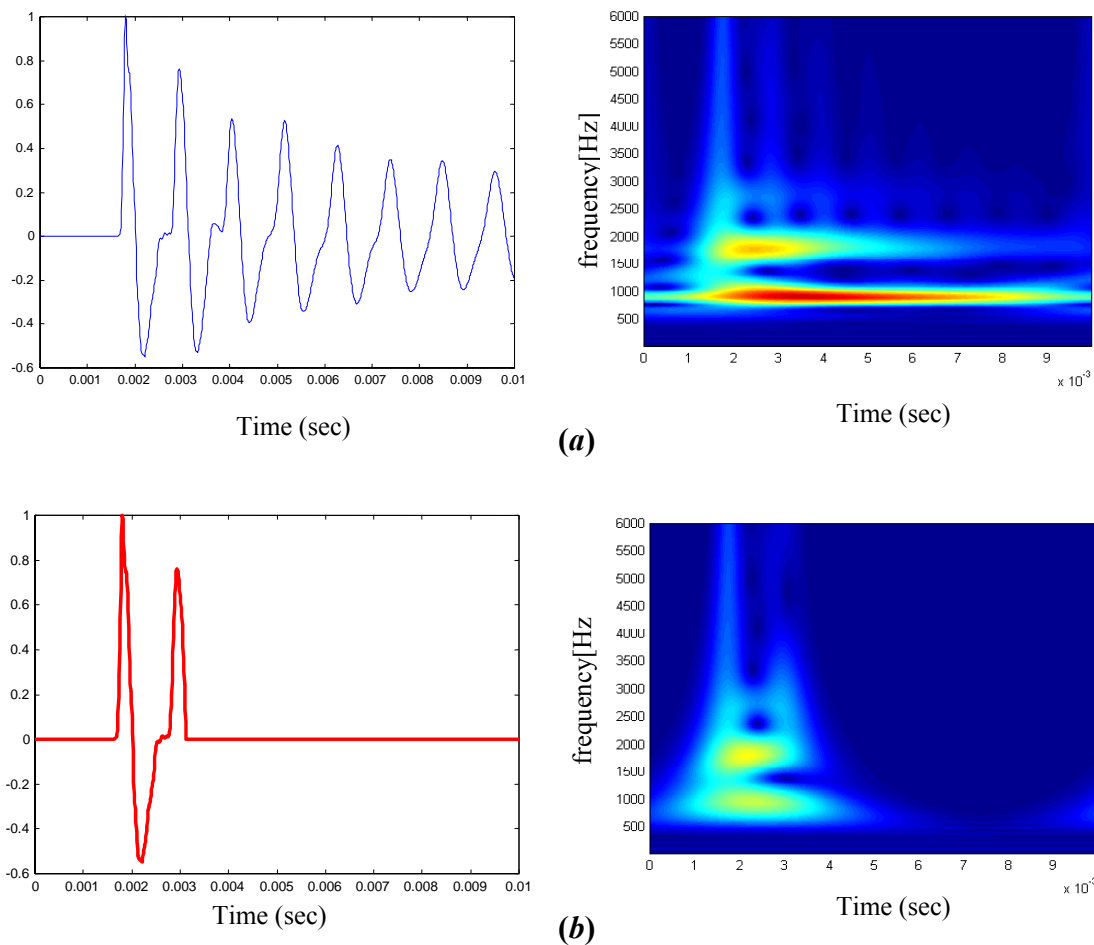


Figure 2.13: Time history and wavelet transform of the response of a uniform rod

(a) full picture and (b) truncated wave.

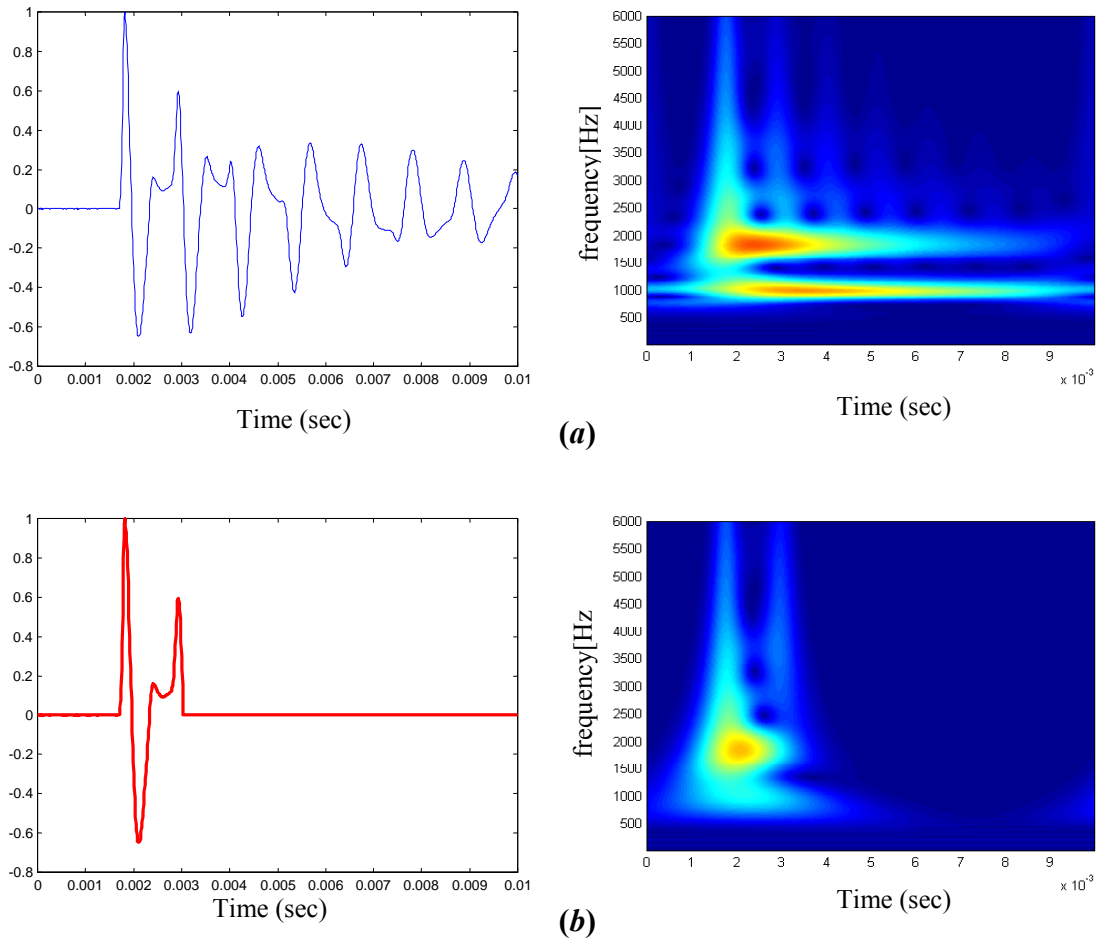


Figure 2.14: Time history and wavelet transform of the response of a tapered rod:

(a) full picture and (b) truncated wave.

2.5 Conclusions

The effect of varying the thickness of one-dimensional wave-guides (rods) can be effectively used to cutoff undesirable low frequency vibrations. The main parameter that influences the spectral location of the cutoff frequency is the ratio between the cross sections at the end of the wave-guide.

The filtering characteristics of these variable geometry rods have also been demonstrated experimentally.

The slight discrepancy between the experimental results and the numerical predictions was caused by the fact that a low pass filter has been used in the experiments in order to filter out the higher frequencies content and better focus on the range of frequencies of interest. In spite of such a discrepancy, it is important to note that rods with tapered profiles are found to shift the energy content to a higher frequency range and, hence, they behave as high-pass mechanical filters.

CHAPTER 3: WAVE PROPAGATION IN PERIODIC SHELLS WITH TAPERED WALL THICKNESS AND CHANGING MATERIAL PROPERTIES

3.1 Introduction

Shells of revolution play an important role in many structural applications. However, the analysis of the dynamics of these structural elements is more complex than the analysis of one-dimensional elements as rods. In fact, traditionally most studies have attempted to adapt the membrane model (very thin shells) for practical calculations. Generally, thick shells present a more interlaced behavior that is not described by extended 2D models. However, the availability of faster computers has shown that analyses of solid bodies based on 3D structural models [17] yield accurate predictions of static displacements, free vibration frequencies and modes, buckling loads, and mode shapes. Many applications require the use of axis-symmetric shells, such as in space vehicles, aircrafts and submarines skins. Transmission shafts for automotive and helicopter industry and turbo-compressor units present even more complex behavior due to the rotation along their axes. All these applications need a careful vibrational and acoustic analysis. Furthermore, the development of particular stop bands through tapered and periodically variable cross sections [43] has become a very interesting field of investigation at this point.

Several researchers have studied three-dimensional vibration of hollow circular cylinders. Early investigations were focused in applying 2D shell theory on circular cylindrical shells having continuously variable wall thickness. In 1973, Stoneking [49] formulated a set of equations to solve vibrations of clamped-clamped tapered cylinders with the partition method. In 1991, Sivadas and Ganesan [47] presented a semi-analytical finite-element analysis for determining the natural frequencies of thin circular isotropic cylindrical shells with linear and quadratic varying section. In their study, Love's first approximation shell theory was considered to solve the problem and investigated different boundary conditions. In 1993, Sivadas and Ganesan [46] improved their model by including the normal strain as well as the transverse shear effects and compared the solutions to two other approximations: the thick shell theory without normal stress and Love's model without shear and rotary inertia. Suzuki *et al.* [50 and 51] presented an analytical solution of the free vibration of a clamped-clamped circular cylindrical shell with quadratic thickness variation along the axial direction.

Basically, only three groups of researchers studied conical shells with variable thickness using 2D-based shell theory. In 1977 Penzes and Padovan [39] characterized a tapered cone with an approximate closed-form solution. Then, Irie *et al.* [18] in 1982 used the transfer matrix approach to treat the case of free vibration of a truncated conical shell having a meridian thickness expressed by an arbitrary function. Natural frequencies and mode-shapes were numerically calculated for linear, parabolic and exponential variable thickness. Takahashi *et al.* [52 and 53] wrote a series of papers (1982-1986) on this subject. 2D models have been developed for moderately thick conical shells of

variable thickness where the normal displacement component is assumed to be constant along the thickness. The tangential displacements and bending rotations is supposed to be linearly varying, as in the well-known Mindlin plate theory. In 1995, Leissa and So [28] presented extensive studies on a 3D-based procedure to determine free vibration frequencies and modes for truncated hollow cones with arbitrary thickness by applying Ritz method. These results were refined in 1999 by Kang and Leissa [20].

The present chapter is organized as follows: a literature survey has been presented in Section 3.1. In Section 3.2, the equations of motion are derived from the energy conservation principles using the transfer matrix approach. This approach allows further investigations of the effect of varying the geometry and/or stiffness, which are the main goals of Sections 3.3. Section 3.3.1 presents numerical solution of examples of exponential and polynomial tapered shell. The propagation constants for the longitudinal and transverse waves are discussed and the time-frequency plots are generated by the Wavelet transform for a linear profile. Section 3.3.2 investigates the possibility of using Functionally Graded Materials (FGM) where by the material Young's modulus is allowed to vary according to exponential or polynomial shapes. Numerical solution of various examples is presented in terms of propagation constants in order to quantify the effect of geometry changes. Moreover, the combined effect of varying the geometrical profiles as well as the gradient of the elastic properties is also investigated.

Section 3.4 describes the experiments conducted on a linearly tapered shell. The time response and the corresponding Wavelet transform analysis are compared to the numerical predictions of Section 3.3. Section 3.5 extends the results of Section 3.3.1 to

the case of periodic shell elements. All different combinations of periodicity are surveyed. Section 3.6 summarizes the conclusions indicating that the best results are obtained when combining tapered geometry and either functionally graded materials or with periodicity. Bi-periodic tapered elements have exhibited the most interesting behavior.

3.2 Equation Of Motion For Shells Of Variable Material Properties And Geometry

Under hypothesis of small deformation, the elastic strains (ε , γ) for the generic three-dimensional shell shown Figure (3.1) are given by [13]:

$$\begin{aligned}
 \varepsilon_{(x)} &= \frac{\partial U(x, \vartheta, r, t)}{\partial x} \quad , \\
 \varepsilon_{(\vartheta)} &= \frac{1}{R+r} \left[\frac{\partial V(x, \vartheta, r, t)}{\partial \vartheta} + W(x, \vartheta, r, t) \right] \quad , \\
 \varepsilon_{(r)} &= \frac{\partial W(x, \vartheta, r, t)}{\partial r} \quad , \\
 \gamma_{(x\vartheta)} &= \frac{1}{R+r} \frac{\partial U(x, \vartheta, r, t)}{\partial \vartheta} + \frac{\partial V(x, \vartheta, r, t)}{\partial x} \quad , \\
 \gamma_{(xr)} &= \frac{\partial U(x, \vartheta, r, t)}{\partial r} + \frac{\partial W(x, \vartheta, r, t)}{\partial x} \quad , \\
 \text{and} \quad \gamma_{(x\vartheta)} &= \frac{\partial V(x, \vartheta, r, t)}{\partial r} + \frac{1}{R+r} \left[\frac{\partial W(x, \vartheta, r, t)}{\partial \vartheta} - V(x, \vartheta, r, t) \right] \quad ,
 \end{aligned} \tag{3.1}$$

where: U , V , W are the displacement in the three spatial directions (x , ϑ , r) and R is the medium radius.

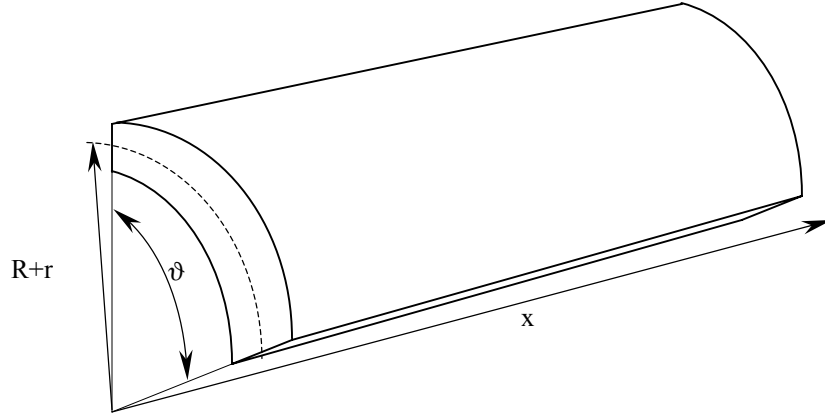


Figure 3.1: Three-dimensional cylindrical shell.

Introducing Kirchhoff hypotheses, such that U and V linearly vary through the thickness and W is constant through the thickness, then:

$$\begin{aligned}
 U(x, \vartheta, r, t) &= u(x, \vartheta, t) - r \frac{\partial w(x, \vartheta, t)}{\partial x} \quad , \\
 V(x, \vartheta, r, t) &= v(x, \vartheta, t) + \frac{r}{R} \left[v(x, \vartheta, t) - \frac{\partial w(x, \vartheta, t)}{\partial \vartheta} \right] \quad ,
 \end{aligned} \tag{3.2}$$

and $W(x, \vartheta, r, t) = w(x, \vartheta, t)$.

Substituting equation (3.2) into (3.1), a simpler expression is obtained:

$$\begin{aligned}
\mathcal{E}_{(x)} &= u_{,x} - r w_{,xx} \quad , \\
\mathcal{E}_{(\vartheta)} &= \frac{1}{R \left(1 + \frac{r}{R}\right)} w - \frac{1}{R} v_{,\vartheta} - \frac{\frac{r}{R}}{R \left(1 + \frac{r}{R}\right)} w_{,\vartheta\vartheta} \quad , \\
\mathcal{E}_{(r)} &= 0 \quad , \\
\mathcal{Y}_{(x\vartheta)} &= \frac{1}{R \left(1 + \frac{r}{R}\right)} u_{,\vartheta} - \left(1 + \frac{r}{R}\right) v_{,x} - \frac{r}{R} \left[1 + \frac{1}{R \left(1 + \frac{r}{R}\right)}\right] w_{,x\vartheta} \quad , \\
\mathcal{Y}_{(xr)} &= -w_{,x} + w_{,x} = 0 \quad , \\
\text{and } \mathcal{Y}_{(x\vartheta)} &= \frac{1}{R} (v - w_{,\vartheta}) + \frac{1}{R} (w_{,\vartheta} - v) = 0 \quad .
\end{aligned} \tag{3.3}$$

If we assume the axial symmetric shell to be thin ($r/R \ll 1$), and torsion and bending to be uncoupled (Donnell-Mushtari) ($v_{,x} \cong 0$; $v_{,\vartheta} \cong 0$), then equations (3.3) reduce to [29]:

$$\begin{aligned}
\mathcal{E}_{(x)} &= u_{,x} - r w_{,xx} \quad , \\
\mathcal{E}_{(\vartheta)} &\cong \frac{1}{R} w \quad , \\
\mathcal{E}_{(r)} &= 0 \quad , \\
\mathcal{Y}_{(x\vartheta)} &\cong 0 \quad , \\
\text{and } \mathcal{Y}_{(xr), \mathcal{Y}_{(x\vartheta)}} &= 0 \quad .
\end{aligned} \tag{3.4}$$

In order to obtain the equations of motion for the axis-symmetric shell, the energy method approach is employed along with the Hamilton's principle, such that:

$$\int_{t_1}^{t_2} \delta(\mathbb{T} - \mathbb{U} + \mathbb{W}) dt = 0 \quad (3.5)$$

where \mathbb{T} is the Kinetic Energy of the structure, \mathbb{U} denotes its Potential Energy and \mathbb{W} defines the Virtual Work done by any external force.

The general expressions of these quantities for a three-dimensional structure are:

$$\begin{aligned} \mathbb{U} &= \frac{1}{2} \iiint_{Vol} \left[\sigma_{(x)} \varepsilon_{(x)} + \sigma_{(\vartheta)} \varepsilon_{(\vartheta)} + \sigma_{(r)} \varepsilon_{(r)} + \tau_{(x\vartheta)} \gamma_{(x\vartheta)} + \tau_{(r\vartheta)} \gamma_{(r\vartheta)} + \tau_{(xr)} \gamma_{(xr)} \right] dV \quad , \\ \mathbb{T} &= \frac{1}{2} \iiint_{Vol} \rho \left[\dot{u}^2 + \dot{v}^2 + \dot{w}^2 \right] dV \quad , \end{aligned} \quad (3.6)$$

and $\delta \mathbb{W} \cong 0$.

The constitutive relations for a linear elastic solid are

$$\begin{aligned} \sigma_{(x)} &= \frac{E}{1-\nu^2} \left(\varepsilon_{(x)} + \nu \varepsilon_{(\vartheta)} \right) \quad , \\ \sigma_{(\vartheta)} &= \frac{E}{1-\nu^2} \left(\varepsilon_{(\vartheta)} + \nu \varepsilon_{(x)} \right) \quad , \end{aligned} \quad (3.7)$$

and $\sigma_{(r)} \cong 0$.

Hence, the kinetic and potential energies reduce to:

$$\mathbf{U} = \frac{1}{2} \int_0^L 2\pi \int_{-h(x)/2}^{h(x)/2} \frac{E}{1-\nu^2} \left[\varepsilon_{(x)}^2 + 2\nu \varepsilon_{(x)} \varepsilon_{(\vartheta)} + \varepsilon_{(\vartheta)}^2 \right] R(x) dr dx \quad , \quad (3.8)$$

$$\mathbf{T} = \frac{1}{2} \rho \int_0^L 2\pi R(x) h(x) \left[\dot{u}^2 + \dot{w}^2 \right] dx \quad ,$$

or

$$\mathbf{U} = \frac{1}{2} \int_0^L 2\pi \left[g \left(u_{,x}^2 + 2\nu \frac{u_{,x} w}{R(x)} + \frac{w^2}{R(x)^2} \right) + q w_{,xx}^2 \right] dx \quad , \quad (3.9)$$

$$\mathbf{T} = \frac{1}{2} \int_0^L 2\pi \frac{g}{c^2} \left[\dot{u}^2 + \dot{w}^2 \right] dx \quad ,$$

where:

$$g = R(x) K_l(x) = R(x) \frac{Eh(x)}{(1-\nu^2)} \text{ is the longitudinal rigidity of the shell,}$$

$$q = R(x) D_l(x) = R(x) \frac{Eh(x)^3}{12(1-\nu^2)} \text{ is the bending rigidity of the shell,}$$

and $c = \sqrt{\frac{E/\rho}{(1-\nu^2)}}$ is the characteristic wave propagation phase speed.

Applying Hamilton's principle yields the following equations of motion for the tapered shell:

$$\frac{g}{c^2} \ddot{u} = g u_{,xx} + g_{,x} u_{,x} + \nu \left(\frac{g}{R} \right)_{,x} w + \nu \frac{g}{R} w_{,x} \quad , \quad (3.10)$$

and $\frac{g}{c^2} \ddot{w} + q w_{,xxxx} + 2q_{,x} w_{,xxx} + q_{,xx} w_{,xx} + \frac{g}{R^2} w + \nu \frac{g}{R} u_{,x} = 0 \quad .$

Applying the Separation Principle to the displacements u and w gives:

$$u(x, t) = u(x)e^{j\omega t} \quad \text{and} \quad w(x, t) = w(x)e^{j\omega t} \quad (3.11)$$

From equations (3.10) and (3.11), the dynamics of the shell subjected to harmonic excitation are given by:

$$u_{,xx} = -\frac{\omega^2}{c^2}u - \frac{g_{,x}}{g}u_{,x} - \nu \frac{\left(\frac{g}{R}\right)_{,x}}{g}w - \nu \frac{1}{R}w_{,x} \quad , \quad (3.12)$$

and

$$w_{,xxx} = \frac{g}{q} \left(\frac{\omega^2}{c^2} - \frac{1}{R^2} \right) w - \frac{q_{,xx}}{q}w_{,xx} - 2\frac{q_{,x}}{q}w_{,xxx} - \nu \frac{g}{qR}u_{,x} \quad .$$

It is convenient, for the further analysis, to have a state-space representation of the shell system as follows:

$$\frac{\partial}{\partial x}U(x) = \mathbf{A}(x)U(x) \quad (3.13)$$

$$\text{where } \mathbf{A}(x) = \begin{bmatrix} 0 & 0 & 0 & 1 & 0 & 0 \\ 0 & 0 & 1 & 0 & 0 & 0 \\ 0 & 0 & 0 & 0 & 0 & 1 \\ -\frac{\omega^2}{c^2} & -v \frac{\left(\frac{g}{R}\right)_{,x}}{g} & -v \frac{1}{R} & -\frac{g_{,x}}{g} & 0 & 0 \\ 0 & \frac{g}{q} \left(\frac{\omega^2}{c^2} - \frac{1}{R^2} \right) & 0 & -v \frac{g}{qR} & -2 \frac{q_{,x}}{q} & -\frac{q_{,xx}}{q} \\ 0 & 0 & 0 & 0 & 1 & 0 \end{bmatrix}$$

represents the *state-space matrix*

$$\text{and } U(x) = \begin{Bmatrix} u \\ w \\ w_{,x} \\ u_{,x} \\ w_{,xxx} \\ w_{,xx} \end{Bmatrix} \text{ is the } \textit{state-space vector}.$$

Solutions to equation (3.13) are calculated by the integration over the shell length L to give:

$$U(L) = e^{\int_0^L [\mathbf{A}(x)] dx} U(0) \quad (3.14)$$

The last three components of the state vector $U(x)$ can be transformed into *generalized forces* (traction N , shear Q , bending moment M) through the coordinate *transformation matrix* $[\mathbf{G}_x]$ and a new state vector Y is obtained:

$$Y(x) = \mathbf{G}_x U(x) \quad (3.15)$$

where

$$Y(x) = \begin{Bmatrix} u \\ w \\ w_x \\ N \\ Q \\ M \end{Bmatrix} \triangleq \text{transfer vector at } x$$

$$\text{and } \mathbf{G}_x = \begin{bmatrix} 1 & 0 & 0 & 0 & 0 & 0 \\ 0 & 1 & 0 & 0 & 0 & 0 \\ 0 & 0 & 1 & 0 & 0 & 0 \\ 0 & \frac{v}{R(x)} K_t(x) & 0 & K_t(x) & 0 & 0 \\ 0 & 0 & 0 & 0 & -D_t(x) & 0 \\ 0 & 0 & 0 & 0 & 0 & D_t(x) \end{bmatrix} \triangleq \text{transformation matrix}$$

The vector Y in equation (3.15) transforms (3.14) into the *Transfer Matrix* representation as follows:

$$Y_L = \left[\mathbf{G}_L e^{\int_0^L \mathbf{A}(x) dx} \mathbf{G}_0^{-1} \right] Y_0 = \mathbf{T} Y_0 \quad (3.16)$$

where $(x = 0) \Rightarrow Y_0 = [\mathbf{G}_0] U(0)$ and $(x = L) \Rightarrow Y_L = [\mathbf{G}_L] U(L)$.

The eigenvalues λ_i of the transfer matrix \mathbf{T} give all the information about the propagation characteristics.

From the previous chapter, it can be summarized that:

$$(Y_L)_i = \lambda_i (Y_O)_i = e^{\alpha_i} (Y_O)_i e^{i\beta_i} \quad (3.17)$$

where $\lambda_i = e^{\mu_i} = e^{\alpha_i} e^{i\beta_i}$.

Equation (3.17) shows that the disturbance measured at location L is shifted in phase by the factor β (*phase angle*) with respect to the signal measured at location O and it is magnified or attenuated by factor α (*attenuation factor*) depending on the taper ratio. When the phase β shifts to 180° , destructive interference occurs between the traveling wave and the reflected wave so that no remaining disturbance propagates along the shell.

3.3 Numerical Examples

A plastic composite shell is considered in this chapter. The basic properties of this shell are listed in Table (3.1). As indicated in Chapter 1, changes in the material properties and/or geometry can affect considerably the propagation characteristics of the structure.

Table 3.1: PVC Shell Properties.

Parameter	Value
Young Modulus [Pa]	3.6×10^9
Density [Kg/m³]	1700
Length [mm]	315 (12 3/8")
External Diameter [mm]	48 (1.9")
Internal Diameter [mm]	40 (1.58")
Geometric Taper Ratio	4
FGM Ratio	10

3.3.1 Geometrically Tapered Profiles

It is of great interest to study the influence of thickness variation along the length of a straight cylindrical shell. In the present study, only the internal diameter will assume different profiles, while the outer diameter is maintained constant.

Hence, the medium radius $R(x)$ at any cross-section x is represented as function of the fixed outer diameter D_0 and the variable thickness $h(x)$ as follows:

$$R(x) = \frac{D_0 - h(x)}{2} \quad (3.19)$$

In order to compare results with the characteristics of a typical uniform shell, the mass is also kept constant, which adds a constraint on the initial thickness h_0 , such that

$$\int_{Vol} R(x)h(x)dV = \pi(D_0 - h_u)h_u L \quad (3.20)$$

Two different profiles are presented in comparison with the uniform shell, namely the exponential profile and the polynomial profile.

3.3.1.1 Exponential Profile

The thickness $h(x)$ is modeled as follows, according to Figure (3.2):

$$h(x) = h_0 e^{\frac{x}{L}} \quad (3.21)$$

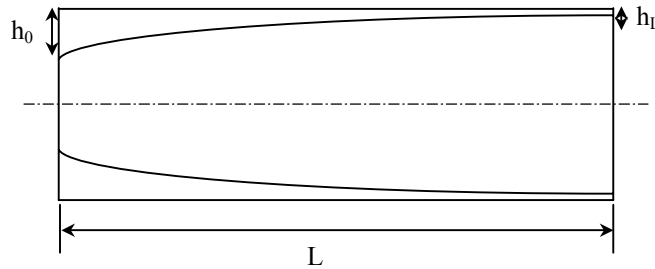


Figure 3.2: Section of exponential-tapered shell.

Parameter a is quickly identified when the *thickness ratio* is decided:

$$a = \ln \frac{h_L}{h_0} \quad (3.22)$$

The eigenvalues problem defined by equations (3.16) and (3.17) is numerically solved with Matlab.

The expression for the state-space matrix \mathbf{A} and the transformation matrix \mathbf{G}_x reduce to:

$$[\mathbf{A}(x)] = \begin{bmatrix} 0 & 0 & 0 & 1 & 0 & 0 \\ 0 & 0 & 1 & 0 & 0 & 0 \\ 0 & 0 & 0 & 0 & 0 & 1 \\ -\frac{\omega^2}{c^2} & -\left(\frac{a}{L}\right)\left(\frac{\nu}{R(x)}\right) & -\frac{\nu}{R(x)} & -\left(\frac{a}{L}\right)\left(1 - \frac{h(x)}{2R(x)}\right) & 0 & 0 \\ 0 & \left(\frac{12}{h^2(x)}\right)\left(\frac{\omega^2}{c^2} - \frac{1}{R^2(x)}\right) & 0 & -\nu\left(\frac{12}{R(x)h^2(x)}\right) & -2\left(\frac{a}{L}\right)\left(3 - \frac{h(x)}{2R(x)}\right) & -\left(\frac{a}{L}\right)^2\left(9 - 7\frac{h(x)}{2R(x)}\right) \\ 0 & 0 & 0 & 0 & 1 & 0 \end{bmatrix} \quad (3.23)$$

$$\text{and } [\mathbf{G}_x] = \begin{bmatrix} 1 & 0 & 0 & 0 & 0 & 0 \\ 0 & 1 & 0 & 0 & 0 & 0 \\ 0 & 0 & 1 & 0 & 0 & 0 \\ 0 & \frac{\nu Eh(x)}{(1-\nu^2)R(x)} & 0 & \frac{Eh(x)}{(1-\nu^2)} & 0 & 0 \\ 0 & 0 & 0 & 0 & -\frac{Eh(x)^3 R(x)}{12(1-\nu^2)} & 0 \\ 0 & 0 & 0 & 0 & 0 & \frac{Eh(x)^3 R(x)}{12(1-\nu^2)} \end{bmatrix} \quad (3.24)$$

The propagation constants are plotted in the frequency domain as shown in Figure (3.3). One can recognize the longitudinal and the bending characteristics and compare them to the corresponding characteristics of a uniformly shaped cylinder:

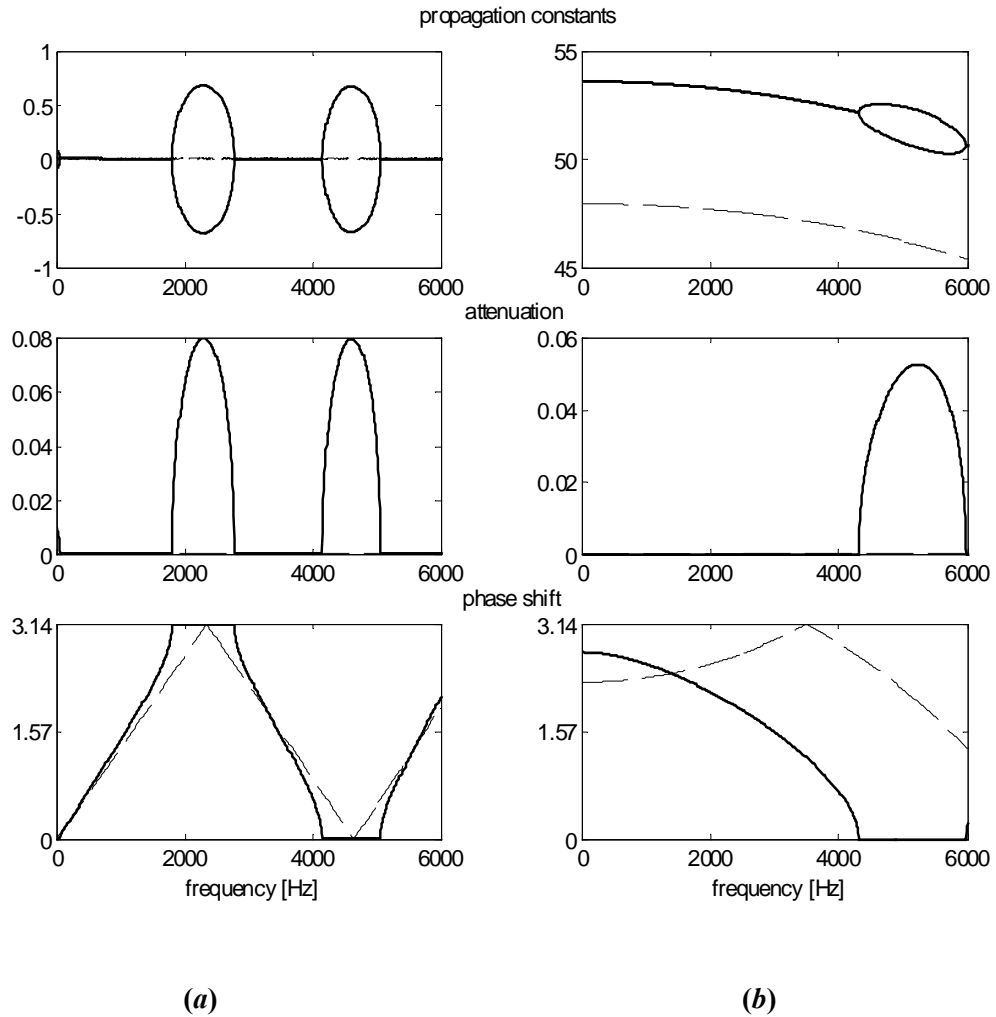


**Figure 3.3: Propagation constants of uniform (dash) and tapered (solid) shells:
(a) longitudinal direction and (b) radial direction.**

3.3.1.2 Polynomial Profile

The thickness $h(x)$ according to Figure (3.4), is given by:

$$h(x) = h_0 \left(1 + a \frac{x}{L} \right)^m \quad (3.25)$$

where the parameter a is function of the thickness ratio:

$$a = \sqrt[m]{\frac{h_L}{h_0}} - 1 \quad (3.26)$$

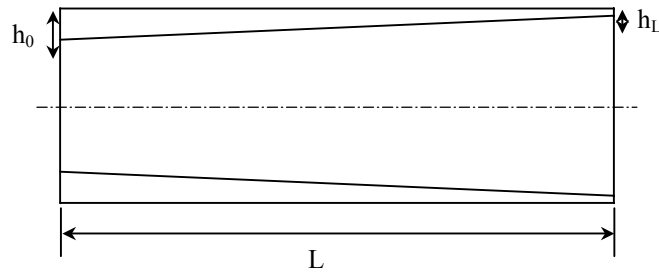


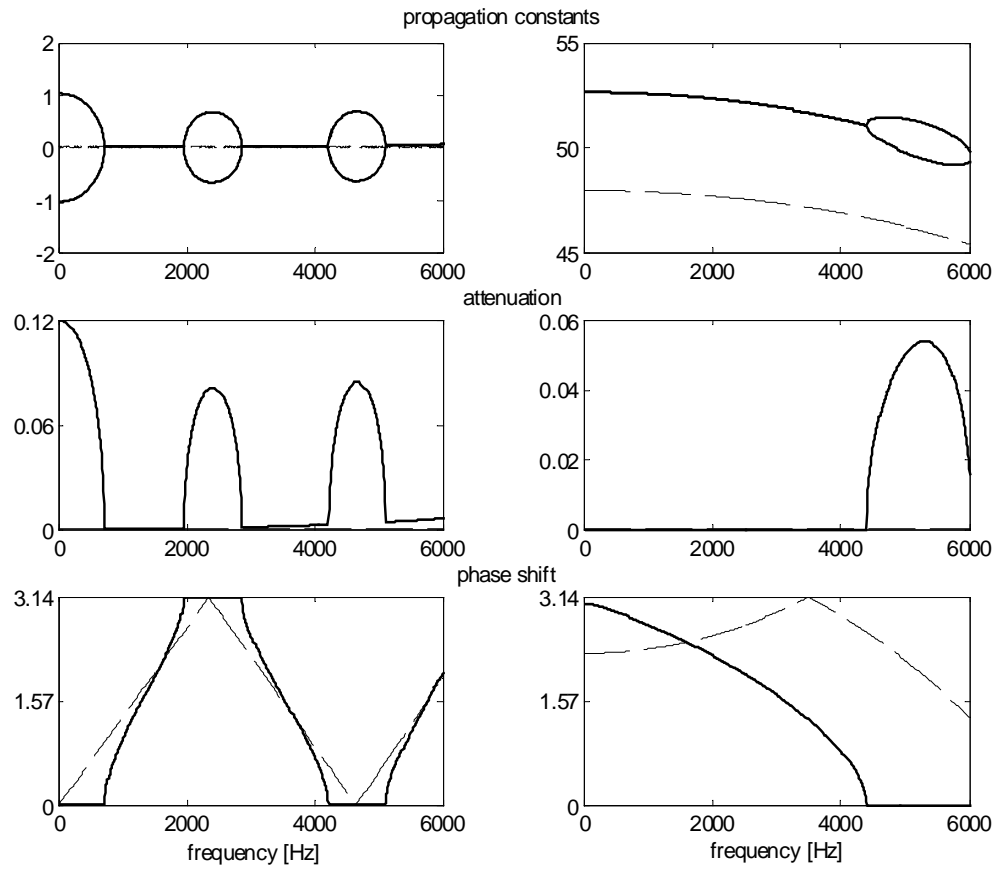
Figure 3.4: Cross-section of a linearly tapered shell.

Hence, the state-space matrix \mathbf{A} and the transformation matrix \mathbf{G}_x become:

$$[\mathbf{A}(x)] = \begin{bmatrix} 0 & 0 & 0 & 1 & 0 & 0 \\ 0 & 0 & 1 & 0 & 0 & 0 \\ 0 & 0 & 0 & 0 & 0 & 1 \\ -\frac{\omega^2}{c^2} & -\nu \left(\frac{a}{L} \right) \left(\frac{1}{h(x)(D_0-h(x))} \right) & -\nu \left(\frac{2}{D_0-h(x)} \right) & -\left(\frac{a}{L} \right) \left(\frac{D_0-2h(x)}{h(x)(D_0-h(x))} \right) & 0 & 0 \\ 0 & \left(\frac{12}{h^2(x)} \right) \left(\frac{\omega^2}{c^2} - \frac{4}{(D_0-h(x))^2} \right) & 0 & -\nu \left(\frac{12}{h^2(x)} \right) \left(\frac{2}{(D_0-h(x))} \right) & -2 \left(\frac{a}{L} \right) \left(\frac{3D_0-4h(x)}{h(x)(D_0-h(x))} \right) & -6 \left(\frac{a}{L} \right)^2 \left(\frac{D_0-2h(x)}{h(x)^2(D_0-h(x))} \right) \\ 0 & 0 & 0 & 0 & 1 & 0 \end{bmatrix} \quad (3.27)$$

$$\text{and } [\mathbf{G}_x] = \begin{bmatrix} 1 & 0 & 0 & 0 & 0 & 0 \\ 0 & 1 & 0 & 0 & 0 & 0 \\ 0 & 0 & 1 & 0 & 0 & 0 \\ 0 & \frac{2\nu Eh(x)}{(1-\nu^2)(D_0-h(x))} & 0 & \frac{Eh(x)}{(1-\nu^2)} & 0 & 0 \\ 0 & 0 & 0 & 0 & -\frac{Eh(x)^3(D_0-h(x))}{24(1-\nu^2)} & 0 \\ 0 & 0 & 0 & 0 & 0 & \frac{Eh(x)^3(D_0-h(x))}{24(1-\nu^2)} \end{bmatrix} \quad (3.28)$$

Emphasis is placed here on linearly tapered shells ($m=1$) because of the ease of their machining. Figure (3.5) portrays the propagation constants in the frequency domain. Such characteristics can be compared to that of shells with exponential taper (Figure 3.3). The interesting point is that there is not a big difference in the performance between the two profiles. Indeed, for the actual choice of dimensions and material, the longitudinal attenuation is more effective at low frequencies than for the case of exponential profile. The radial propagation characteristics are comparable in the two cases.



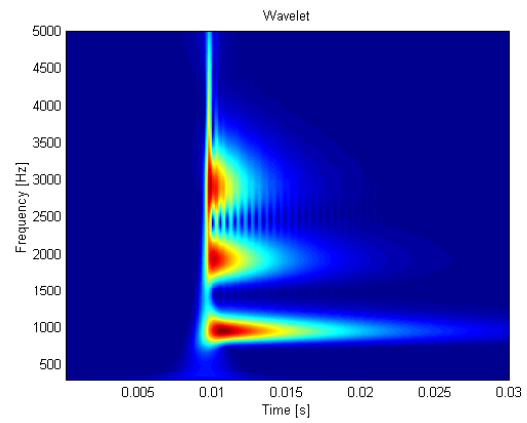
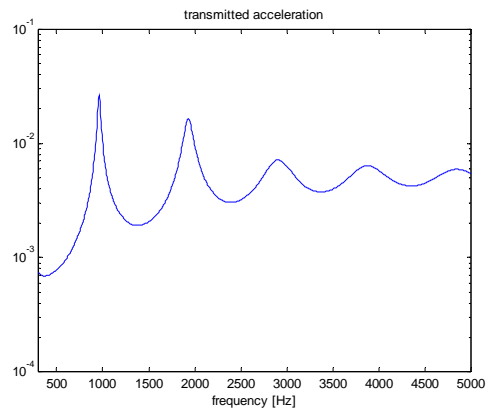
(a)

(b)

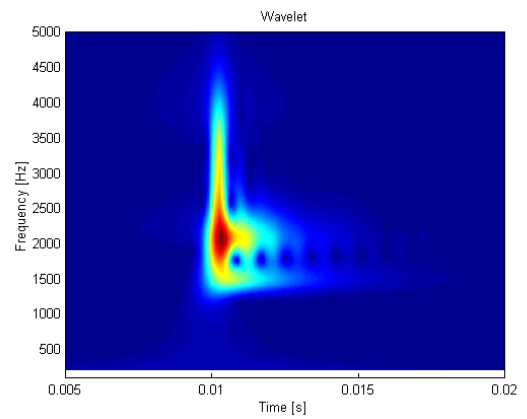
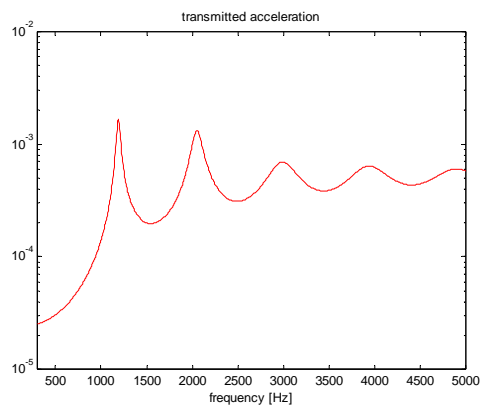
Figure 3.5: Propagation constants of uniform (dash) and tapered (solid) shells:

(a) longitudinal direction and (b) radial direction.

In order to gain a better understanding of the energy distribution of the shell in the time and frequency domains, the Wavelet transform technique is applied when the shell is subjected to an impulsive load exerted at location θ . Figure (3.6) emphasizes that the transmitted energy shifts to higher modes and the peak below 1 kHz vanishes.



(a)



(b)

Figure 3.6: Frequency response and Wavelet Transform:

(a) uniform thickness and (b) tapered profile.

3.3.2 Functionally Graded Materials

The focus is now placed on tuning Young's modulus of the material in order to improve the vibration properties.

First, comparisons are made with plain shell, and then the benefit of combining the effect of geometrical changes with FGM will be considered. Young's Modulus is modeled as either a polynomial function or an exponential function, following the same line of thought as presented in the previous chapter.

3.3.2.1 FGM Effect: Exponential Grading

The *exponential* model of Young's modulus is assumed to be

$$E(x) = E_0 e^{\frac{x}{L}} \quad (3.29)$$

where the coefficient e is more conveniently calculated from the modulus ratio between the two ends of the shell:

$$e = \ln \frac{E_L}{E_0} \quad (3.30)$$

Recalling the general solution for the equations of motion obtained in Section 3.2, equations (3.12) to (3.17), the following expression for the state-space matrix \mathbf{A} are obtained:

$$[\mathbf{A}(x)] = \begin{bmatrix} 0 & 0 & 0 & 1 & 0 & 0 \\ 0 & 0 & 1 & 0 & 0 & 0 \\ 0 & 0 & 0 & 0 & 0 & 1 \\ -\frac{\omega^2}{c^2} & -\left(\frac{e}{L}\right)\frac{\nu}{R} & -\frac{\nu}{R} & -\left(\frac{e}{L}\right) & 0 & 0 \\ 0 & \left(\frac{12}{h^2}\right)\left(\frac{\omega^2}{c^2} - \frac{1}{R^2}\right) & 0 & -\frac{12\nu}{Rh^2} & -2\left(\frac{e}{L}\right) & -\left(\frac{e}{L}\right)^2 \\ 0 & 0 & 0 & 0 & 1 & 0 \end{bmatrix} \quad (3.31)$$

Also, the transformation matrix \mathbf{G}_x has the following form:

$$[\mathbf{G}_x] = \begin{bmatrix} 1 & 0 & 0 & 0 & 0 & 0 \\ 0 & 1 & 0 & 0 & 0 & 0 \\ 0 & 0 & 1 & 0 & 0 & 0 \\ 0 & \frac{\nu E(x)}{(1-\nu^2)R}h & 0 & \frac{E(x)}{(1-\nu^2)}h & 0 & 0 \\ 0 & 0 & 0 & 0 & -\frac{E(x)}{12(1-\nu^2)}Rh^3 & 0 \\ 0 & 0 & 0 & 0 & 0 & \frac{E(x)}{12(1-\nu^2)}Rh^3 \end{bmatrix} \quad (3.32)$$

The propagation constants of the FGM shell (solid lines) are compared to the uniform shell (dashed lines) in Figure (3.7) in the case when the ratio of the Young's moduli is 10. These characteristics show a principal cut-off frequency at about 2000 Hz for the longitudinal and radial waves and some smaller interference at higher frequencies.

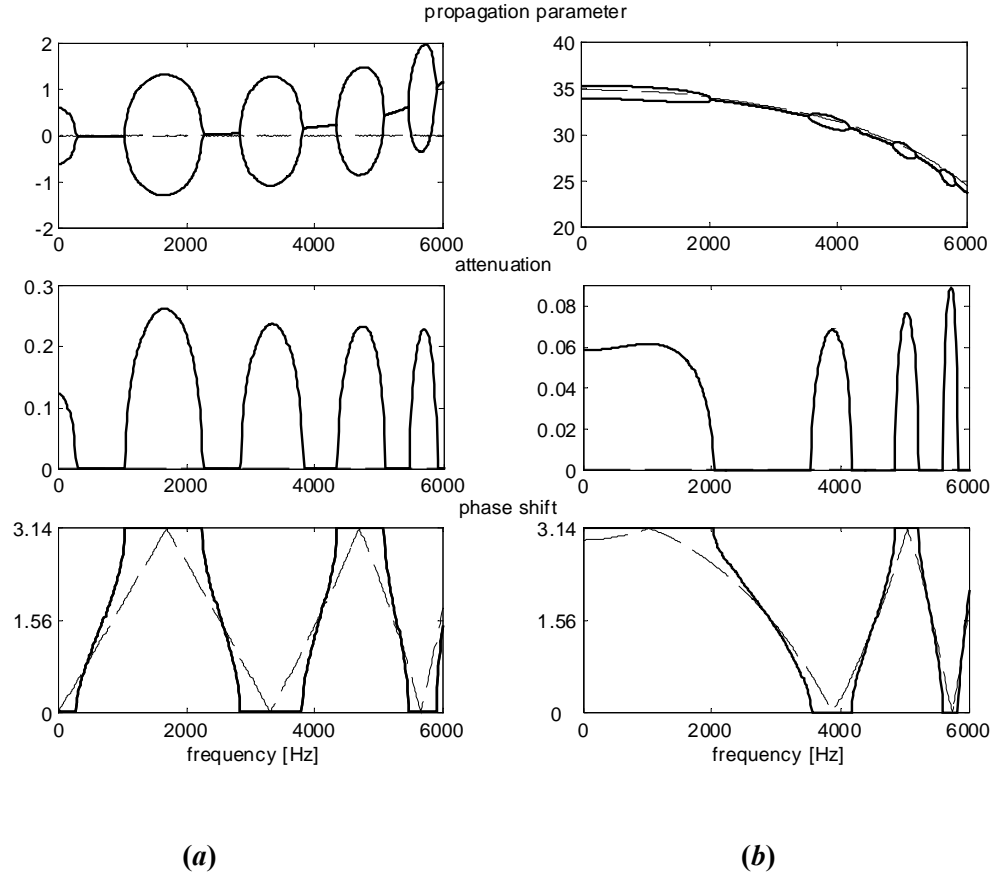


**Figure 3.7: Propagation constants of uniform (dash) and exponential FGM (solid) shells:
 (a) longitudinal direction and (b) radial direction.**

3.3.2.2 FGM Effect: Linear Grading

For a *linear* Young's modulus we have:

$$E(x) = E_0 \left(1 + e \frac{x}{L} \right) \quad (3.33)$$

The parameter e is depends on the modulus ratio:

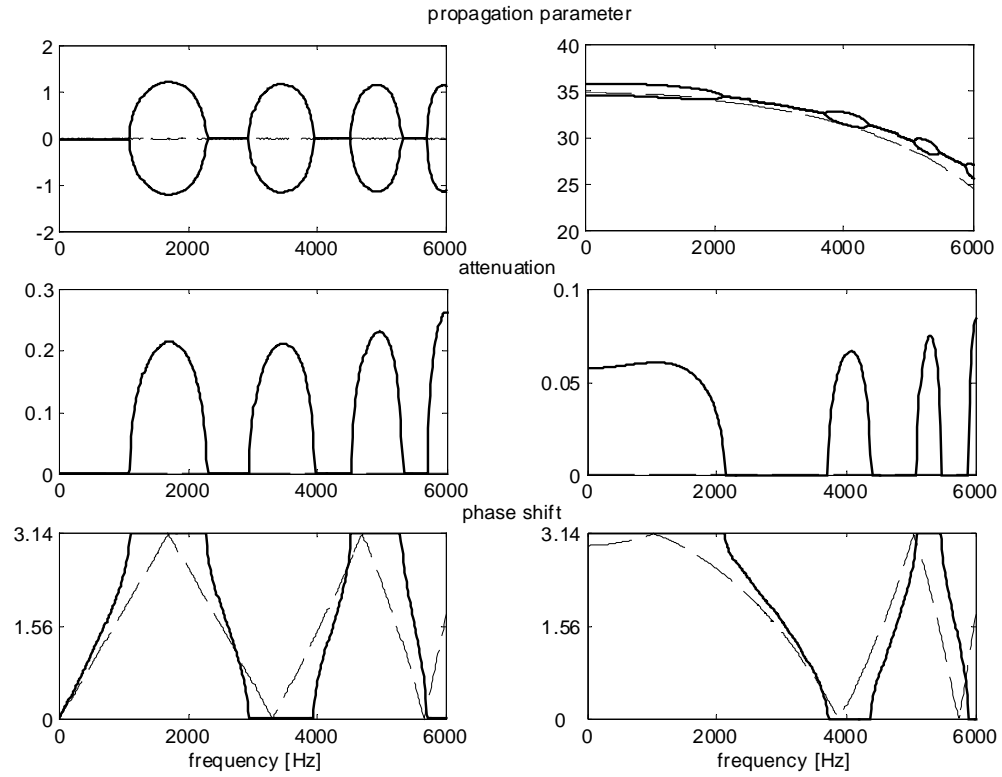
$$e = \sqrt{\frac{E_L}{E_0}} - 1 \quad (3.34)$$

Hence, the general expression for the state-space matrix \mathbf{A} is:

$$[\mathbf{A}(x)] = \begin{bmatrix} 0 & 0 & 0 & 1 & 0 & 0 \\ 0 & 0 & 1 & 0 & 0 & 0 \\ 0 & 0 & 0 & 0 & 0 & 1 \\ -\frac{\omega^2}{c^2} & -\frac{\left(\frac{e}{L}\right)\nu}{\left(1+e\frac{x}{L}\right)R} & -\frac{\nu}{R} & -\frac{\left(\frac{e}{L}\right)}{\left(1+e\frac{x}{L}\right)} & 0 & 0 \\ 0 & \left(\frac{12}{h^2}\right)\left(\frac{\omega^2}{c^2} - \frac{1}{R^2}\right) & 0 & -\frac{12\nu}{Rh^2} & -2\frac{\left(\frac{e}{L}\right)}{\left(1+e\frac{x}{L}\right)} & 0 \\ 0 & 0 & 0 & 0 & 1 & 0 \end{bmatrix} \quad (3.35)$$

where we notice the main difference with (3.31) is the term $A[5,6]=0$ because the second derivative of the linear profile vanishes.

The propagation constants for the shell of Table (3.1) can be plotted in the frequency domain, as shown in Figure (3.8). The characteristics are very similar to those obtained for the exponentially graded shell (Figure (3.7)). More precisely, a cut-off frequency at about 2000 Hz in the radial direction is still present in the FGM characteristics (solid line).



(a)

(b)

Figure 3.8: Propagation constants of shells with linearly varying Young's modulus:

(a) longitudinal direction and (b) radial direction.

3.3.3 Combined Effect

Lastly, one can combine the effect of the geometric taper with the functionally graded Young's modulus in order to have more control over the propagation characteristic of the shell. The resulting system matrix $[A]$:

$$[\mathbf{A}(x)] = \begin{bmatrix} 0 & 0 & 0 & 1 & 0 & 0 \\ 0 & 0 & 1 & 0 & 0 & 0 \\ 0 & 0 & 0 & 0 & 0 & 1 \\ -\frac{\omega^2}{c^2} & -\nu A_{42} & -\nu A_{43} & -A_{44} & 0 & 0 \\ 0 & A_{52a} \frac{\omega^2}{c^2} - A_{52b} & 0 & -\nu A_{54} & -2A_{55} & -A_{56} \\ 0 & 0 & 0 & 0 & 1 & 0 \end{bmatrix} \quad (3.38)$$

where

$$A_{42} = \frac{\left(\frac{g}{R}\right)_x}{g} = \frac{E_x}{ER} + \frac{h_x}{Rh} ,$$

$$A_{43} = \frac{1}{R} = \frac{2}{D_0 - h} ,$$

$$A_{44} = \frac{g_x}{g} = \frac{E_x}{E} + \frac{R_x}{R} + \frac{h_x}{h} ,$$

$$A_{52a} = \frac{g}{q} = \frac{12}{h^2} ,$$

$$A_{52b} = \frac{g}{qR} = \frac{12}{Rh^2} ,$$

$$A_{54} = \frac{g}{qR^2} = \frac{12}{(Rh)^2} ,$$

$$A_{55} = \frac{q_x}{q} = \frac{E_x}{E} + \frac{R_x}{R} + 3\frac{h_x}{h} ,$$

$$\text{and } A_{56} = \frac{q_{xx}}{q} = \frac{E_{xx}}{E} + 2\frac{E_x}{E} \frac{(Rh^3)_x}{Rh^3} + \frac{(Rh^3)_{xx}}{Rh^3} . \quad (3.39)$$

A numerical comparison among three different possibilities has been carried out and obtained results are displayed in Figure (3.9). In all the characteristics, Young's modulus is assumed to be linearly decreasing. The dashed line denotes the response of a shell with uniform thickness, where as the dotted line defines the performance of a shell with linearly decreasing thickness and the solid line is corresponding to shells with linearly increasing thickness.

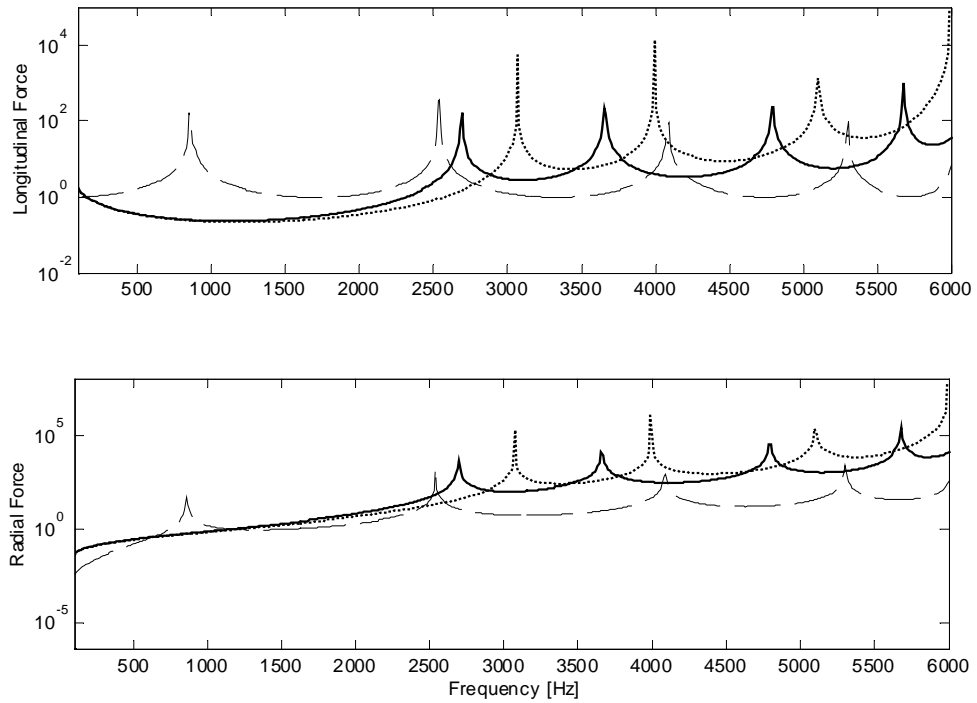


Figure 3.9: Frequency response:
(dash) uniform thickness, (solid) same slope, (dot) opposite slope.

As expected, the combined effect of decreasing Young's modulus and decreasing thickness gives the largest stop band. As a result of this analysis, we can conclude that it is possible to effectively control the spectral location and width of the stop bands over a wider range of frequency spectrum, with proper selection of geometrical and material parameters.

3.4 Experimental Characteristics of Shells with Varying Geometry

A series of experiments are carried out in order to validate the numerical results presented in Section 3.3. Manufacturing considerations suggested keeping the internal diameter constant and letting the outer profile be linearly varying. Dimensions and material properties of the shell used in the experiments have been summarized in Table (3.1). One of the two PVC shells has uniform profile while the other is tapered with a geometric ratio $A_L / A_0 = 4$. Figure (3.10) shows photographs of the shells used.



(a)

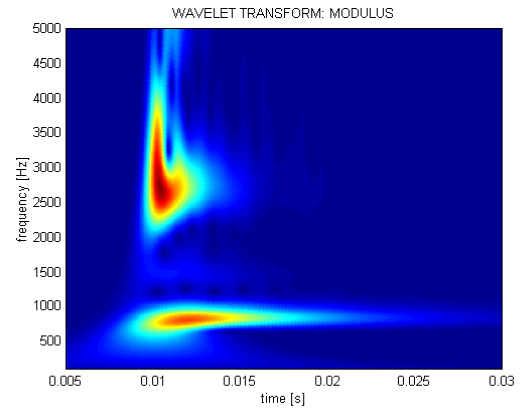
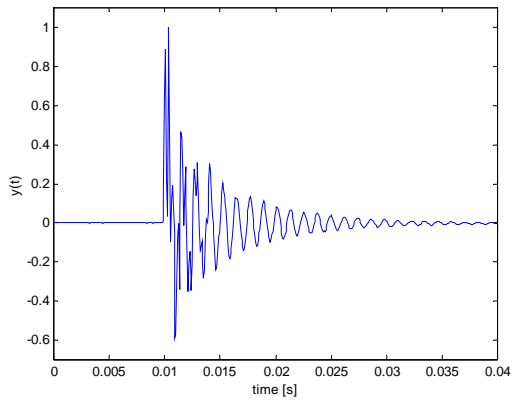


(b)

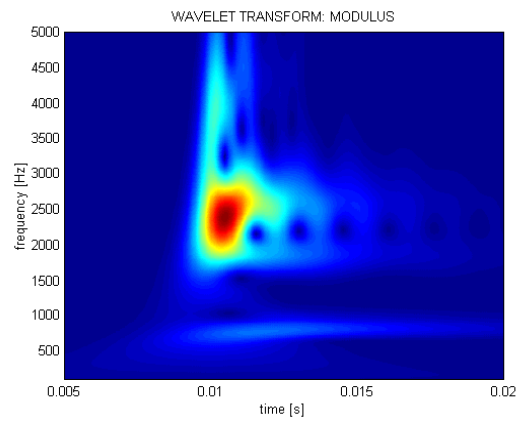
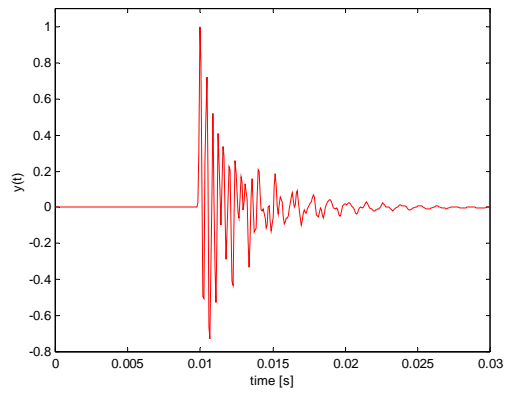
Figure 3.10: (a) uniform shell and (b) tapered shell.

An impact hammer (PCB Model 086C02) is used to exert a longitudinal impulsive excitation on one end of the shell. The longitudinal acceleration at the shell end opposite to the force location is captured by a piezoelectric accelerometer (PCB Model 303A03). The spectrum analyzer (ONO SOKKI Model CF910) is triggered by the input force. The analyzer is used to record the signal coming from the accelerometer for 30 milliseconds. The stored transient response is analyzed through the Wavelet Transform (WT) in order to capture the energy content associated with the propagation spectrum. The WT allows for displaying the energy distribution simultaneously in the time and frequency domain and hence allows for fully describing the filtering characteristics of the considered classes of shells. Results are displayed in Figure (3.11).

Figure (3.11a) shows that the uniform profile propagates sinusoidal waves with no dispersion. The energy looks equally distributed about the two most significant peaks at approximately 900 Hz and 2500 Hz. On the other hand, the tapered profile, pictured in Figure (3.11b), deforms the impulsive wave as time progresses. This reflects the shift in the energy content as represented by the WT plot to higher frequencies. Also, most of the energy is concentrated about the 2500 Hz peak and the peak at 900 Hz has been significantly cut off. These results confirm the prediction obtained by the numerical model and displayed in Figure (3.6).



(a)



(b)

Figure 3.11: Experimental Time Response and Wavelet Transform of shells:

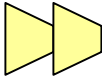
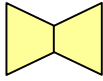
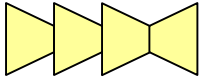
(a) uniform thickness and (b) tapered profile.

3.5 Periodic Shells with Tapered Elements

Further improvements in the wave propagation characteristics can be obtained by connecting a series of tapered shell elements. It is proved [43] that elements whose length is comparable to the diameter perform better than very long elements. Therefore, for a medium radius of 0.87 in. (Table (3.1)), the length of the tapered element is limited to about 2 inches.

Three different configurations are investigated and each of them brings different improvements. Table (3.2) shows the different configurations considered in the study.

Table 3.2: Periodic Tapered Elements.

Single sub-element	Two sub-elements	Bi-periodic
Type(A) 	Type(B) 	Type(C) 

The characteristics of configuration (A) have already been discussed in details in Section 3.3.1. The shorter length of the element amplifies the width of the stop bands while periodicity amplifies the amount of the energy redistribution. Figure (3.12) represents the characteristics of the tapered element with solid lines and the uniform characteristics in dashed. The principal cut-off frequency has increased to about 1.5 kHz. Another stop band is located at about 3.6 kHz. Figure (3.13) displays the overall effect on the frequency response of a periodic shell with four consecutive cells.

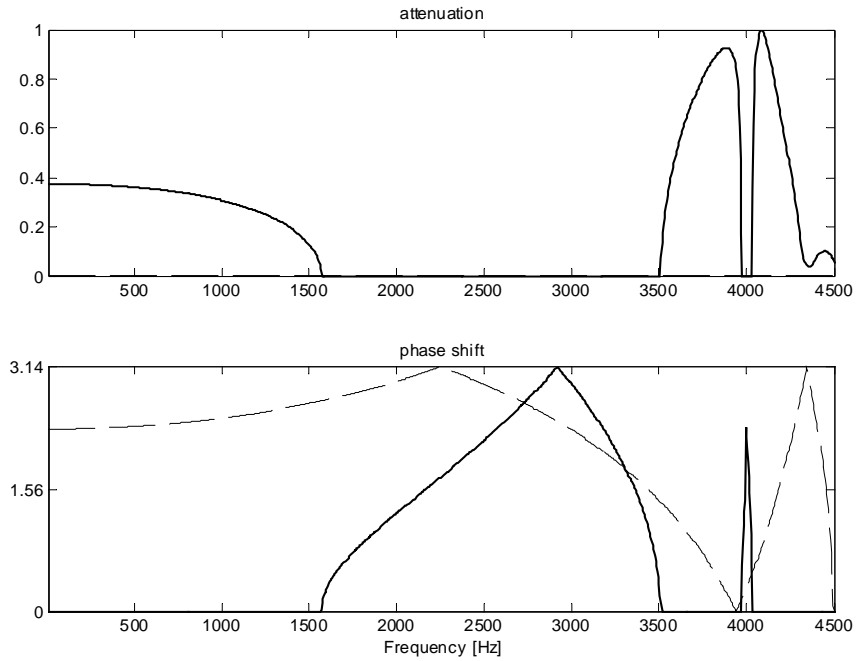


Figure 3.12: Propagation characteristics of a periodic tapered shell type (A).

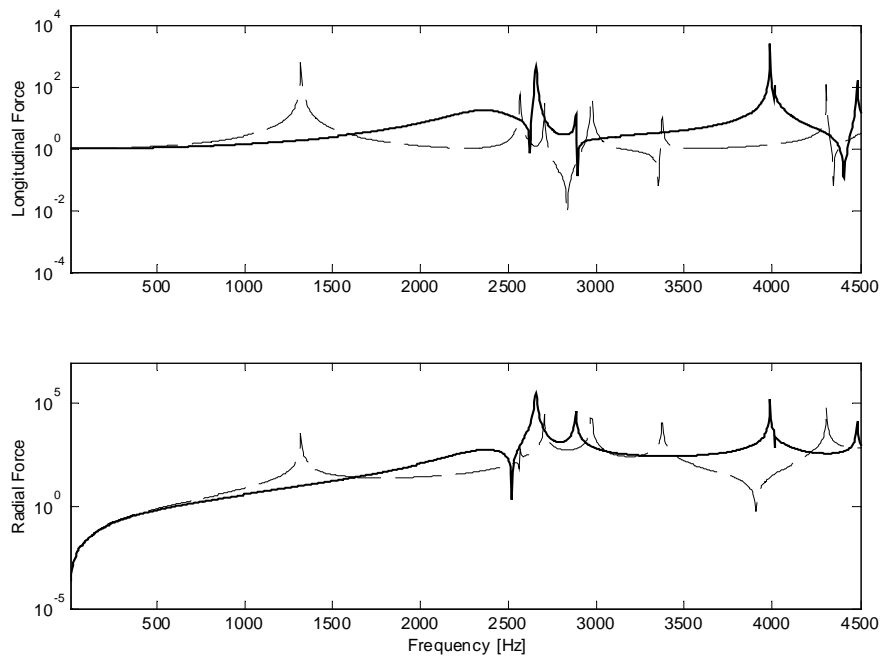


Figure 3.13: Transmitted force: type (A) tapered shell (solid) and uniform shell (dashed).

Configuration (B) consists of two tapered sub-elements of opposite taper ratio. Although it appears to be less effective than type (A) at lower frequencies, the characteristics portrayed in Figure (3.14) show that there is a principal stop band around 2.5 kHz whereas the type (A) has a pass band (Figure (3.12)).

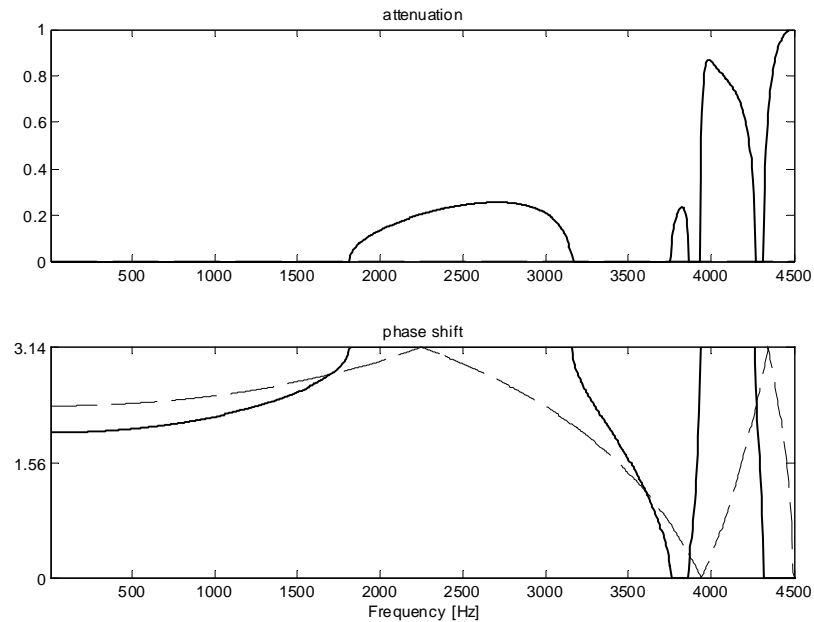


Figure 3.14: Propagation characteristics of a periodic tapered shell type (B).

Figure (3.15) displays the overall effect on the frequency response of a periodic shell with 4 consecutive type (B) cells. Although the first natural frequency is not affected by this configuration, all peaks between 2 kHz and 3.5 kHz vanish.

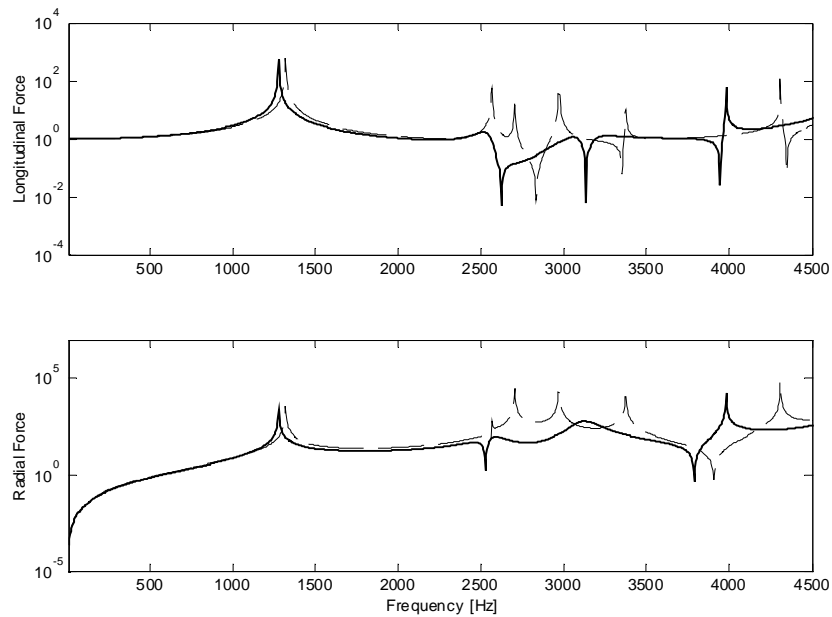


Figure 3.15: Transmitted force: type (B) tapered shell (solid) and uniform shell (dashed).

The bi-periodic configuration (C) allows for attempting a combination of the effects shown in the two previous cases. The bi-periodic cell consists of three sub-elements with the same taper ratio followed by one with opposed taper ratio.

The characteristics are displayed in Figure (3.16). The principal stop band at low frequencies that was observed in type (A) characteristics (Figure (3.12)) is combined with the mid-frequencies stop band similar to the one of Figure (3.13) (type (B) element).

The overall frequency response of a periodic shell with 2 consecutive bi-periodic cells appears in Figure (3.17). Only disturbance about 3 kHz can effectively propagate along the shell.

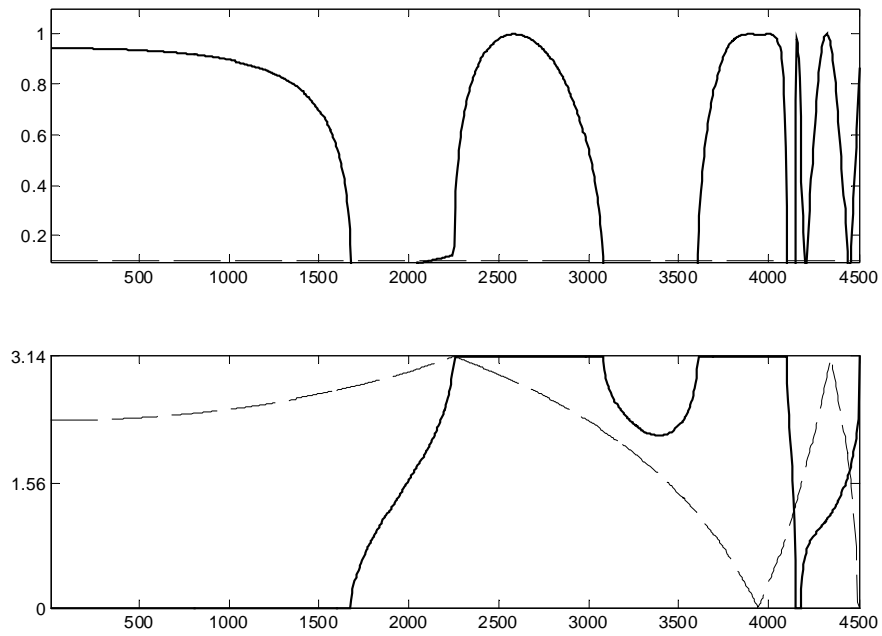


Figure 3.16: Propagation characteristics of a periodic tapered shell type (C).

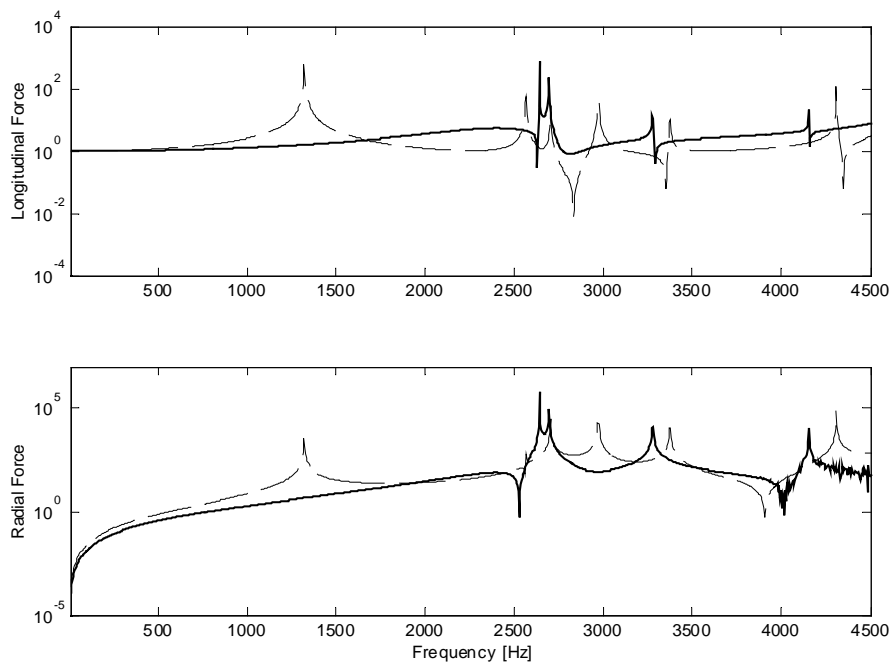


Figure 3.17: Transmitted force: type (C) tapered shell (solid), uniform shell (dashed).

3.6 Conclusions

Variation of the thickness of a shell can be effectively used to filter out undesirable bands of wave propagation frequencies. The main parameter that influences the width of the stop bands is the ratio between the cross sections at the two ends of the shell. We can also state that there are no significant improvements of the propagation characteristics when more complex profiles are implemented. The latter result is very important from a practical point of view since linear tapers are much easier to machine with traditional machinery and they can result in significant attenuation as much more complex geometries.

Very similar results have been obtained with a variation of Young's Modulus using functionally graded materials. Such materials can be very helpful in environments where the geometry of the structure impose design constraints, which cannot be modified. Besides, it may be easier to obtain a much higher ratio. Finally, by combining the two effects one can obtain the flexibility needed for some very demanding applications.

Periodicity is also considered. Different taper configurations (same ratio versus opposite ratio) proved to have complementary effects on the wave characteristics that can be successfully combined in bi-periodic tapered cells. This complex geometry can produce the most effective energy redistribution.

CHAPTER 4: WAVE PROPAGATION IN PERIODIC ROTATING SHAFTS WITH DIFFERENT GEOMETRIES

4.1 Introduction

Rotational motion is one of the oldest developments in the human history, and rotating flexible shafts are one of the most commonly employed mechanical elements for power transmission in industrial applications and automotive and aeronautic engineering. In each case, an accurate vibration analysis and stability behavior of the rotating shaft is essential for the success of the machine performance.

The first published work on dynamics of rotating shafts was presented in 1869 by Rankine [40]. According to Gunter [16], Rankine's neglect of Coriolis acceleration led to erroneous conclusions that confused engineers for half a century. The number of publications on dynamics of rotating shafts increased exponentially after the 40s. Over these early years most rotating machinery were traditionally designed to operate below the first natural transverse frequency of the shaft (or critical speed) in order to ensure reliable operation. For this reason, the earliest papers were mainly focused on predicting the first critical velocity of shafts for different practical configurations and they would suggest methods on balancing shafts for the *sub-critical operation range*.

Modern rotating machinery, however, often must operate at much higher speeds, far in excess of the first critical velocity (*super-critical range*); therefore, more recent literature [14, 23, 26, 34] treats a wider set of problems and phenomena, such as the

proximity of operating speed to higher order criticals, the extent of unstable regions and fatigue stresses, investigating both experimental data and FEM models. In general, three beam theories are commonly employed to examine the transverse vibrations of rotating flexible shafts. These are the Timoshenko's model, where both the rotary inertia and shear deformation effects are accounted for, Rayleigh's model, which considers only the rotary inertia, and Euler-Bernoulli's beam. Timoshenko and Rayleigh models also include conservative gyroscopic moments generated by the rotation of the shaft about its longitudinal axis, resulting in a non-self-adjoint problem. As more exact analyses are required, it is recognized that the Timoshenko theory gives the most accurate predictions.

Kuang and Tan [24] obtained an exact solution for the free and forced response of a stepped, rotating Rayleigh shaft by the distributed transfer function method and a generalized displacement formulation. Murphy [36] developed a polynomial transfer matrix method to improve the efficiency in analyzing the eigenvalues problem and the unbalance response of multi-element rotors. Curti *et al.* [10] investigated the steady-state unbalance response of a continuous rotor on anisotropic supports by using a FEM model based on Timoshenko theory. The development of lightweight, stiff, extended boring bars for metal cutting operations motivated the work by Kim *et al.* [21], who performed a free vibration analysis of a rotating tapered filament-wound composite shaft, showing that, by tapering, the bending natural frequencies and stiffness of the shaft can be significantly increased over those of a uniform shaft of the same volume and material. The same results are confirmed by Scott and Kim [44], who further investigate the wave propagation characteristics of the same composite shaft. Suzuki *et al.*[50] proposed an analytical solution to the problem of free vibrations of rotating tapered shells by power

series expansion in the particular case of clamped-clamped boundary conditions. Numerical results illustrate the effect of thickness variation upon natural frequencies and mode shapes.

An innovative point of view is introduced by Kang and Tan's description of the vibration of rotors in terms of propagating and attenuating waves in waveguides. First, they investigate the general problem of flexural waves propagation by considering an infinitely long axially strained rotating Timoshenko shaft [19]. Also, in a second work [54], they examine the effect of the axial strain on the wave reflection and transmission characteristics under arbitrary geometric discontinuities, supports and boundary conditions.

In this chapter, a literature survey on the problem of rotordynamics has been given in Section 4.1. Section 4.2 develops a detailed analysis of the different components of a rotor. The equations of motion and the transfer matrix of a generic shaft are derived from the energy conservation using Lagrange's equations in Section 4.3. Section 4.4 addresses the problem of critical speeds and the concept of Campbell diagrams. Section 4.5 introduces a finite element formulation to evaluate the wave characteristics and stability problems in rotordynamics. Section 4.6 displays the numerical results for tapered profiles as well as periodic geometries. It also deals with possible combinations of the two effects in order to optimize the bandwidth and location of the stop bands. Section 4.7 presents the experimental results and validates the numerical predictions for the tapered

shaft and the stepped periodic shaft. Section 4.8 introduces the effect of damping material. The drawn conclusions are summarized in Section 4.9.

4.2 Lateral Shaft Problems

This section refers to Lalanne and Ferraris [26], who give a very detailed derivation of the governing equations of a generic rotor.

The basic elements of a rotor are the disk, the shaft, the bearings and seals; the inherent mass unbalance must also be considered to complete the analysis.

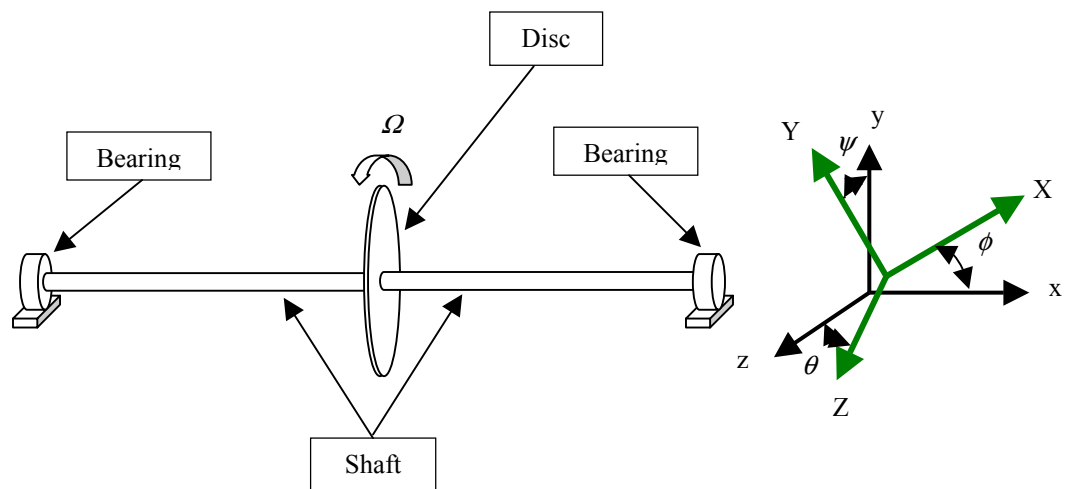


Figure 4.1: Sketch of a complete rotor.

The kinetic energy T , potential strain energy U and virtual work δW due to external disturbances F are written for each element and Lagrange's equations are generated as follows

$$\frac{d}{dt} \left(\frac{\partial T}{\partial \dot{q}_i} \right) - \frac{\partial T}{\partial q_i} + \frac{\partial U}{\partial q_i} = F q_i \quad ; \quad i = 1..N \quad (4.1)$$

where N are the degrees of freedom, q_i the generalized independent coordinates.

4.2.1 The disk

The disk is usually assumed rigid; therefore it is simply characterized by its kinetic energy. Recalling the instantaneous angular speed vector ω

$$\omega = \begin{bmatrix} \omega_x \\ \omega_y \\ \omega_z \end{bmatrix} = \begin{bmatrix} \dot{\phi} + \psi \sin \theta \\ \dot{\theta} \cos \phi - \dot{\psi} \cos \theta \sin \phi \\ \dot{\theta} \sin \phi + \dot{\psi} \cos \theta \cos \phi \end{bmatrix} \quad (4.2)$$

Assuming that the angular speed Ω is constant, the angles θ and ψ are small and the disk is symmetric and isotropic, we can simplify the kinetic energy as

$$T_{Disk} = \frac{1}{2} M_D (\dot{u}^2 + \dot{w}^2) + \frac{1}{2} I_{zD} (\dot{\theta}^2 + \dot{\psi}^2) + \frac{1}{2} I_{xD} \Omega^2 + I_{xD} \Omega \dot{\psi} \theta \quad (4.3)$$

where the last term represents the gyroscopic effect (Coriolis acceleration) with M_D and I_D denoting the mass and mass moment of inertia of the disk respectively. Also, u and w denote the transverse deflections in the x and z direction.

4.2.2 The shaft

The flexible shaft is represented by a generic beam with circular cross section with kinetic energy T_{Shaft} and strain energy U_{Shaft} . A possible axial force F_{axial} is taken into account because it may seriously affect the dynamical behavior of the system. Moreover, the hypotheses of symmetry, isotropy and linearity are still assumed as valid, but the rotary inertia is taken into account (Timoshenko beam) in the kinetic energy.

$$T_{Shaft} = \frac{1}{2} \int_0^L \rho S (\dot{u}^2 + \dot{w}^2) dx + \frac{1}{2} \int_0^L \rho I (\dot{\theta}^2 + \dot{\psi}^2) dx + \rho L \Omega^2 + 2\Omega \int_0^L \rho I \dot{\psi} \theta dx \quad (4.4)$$

where ρ , L , S and I denote the density, length, cross-section and moment of inertia of the shaft respectively. Also, u and w denote the transverse deflections in the x and z direction.

The strain energy becomes:

$$U_{Shaft} = \frac{1}{2} \int_0^L EI \left[\left(\frac{\partial^2 u}{\partial x^2} \right)^2 + \left(\frac{\partial^2 w}{\partial x^2} \right)^2 \right] dx + \frac{1}{2} \int_0^L F_{axial} \left[\left(\frac{\partial^2 u}{\partial x^2} \right)^2 + \left(\frac{\partial^2 w}{\partial x^2} \right)^2 \right] dx \quad (4.5)$$

4.2.3 Bearings and seals

The bearings are supposed rigid. Hence, the virtual work δW due to their viscous and elastic forces is neglected in this analysis, or

$$\delta W = \delta W_{Bearings} + \delta W_{Seals} \cong 0 \quad (4.6)$$

4.2.4 Mass unbalance

The unbalance can be related to manufacturing tolerances and misalignments among the geometric and inertial centers of the various elements of the rotor. It is generally defined as a small additional mass m_u , which is eccentric to the geometric center of the shaft by a distance ε . The associated kinetic energy can be approximated as:

$$T_{Unbalance} \cong m_u \Omega \varepsilon (\dot{u} \cos \Omega t - \dot{w} \sin \Omega t) \quad (4.7)$$

where $T_{Unbalance}$ denotes the so-called “centrifugal vector” and it will be considered as an external excitation to the perfectly centered structure.

4.3 Equations of Motion

The problem is now solved for the simple case of a single shaft on rigid bearings. The analysis takes into account various geometries, as sketched in Figure (4.2).

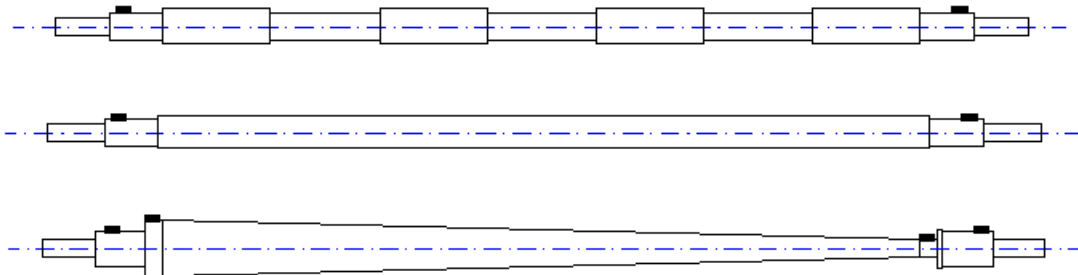


Figure 4.2: Sketch of a periodic, uniform and tapered shaft.

For this structure, one can collect the following terms:

$$\begin{aligned} \mathbf{T} &= \mathbf{T}_{Shaft} + \mathbf{T}_{Unbalance} \quad , \\ \mathbf{U} &= \mathbf{U}_{Shaft} \quad , \\ \text{and} \quad \delta \mathbf{W} &= 0 \quad . \end{aligned} \tag{4.7}$$

The Lagrange's equations are applied to system of equation (4.7)

$$\begin{aligned} \frac{d}{dt} \left(\frac{\partial \mathbf{T}}{\partial \dot{q}_1} \right) - \frac{\partial \mathbf{T}}{\partial q_1} + \frac{\partial \mathbf{U}}{\partial q_1} &= 0 \quad , \\ \text{and} \quad \frac{d}{dt} \left(\frac{\partial \mathbf{T}}{\partial \dot{q}_2} \right) - \frac{\partial \mathbf{T}}{\partial q_2} + \frac{\partial \mathbf{U}}{\partial q_2} &= 0 \quad , \end{aligned} \tag{4.8}$$

where $q_1 = u$ and $q_2 = w$. These result in the following equations of motion of the system:

$$\begin{aligned} \rho S(x) \ddot{u}(x, t) - \rho I(x) \Omega \dot{w}(x, t) + \frac{d^2}{dx^2} (EI(x) u_{,xx}(x, t)) &= m_u \Omega^2 \varepsilon u(x_u, t) \sin(\Omega t) \quad , \text{ and} \\ \rho S(x) \ddot{w}(x, t) + \rho I(x) \Omega \dot{u}(x, t) + \frac{d^2}{dx^2} (EI(x) w_{,xx}(x, t)) &= m_u \Omega^2 \varepsilon w(x_u, t) \cos(\Omega t) \quad . \end{aligned} \tag{4.9}$$

System (4.9) can be put in a spectral form in terms of a sole complex variable $W(x, t)$ as vectorial sum of its components u and w ,

$$W(x, t) = [u(x, t) + iw(x, t)] = U(x) e^{i\omega t} \quad , \quad \text{such that}$$

$$\rho S(x)\ddot{W} + \rho I(x)\Omega\dot{W} + \frac{d^2}{dx^2}(EI(x)W_{,xx}) = m_u\Omega^2\varepsilon W_u [\sin(\Omega t) + \cos(\Omega t)] \quad (4.10)$$

Applying the separation principle, the state-space spectral formulation is obtained:

$$\begin{pmatrix} 0 & 1 & 0 & 0 \\ 0 & 0 & 0 & 1 \\ -\frac{g}{qc^2}(\omega^2 + \Omega^2) - \frac{\rho I}{q}\Omega\omega & 0 & -\frac{q_{,x}}{q} & -\frac{q_{,xx}}{q} \\ 0 & 0 & 1 & 0 \end{pmatrix} \begin{Bmatrix} U \\ U_{,x} \\ U_{,xxx} \\ U_{,xx} \end{Bmatrix} = \begin{Bmatrix} 0 \\ 0 \\ 1 \\ 0 \end{Bmatrix} F \quad (4.11)$$

The state vector $U(x)$ corresponds to the configuration where the first two components are the *generalized displacements* (transverse w , slope $w_{,x}$), while the last couple reflects the *generalized forces* (shear Q , bending moment M) in the shaft. Equation (4.11) can now be cast into “Transfer Matrix” representation. First of all, we define a coordinate *transformation matrix* \mathbf{G}_x as follows:

$$Y(x) = \mathbf{G}_x U(x) \quad (4.12)$$

where

$$Y(x) = \begin{Bmatrix} U \\ U_{,x} \\ Q \\ M \end{Bmatrix} \text{ is the } \textit{transfer vector at location } x$$

and $\mathbf{G}_x = \begin{bmatrix} 1 & 0 & 0 & 0 \\ 0 & 1 & 0 & 0 \\ 0 & 0 & -D_t(x) & 0 \\ 0 & 0 & 0 & D_t(x) \end{bmatrix}$ is the *transformation matrix at location x*.

Solutions to the dynamics of equation (4.10) are calculated by the integration of equation (4.11) over the length of the shaft, such that

$$U(L) = e^{\int_0^L [\mathbf{A}(x)] dx} U(0) \quad (4.13)$$

One finally gets to the following *Transfer Matrix Representation* of the dynamics of the shaft:

$$Y_L = \left[\mathbf{G}_L e^{\int_0^L \mathbf{A}(x) dx} \mathbf{G}_0^{-1} \right] Y_0 = \mathbf{T} Y_0 \quad (4.14)$$

where $\begin{cases} (x=0) \Rightarrow Y_0 = [\mathbf{G}_0]U(0) \\ (x=L) \Rightarrow Y_L = [\mathbf{G}_L]U(L) \end{cases}$

From the analysis of the transfer matrix performed in the previous chapters, it can be summarized that:

$$(Y_L)_i = e^{\alpha_i} (Y_0)_i e^{i\beta_i} \quad (4.15)$$

where $\lambda_i = e^{\mu_i} = e^{\alpha_i} e^{i\beta_i}$. Equations (4.15) shows that the disturbance measured at location L is shifted in phase by the factor β (*phase angle*) with respect to the signal measured at location 0 and it is magnified or attenuated by factor α (*decaying amplitude*) depending on the geometric characteristics of the structure and on the amount of wave interference. When the phase β shifts of 180° , destructive interference occurs between the traveling waves and the reflected waves so that no remaining disturbance propagates along the shaft.

4.4 Campbell Diagrams

Traditionally [23], a rough estimate of the first critical speed for practical applications is simple to obtain for simply-supported Jeffcott rotors. In this case, for steady operating conditions, the lowest critical speed Ω coincides with the first natural frequency f_1 of the shaft. In other words,

$$\Omega_{critic} \cong f_1 = \frac{1}{2\pi} \sqrt{\frac{k}{m}} \quad (4.16)$$

where $k = \frac{48EI}{l^3}$, $I = \frac{\pi d^4}{64}$ and $m = \rho\pi l \frac{d^2}{4}$, so that $\Omega_{critic} \cong 0.275 \frac{d}{l^2} \sqrt{\frac{E}{\rho}}$.

A careful study of the critical velocities of a generic rotor can be carried out using FEM or analytic methods [14, 26]. In the latter case, the equations of motion (4.9) can be modified with the transformation $u(x, t) = f_i(x) q_1(t)$ and $w(x, t) = f_i(x) q_2(t)$.

The equations of motion end up being:

$$\begin{aligned} m\ddot{q}_1 - a\Omega\dot{q}_2 + kq_1 &= m_u\Omega^2\epsilon f(x_u)\sin(\Omega t) \quad , \\ \text{and} \quad m\ddot{q}_2 + a\Omega\dot{q}_1 + kq_2 &= m_u\Omega^2\epsilon f(x_u)\cos(\Omega t) \quad . \end{aligned} \quad (4.17)$$

where

$$m = M_{Disk} + \int_0^L f_i(x) [\rho_{Shaft} S(x) f_i(x)] dx \quad \text{is the mass coefficient} \quad ,$$

$$a = a_{Disk} + \int_0^L f_i(x) \left[-\frac{\partial^2}{\partial x^2} (\rho_{Shaft} I(x) f_i(x)) \right] dx \quad \text{is the gyroscopic effect} \quad ,$$

$$k = K_{Disk} + \int_0^L f_i(x) \left[\frac{\partial^2}{\partial x^2} \left(E_{Shaft} I(x) \frac{\partial^2}{\partial x^2} f_i(x) \right) \right] dx \quad \text{is the stiffness coefficient} \quad ,$$

and $f_i(x)$ is an *admissible displacement function* of the longitudinal coordinate x for the i^{th} mode shape of the shaft.

For each of the first i^{th} configurations, we can study the Campbell diagram of the shaft, by solving the homogeneous part of equation (4.17) for the rotation speed Ω .

$$\begin{bmatrix} m & 0 \\ 0 & m \end{bmatrix} \begin{Bmatrix} \ddot{q}_1 \\ \ddot{q}_2 \end{Bmatrix} + \begin{bmatrix} 0 & -a\Omega \\ a\Omega & 0 \end{bmatrix} \begin{Bmatrix} \dot{q}_1 \\ \dot{q}_2 \end{Bmatrix} + \begin{bmatrix} k & 0 \\ 0 & k \end{bmatrix} \begin{Bmatrix} q_1 \\ q_2 \end{Bmatrix} = \begin{Bmatrix} 0 \\ 0 \end{Bmatrix} \quad (4.18)$$

The solution $\omega = \omega_{\Omega=0} \pm f(\Omega)$ defines the two critical speeds at which either backward or forward whirl appears. The intersection of these curves with the critical condition, when the rotating speed of the shaft matches an harmonic of the natural frequency of the rotor ($\Omega = n\omega_i$, $n = 1, 2, \dots$), gives the value of the critical speed related to the i^{th} deformed shape. The picture that portraits the natural frequencies versus the rotating speed parameter is called ‘‘Campbell diagram’’.

4.5 Finite Element Formulation

The kinetic energy (4.4) and potential energy (4.5) of a shaft can also be written in terms of $u(x, t) = [N_1(x)]\delta u(t)$ and $w(x, t) = [N_2(x)]\delta w(t)$, which gives the mass [M], stiffness [K] and gyroscopic matrix [G] of a FEM shaft element [26]:

$$\frac{1}{2} \dot{\Delta}^T [M] \dot{\Delta} = \dot{\Delta}^T \left\{ \frac{1}{2} \int_0^L \rho S(x) \begin{bmatrix} N_1^T N_1 & 0 \\ 0 & N_2^T N_2 \end{bmatrix} + \rho I(x) \begin{bmatrix} N_{1,x}^T N_{1,x} & 0 \\ 0 & N_{2,x}^T N_{2,x} \end{bmatrix} dx \right\} \dot{\Delta},$$

$$\frac{1}{2} \Delta^T [K] \Delta = \Delta^T \left\{ \int_0^L \frac{EI(x)}{2} \begin{bmatrix} N_{1,xx}^T N_{1,xx} & 0 \\ 0 & N_{2,xx}^T N_{2,xx} \end{bmatrix} + \frac{F_0}{2} \begin{bmatrix} N_{1,x}^T N_{1,x} & 0 \\ 0 & N_{2,x}^T N_{2,x} \end{bmatrix} dx \right\} \Delta,$$

and
$$\dot{\Delta}^T [G(\Omega)] \Delta = \dot{\Delta}^T \left\{ \int_0^L -\rho \Omega I(x) \begin{bmatrix} 0 & N_{1,x}^T N_{2,x} \\ N_{2,x}^T N_{1,x} & 0 \end{bmatrix} dx \right\} \Delta \quad (4.19a)$$

where $\Delta = \begin{bmatrix} \delta u(t) \\ \delta w(t) \end{bmatrix}$ are the shape function, and $[N_1]$ and $[N_2]$ are the typical cubic displacement polynomial functions for a beam in bending.

Applying Lagrange's principle, in absence of axial force F_0 , allows for obtaining the equation of motion of the i^{th} beam element as

$$[M]_i \ddot{\Delta}_i + [G(\Omega)]_i \dot{\Delta}_i + [K]_i \Delta_i = F_{external} \quad , \quad i = 1..n \quad (4.19b)$$

The system (4.19) can be assembled into the overall governing equation for the whole shaft, or

$$\overline{[M]} \ddot{\Delta} + \overline{[G(\Omega)]} \dot{\Delta} + \overline{[K]} \Delta = \overline{F}_{external} \quad (4.20)$$

4.5.1 Transfer Matrix

A coordinates transformation brings the system (4.19) into the transfer matrix approach. It is convenient to rewrite the equation of motion in terms of the dynamic stiffness

$$[[K] + j\omega[G(\Omega)] - [M]\omega^2] \Delta = F \quad \Rightarrow \quad K_{Dyn} \Delta = F$$

$$\text{Noticing that } \Delta = \{U_{left}; U_{right}\} \quad , \quad F = \{F_{left}; F_{right}\} \quad , \quad K_{Dyn} = \begin{bmatrix} K_{11} & K_{12} \\ K_{21} & K_{22} \end{bmatrix}$$

it is possible to rearrange the system in the transfer matrix approach:

$$\begin{Bmatrix} U_{left} \\ F_{left} \end{Bmatrix}_{i+1} = \mathbf{T} \begin{Bmatrix} U_{left} \\ F_{left} \end{Bmatrix}_i, \quad (4.21)$$

$$\mathbf{T} = \begin{bmatrix} -K_{12}^{-1}K_{11} & K_{12}^{-1} \\ K_{22}K_{12}^{-1}K_{11} - K_{21} & -K_{22}K_{12}^{-1} \end{bmatrix}$$

The transfer matrix approach considers the whole structure as one single *input-output* block that directly relates the right side of the shaft (*output*) to the left side (*input*); hence the whole shaft is divided into one single macro-element, which brings concerns about the accuracy of the analysis [36]. Therefore, higher order polynomials must be considered to improve the accuracy.

The transfer matrix method allows for investigating periodically tapered shafts in a very compact form. In this case, the transfer matrix of the overall structure $[\mathbf{T}_N]$ is equal to the product of the transfer matrices of each element $[\mathbf{T}_i]$:

$$\begin{Bmatrix} U_{left} \\ F_{left} \end{Bmatrix}_N = [\mathbf{T}_N] \begin{Bmatrix} U_{left} \\ F_{left} \end{Bmatrix}_0 \quad (4.22)$$

where $[\mathbf{T}_N] = \prod_{i=1}^N [\mathbf{T}_i]$. The frequency response of the periodic structure is derived applying the proper boundary conditions. In the case of simply-supported shaft, it resolves into

$$\frac{F_{left_N}}{F_{left_0}} = [T_{22_N}] \quad (4.23)$$

where $T_N = \begin{bmatrix} T_{11_N} & T_{12_N} \\ T_{21_N} & T_{22_N} \end{bmatrix}$

4.5.2 Campbell Diagram

The homogeneous part of system (4.20) is taken into consideration while investigating for critical speeds:

$$[[\overline{K}] + j\omega[\overline{G(\Omega)}] - \overline{[M]}\omega^2]\Delta = 0 \quad (4.24)$$

Solving the eigenvalues-problem of (4.24) for different values of the velocity Ω gives the Campbell diagram of the shaft. In this case, the maximum number of whirl speeds obtained depends on the number of finite elements n the shaft is divided into.

4.6 Numerical Results

Different types of geometries are considered in order to clarify their specific waves propagation pattern in comparison with a simple uniform cylindrical shaft.

First, tapered profiles are investigated. Then, periodicity is introduced with stepped cylindrical profiles. Finally, the different geometries are combined with periodicity in order to optimize the wave propagation pattern at low frequencies as well as the bandwidth of the stop bands.

4.6.1 Tapered Shaft

A tapered aluminum shaft is considered and compared to a uniform shaft with the same mass. Detailed schematic drawings of the shafts are represented in Figure (4.3).

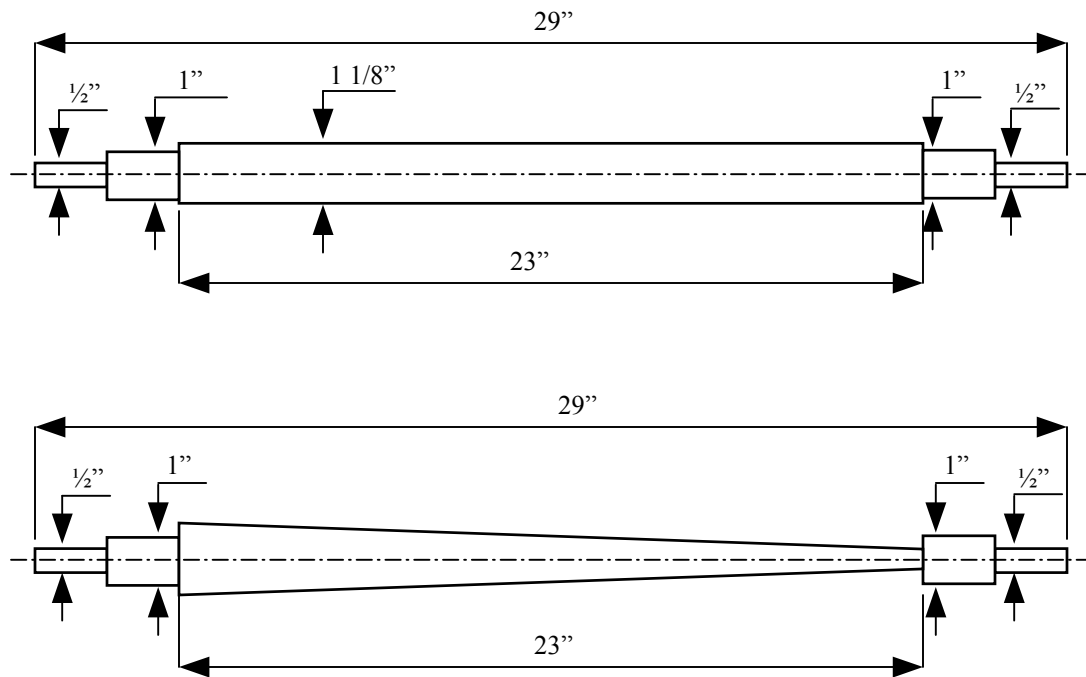


Figure 4.3: Schematic drawing of the tapered and uniform shaft.

Dimensions and material properties are displayed in the following Table (4.1):

Table 4.1: Tapered Shaft Properties

Parameter	Value
Young Modulus [Pa]	71×10^9
Density [Kg/m^3]	2700
Length [mm]	584.2 (23")
Medium Diameter [mm]	28.575 (1 1/8")
Geometric Taper Ratio	4

The propagation characteristics as well as and the Campbell diagram are calculated for the tapered rotor in order to compare its dynamic behavior with that of a cylindrical shaft of equal mass and material properties. Figure (4.4) displays the propagation constants for both shafts. A comparison between the phase shift and the attenuation parameters of the uniform shaft (dashed line) and the tapered shaft (solid line) shows that the tapered profile presents an interesting stop band between 0.9 kHz and 1.7 kHz.

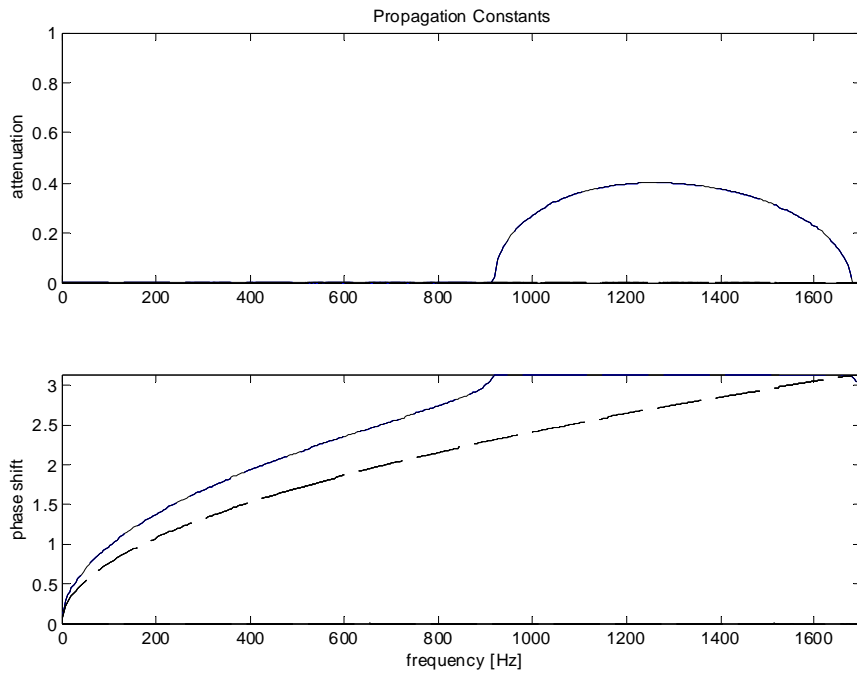


Figure 4.4: Propagation Constants: tapered profile (solid) and uniform profile (dash).

Figure (4.5) portrays the Campbell diagram for the two systems. The tapered profile has lower critical frequencies than the uniform shaft due to the loss of overall rigidity in the narrower section. On the other hand, the area between the backward and

forward whirl curves remains as limited as the uniform shaft, showing similar behavior during transition

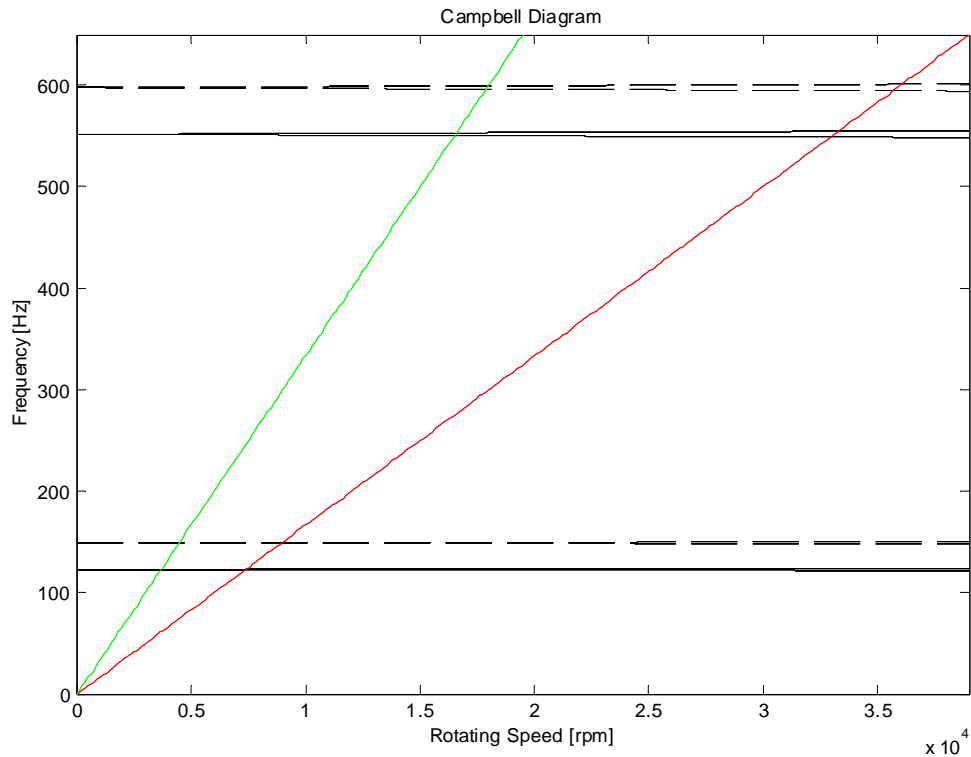


Figure 4.5: Campbell Diagram of a tapered profile (solid line) and uniform profile (dash line).

4.6.2 Periodically Stepped Shaft

A periodically stepped aluminum shaft is taken into consideration and compared to a uniform shaft with the same mass. Dimensions and material properties are displayed in Table (4.2), while a sketch of the shafts is represented in Figure (4.6).

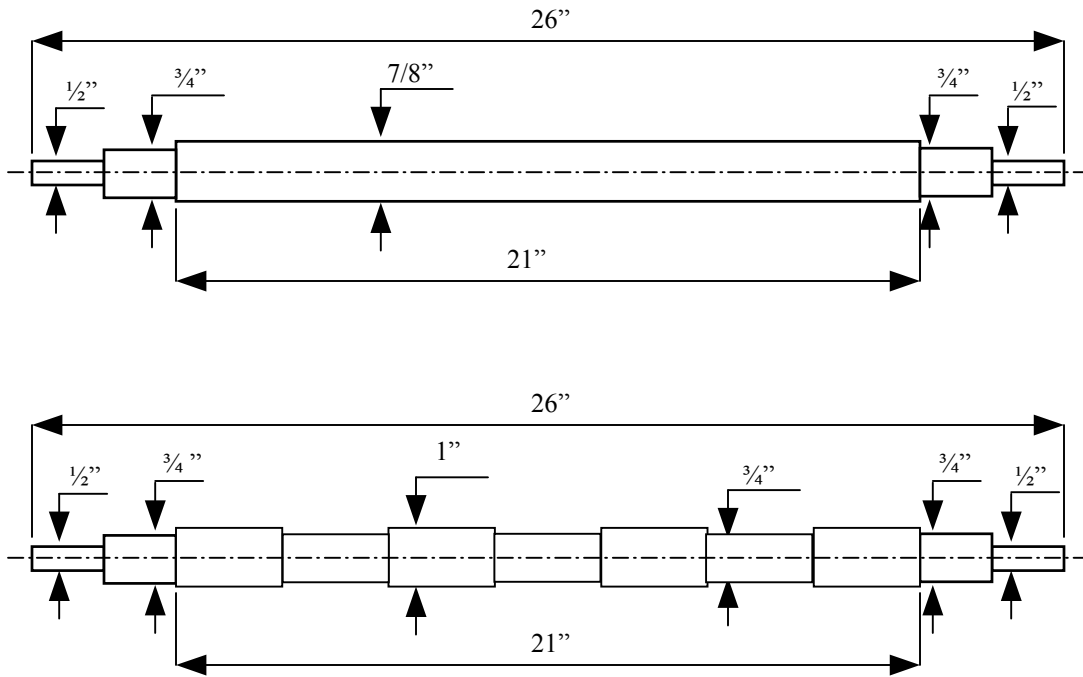


Figure 4.6: Schematic drawing of the stepped and uniform shafts.

Table 4.2: Periodic Shaft Properties.

Parameter	Value
Young Modulus [<i>Pa</i>]	71×10^9
Density [<i>Kg/m</i> ³]	2700
Shaft Length [<i>mm</i>]	533.4 (21")
Medium Diameter [<i>mm</i>]	23.3 (7/8")
Element Diameter Ratio	$\frac{3}{4}$
Element Length Ratio	$\frac{1}{2}$
Element Length [<i>mm</i>]	152.4 (6")

The propagation constants of the periodic rotor are compared with the corresponding characteristics of a cylindrical shaft of equal mass and material properties, as displayed in Figure (4.7). A comparison between the attenuation and the phase shift parameters of the uniform shaft (dashed line) and the periodic shaft (solid line) shows a sharp stop band between 1.1kHz and 1.6kHz. A higher frequency stop band starts around 4.8kHz.

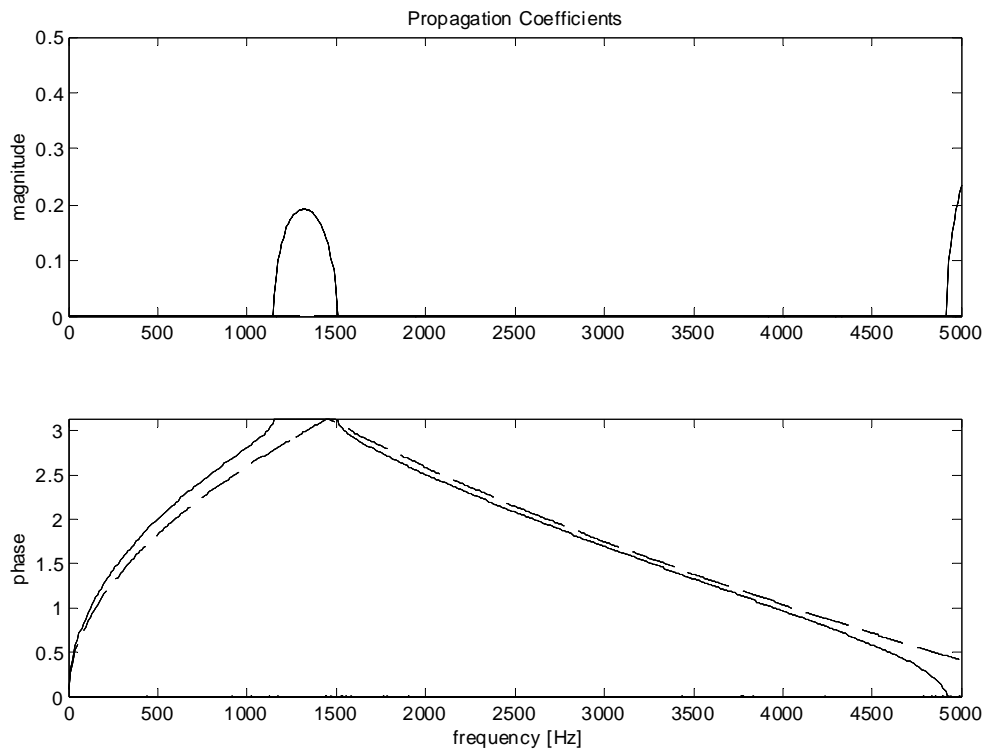


Figure 4.7: Propagation Constants: periodic profile (solid) and uniform profile (dash).

4.6.3 Optimized Geometry: Combined Effect

The major goal of this optimization process is trying to shift the first stop band to lower frequencies and enlarge it as much as possible. Length mismatch between the two sub-elements of the periodic cell is used as an effective way to lower the frequency at which the stop band appears. Then, a tapered sub-element is introduced in order to combine the filtering effects of periodicity with that of tapered profiles.

The length of the large section is increased in order to create a length mismatch in the wave-guide. The best compromise between width and amplitude of the stop band is found with an element length ratio of 5. Also, the cell length was slightly increased from 6" to 8". It has to be noticed that higher diameter ratio is more effective in stopping the wave propagation. Indeed, a combination of steps and tapered profiles optimizes the performance of the shaft. A sketch of the final periodic tapered cell is represented in Figure (4.8).

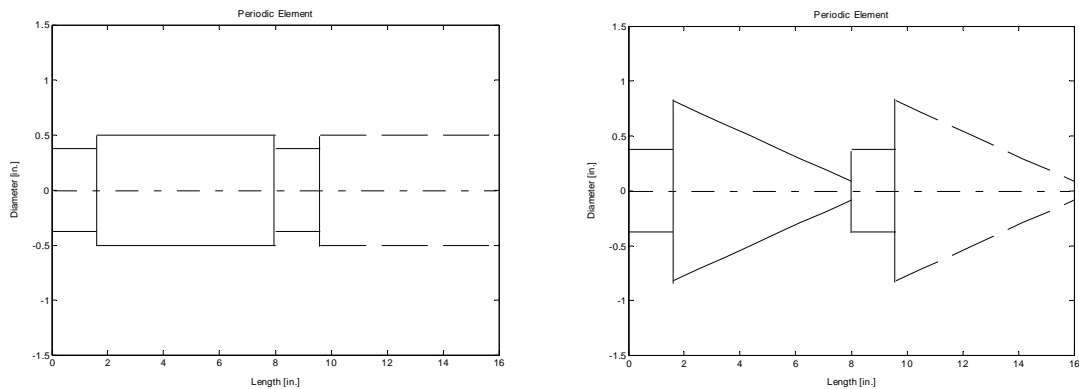
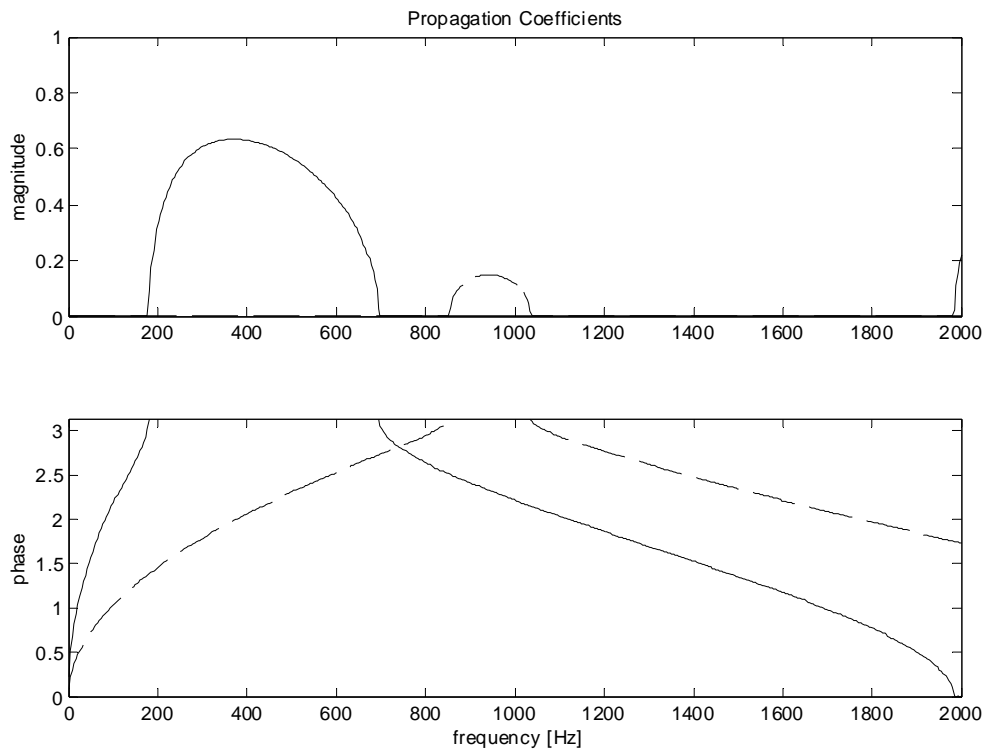


Figure 4.8: Sketch of the stepped profile and the stepped-tapered profile.

In comparison to the periodic shaft of Figure (4.7) (where the two sub-elements have same length), Figure (4.9) shows the stop band of the optimized stepped profile (dashed line) moves about 500Hz to lower frequencies. However, after introducing a linearly tapered sub-element (taper ratio = 10), the same stop band has shifted 1kHz back in frequency and consistently grows in magnitude (solid line). Also the second stop band considerably shifts back in frequency and it starts now at only 2kHz instead of 5kHz.



**Figure 4.9: Propagation Constants with length mismatch:
stepped-tapered profile (solid) versus stepped profile (dash).**

4.7 Experimental Results

A series of experiments on the shafts displayed in Figures (4.3) and (4.6) are carried out in this chapter in order to validate the numerical predictions from the previous section.

4.7.1 Tapered Shaft

Table (4.1) and Figure (4.3) summarize the dimensions and material properties of the shafts used in this experiment, and the setup is shown in Figure (4.10a-b). The rotors consist of two axis-symmetric aluminum shafts (AISI-6061), one of which linearly tapered, simply supported by two ball-bearing cages. At one end, a pulley connects the shaft to an AC motor ($\frac{1}{2}$ HP@3450rpm) by mean of a V-belt (ratio 2/1), while the other end is connected to a piezoelectric shaker (Wilcoxon Research Model D60H). The asynchronous AC motor is used to drive the shaft at a constant speed, and a Variac device allows for adjusting the rotating speed by varying the AC input voltage to the motor.

The shaker, driven by a high-voltage power amplifier (Trek Model 50/750), exerts a lateral excitation (random noise / sine sweep) on the shaft through a small radial ball bearing. Two piezoelectric accelerometers (PCB Model 303A03) are placed on the bearings mounts at each end of the shaft, in order to capture the disturbance transmitted by the rotor. The spectrum analyzer (SRS Model SR780) is triggered to the input force and records the frequency response at the accelerometer locations. Two laser sensors (NAIS Model ANL2500A) is used to capture the lateral vibration directly on the shaft.

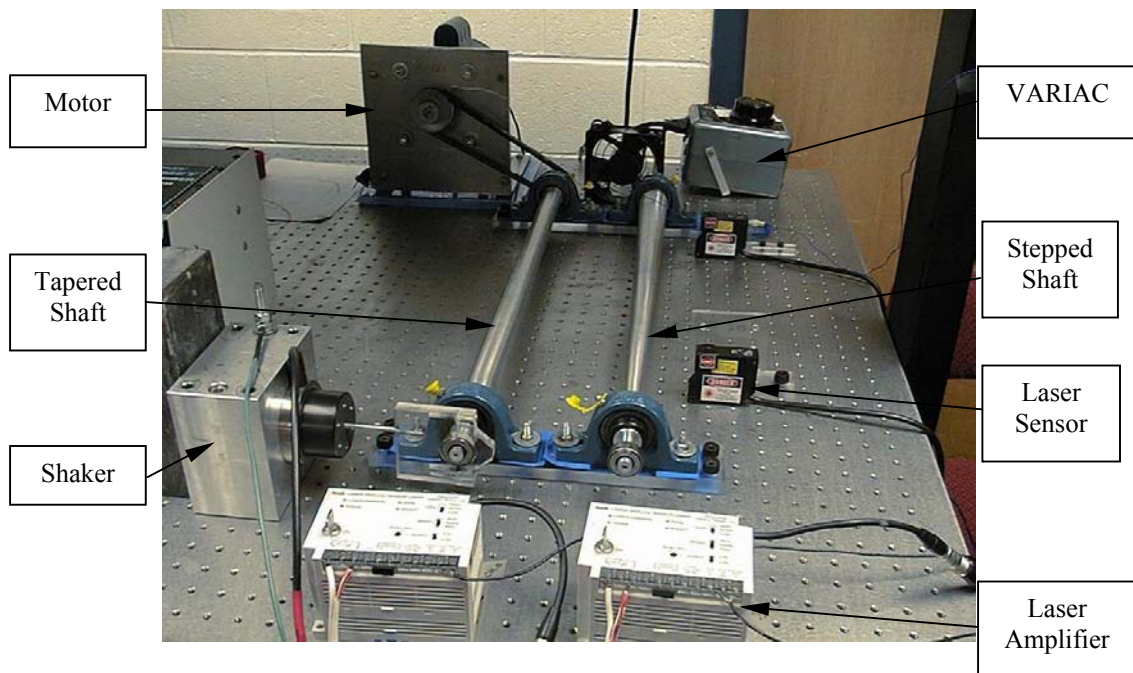


Figure 4.10a: Experimental setup.

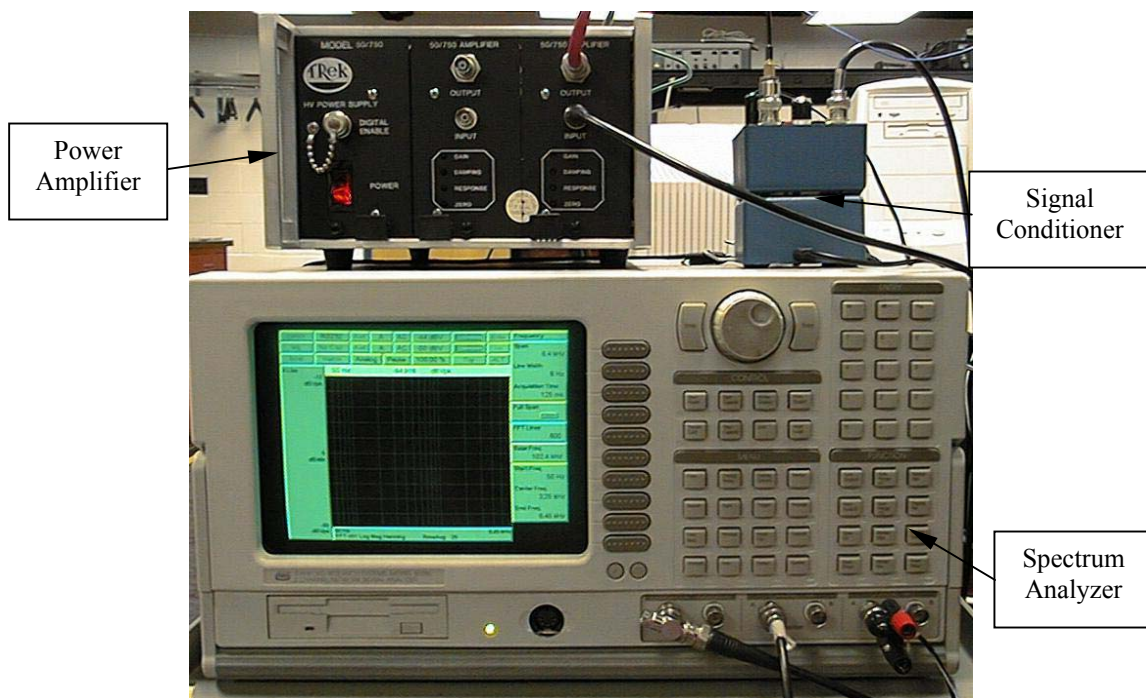


Figure 4.10b: Power Amplifier and Spectrum Analyzer.

At first, the non-rotating frequency responses of the two shafts are captured, in order to have a preview of the system behavior. Figure (4.11) compares the frequency response of the two different rotors. Some attenuation can be observed between 900Hz and 1.4kHz, which corresponds to the predicted stop band (Figure 4.4).

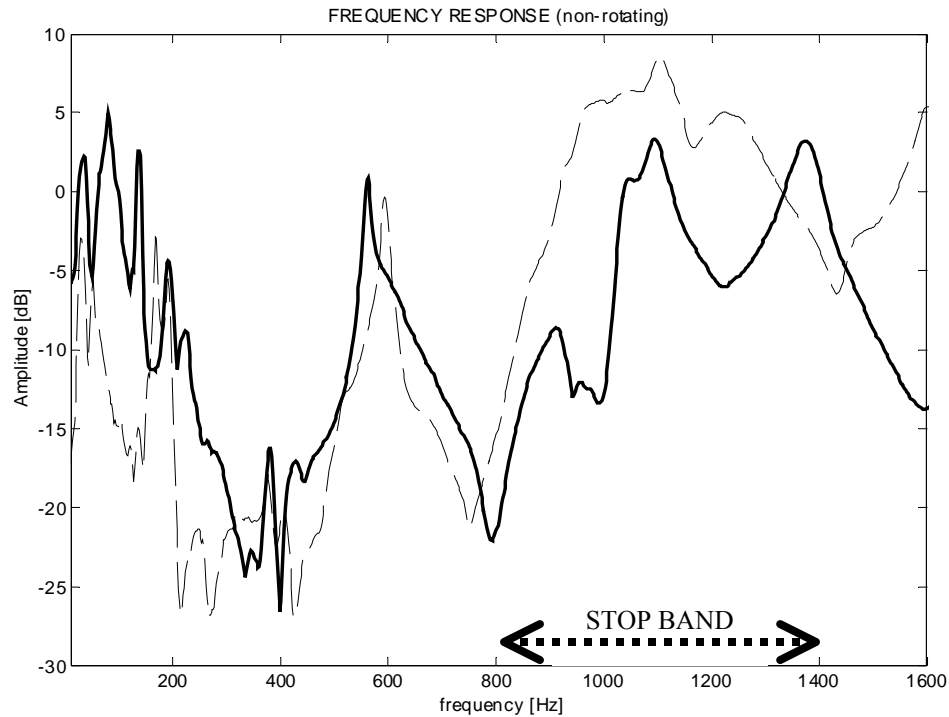


Figure 4.11: Non-rotating shaft: frequency response of the tapered profile (solid) and uniform profile (dash).

Figure (4.12) displays the frequency response of the shafts when their rotation speed is about 84Hz. Higher harmonics of the rotation speed are clearly evident in the picture, as the motor and the ball bearings are found to introduce considerable noise in the accelerometers readings. Nonetheless, it has to be noticed how the tapered profile shows a stop band between 900Hz and 1.5kHz in good agreement with predictions obtained in Section 4.6 (Figure 4.4).

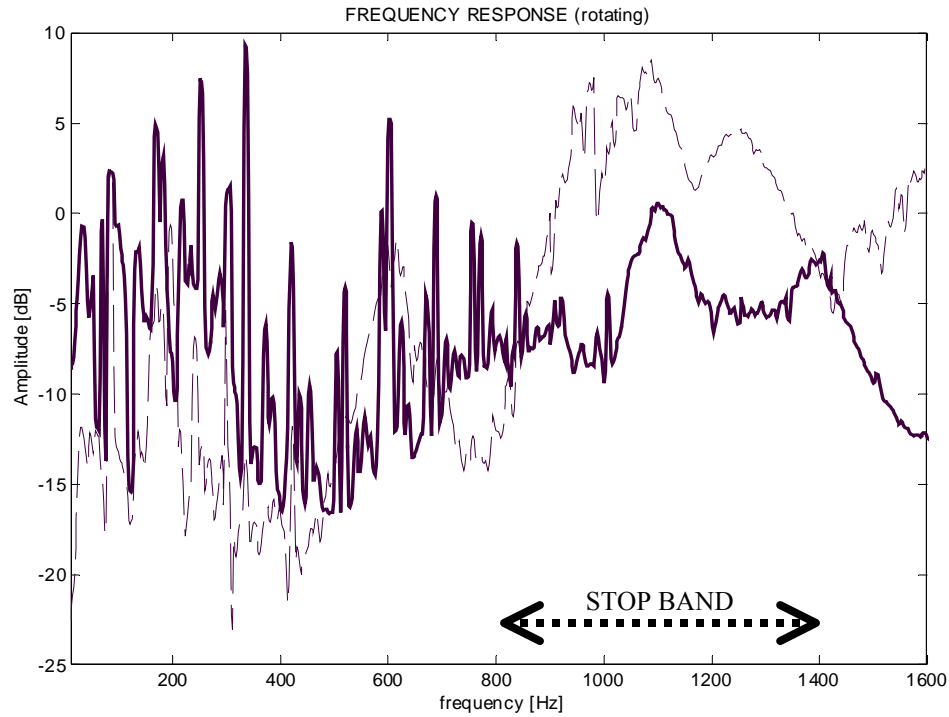


Figure 4.12: Rotating shaft: Frequency response of the tapered profile (solid) and uniform profile (dash).

4.7.2 Periodically Stepped Shaft

Figure (4.6) and Table (4.2) summarize dimensions and material properties of the shafts used in the experiments. A photograph of the setup is shown in Figure (4.13). The rotors consist of two axisymmetric aluminum shafts (AISI-6061), one of which is stepped and is simply-supported by two ball-bearing. At one end, an asynchronous AC motor drives the shaft at a constant speed by mean of pulleys and V-belt, while the other end is connected to an electromagnetic shaker (Wilcoxon Research Model F4). A Variac is used for adjusting the rotating speed of the motor.

The shaker, driven by a power amplifier (Wilcoxon Research Model PA7C), exerts a lateral excitation on the shaft through a small radial ball bearing. A piezoelectric accelerometer (PCB Model 303A03) is placed on the bearing support at each end of the shaft, in order to capture the transmitted disturbance along the rotor. The spectrum analyzer (SRS Model SR780) of Figure (4.10b) is triggered to the input force and records the frequency response at the accelerometer locations.

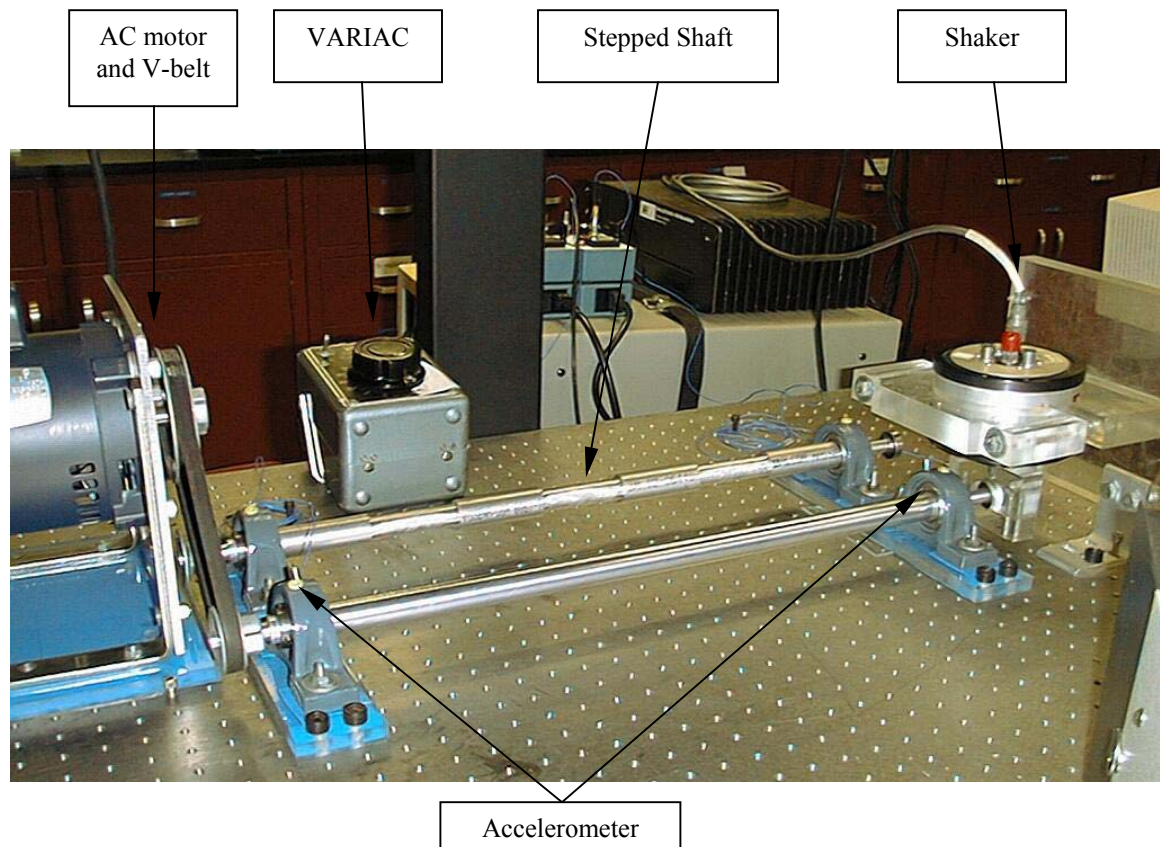


Figure 4.13: Experimental setup for the stepped and uniform shaft.

At first, the non-rotating frequency responses of the two shafts are captured, in order to have a preview of the system behavior. Figure (4.14) shows a stop band is

present between 1kHz and 1.8kHz and a second stop band starts at about 4.8kHz. This result is in good agreement with the theoretical propagation constants obtained in Section 4.6.2 and reported in Figure (4.7).

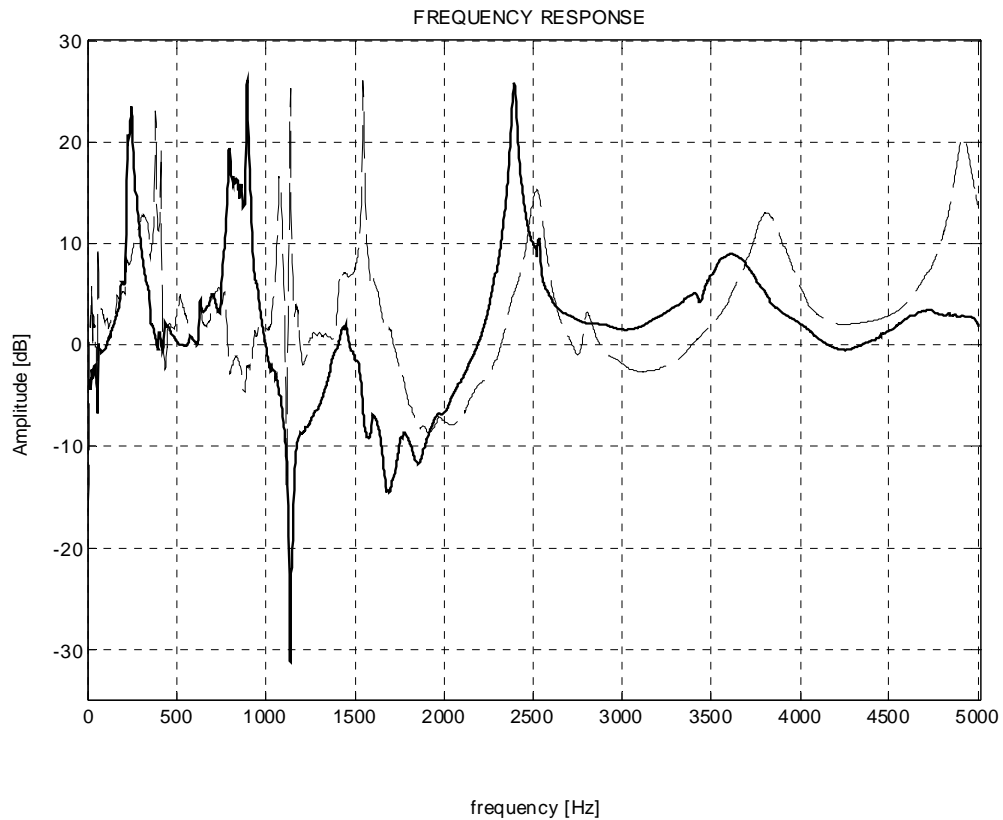


Figure 4.14: Non-rotating shaft: Frequency response of the periodic profile (solid) and uniform profile (dash).

Once again, when the shaft is set into rotation at constant speed of 83 Hz, considerable noise is introduced in the frequency response as can be seen in Figure (4.15). However, the comparison between the response of the uniform shaft (dash)

and the stepped shaft (solid) still shows good attenuation in the same regions (1kHz-1.8kHz and after 4.8kHz), as predicted by Figure (4.7).

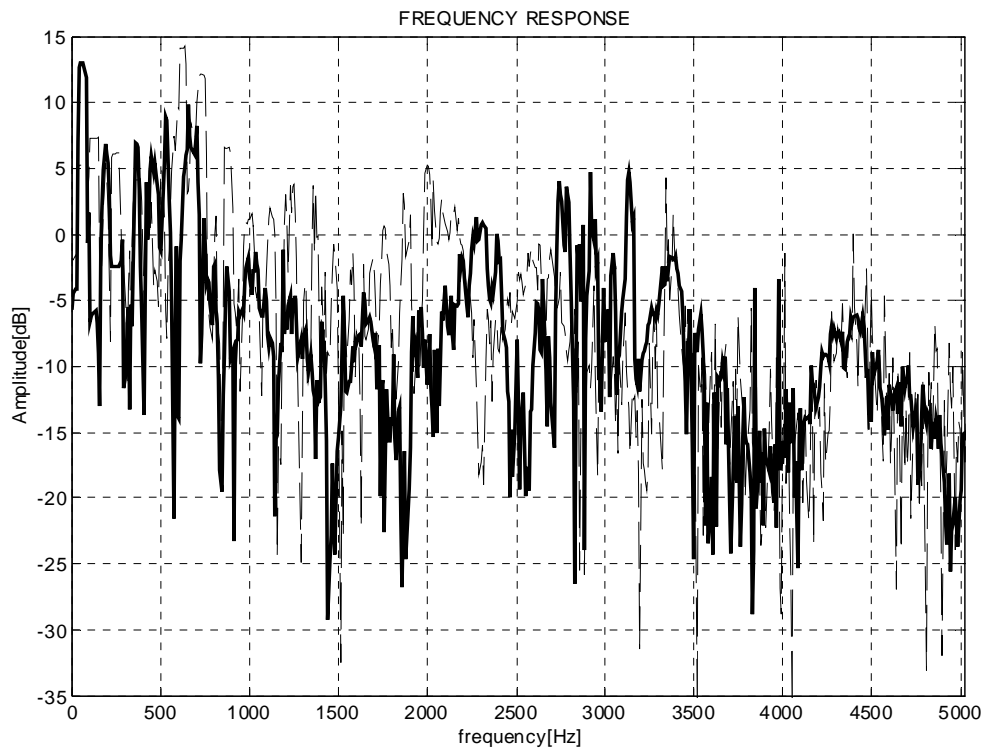


Figure 4.15: Rotating shaft: Frequency response of the periodic profile (solid) and uniform profile (dash).

4.8 Alternative Optimization: Effect of Viscoelastic Inserts

In Section 4.6.3 it is noticed that, shifting the stop bands to lower frequencies, comes at the expense of localizing the stresses due to the abrupt change in geometry and of using rather extreme taper ratios.

In this section, viscoelastic material is used as an additional way to increase the broadband filtering capabilities of the periodic structures and improve the structural integrity of the smaller sections. The thinner elements of the stepped periodic shaft in Figure (4.6) are coated with a layer of commercial Neoprene rubber 1/8 inch thick. The properties of the viscoelastic coating are listed in Table (4.3):

Table 4.3: Neoprene Properties.

Parameter	Value
Young Modulus [Pa]	3.6×10^9
Density [Kg/m³]	1150
Width [mm]	76.2 (3")
Thickness [mm]	3.18 (1/8")

The theoretical propagation characteristics and the experimental frequency response of the coated shaft are compared to the performance of the stepped periodic shaft and the uniform shaft tested in Section 4.6.2.

First, the preliminary data is collected from the non-rotating case. Each of the three shafts are suspended in a free-free boundary condition, as shown in Figure (4.16).

The shafts are then excited at one end by a piezoelectric shaker (Wilcoxon Research Model D60H) driven by the high voltage power amplifier (Trek Model 50/750) of Figure (4.10b). An accelerometer (PCB Model 303A03) is placed at each side of the shaft. The responses to sine sweep and random noise excitations are measured and the transfer function is computed by the spectrum analyzer (SRS Model SR780).

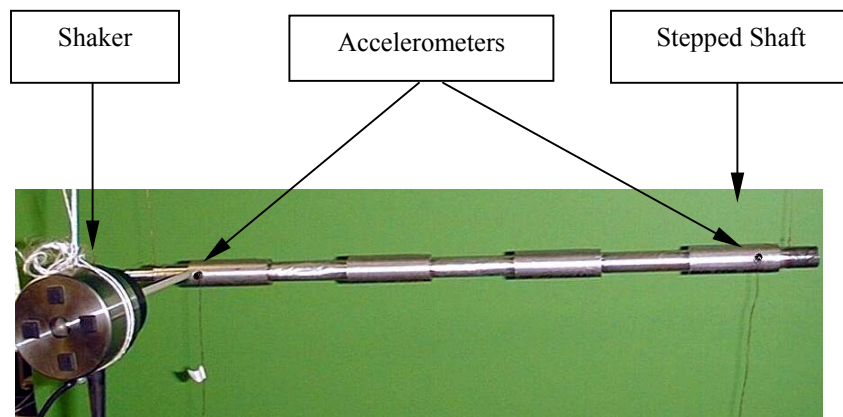


Figure 4.16: Experimental setup of the shaft with free-free boundary conditions.

Figure (4.17) presents the predicted propagation characteristics and the experimental frequency responses for the three different shafts: dashed lines are used to indicate the uniform shaft, thin solid lines for the stepped shaft, and thick solid lines for the rubber-coated shaft.

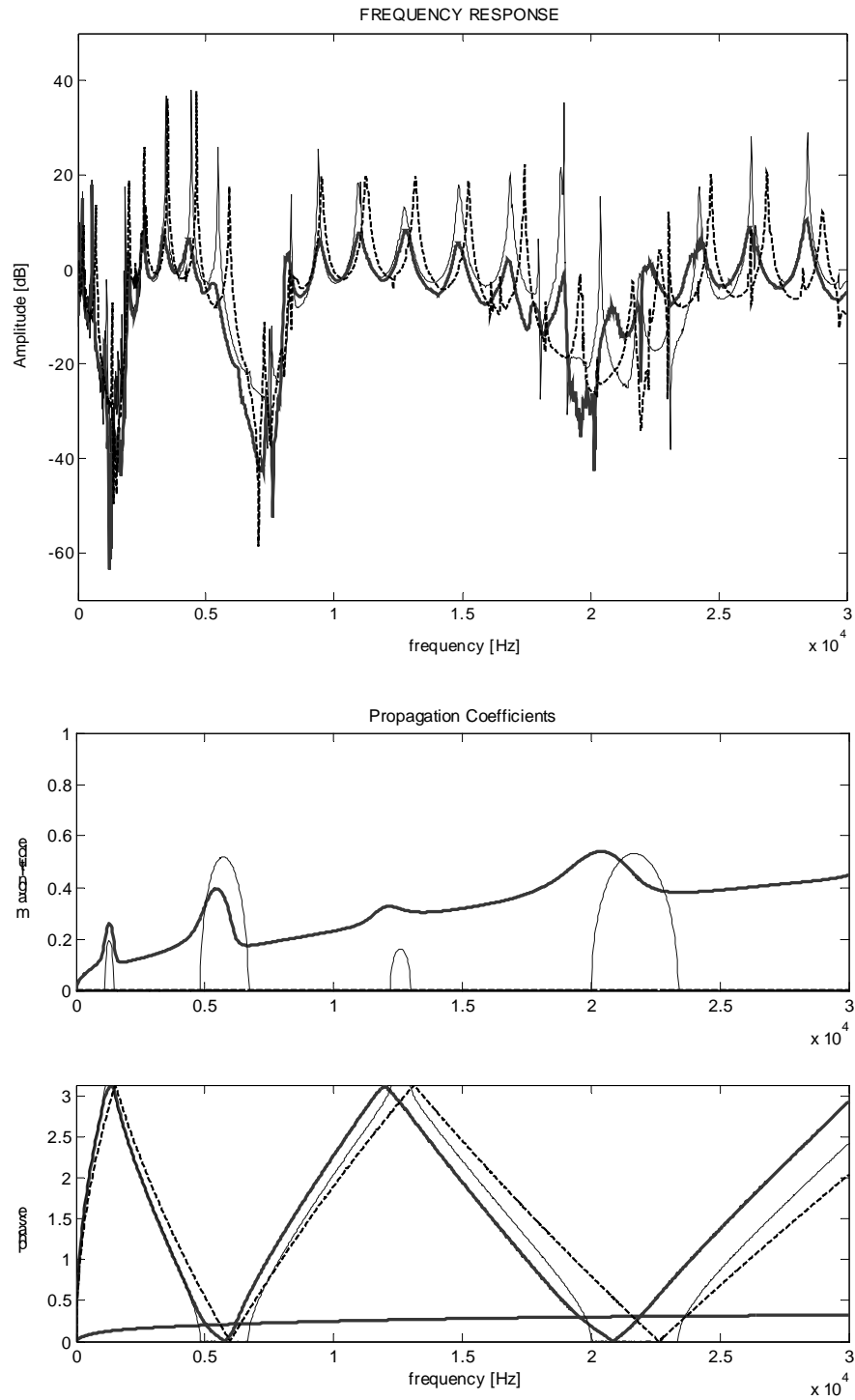


Figure 4.17: Broadband frequency response and propagation characteristics of the non-rotating uniform shaft (dash), stepped periodic shaft (thin solid) and rubber-coated shaft (thick solid).

The stepped shaft shows three main stop-bands around 1.1-1.5kHz, 4.8-6.5kHz and 20-23kHz and a smaller one at 12-13kHz. Note that the two lower stop-bands have already been measured in Sections 4.6, as shown in Figure (4.7).

The coated shaft adds to these four stop bands a broadband effect due to the internal viscous dissipation that extends over the entire frequency range. This effect is responsible of rounding all the peaks corresponding to the natural frequencies of the shaft.

Figure (4.17) presents also the means to verify the numerical predictions against the experimental results. Very good agreement is evident between theory and experiment even at high frequencies (above 9-10kHz) where the Euler-Bernoulli beam element used in the numerical model becomes a rough approximation of the physical phenomenon.

Another series of experiments are carried out with the shaft rotating at constant speed. Figure (4.18) displays the experimental setup. An adequate source of vibration is provided by an epicyclic gearbox (ratio $\frac{1}{2}$) driven by an asynchronous AC motor ($\frac{1}{2}$ HP@2450rpm). The output of the gearbox is secured to one end of the shaft with a rigid connecting sleeve, while a bearing supports the other end of the shaft. Because this bearing provides a severe source of disturbance, a more sophisticated data sampling and analysis is needed in order to clearly identify the filtering capabilities of the three different rotors without introducing any other source of noise.

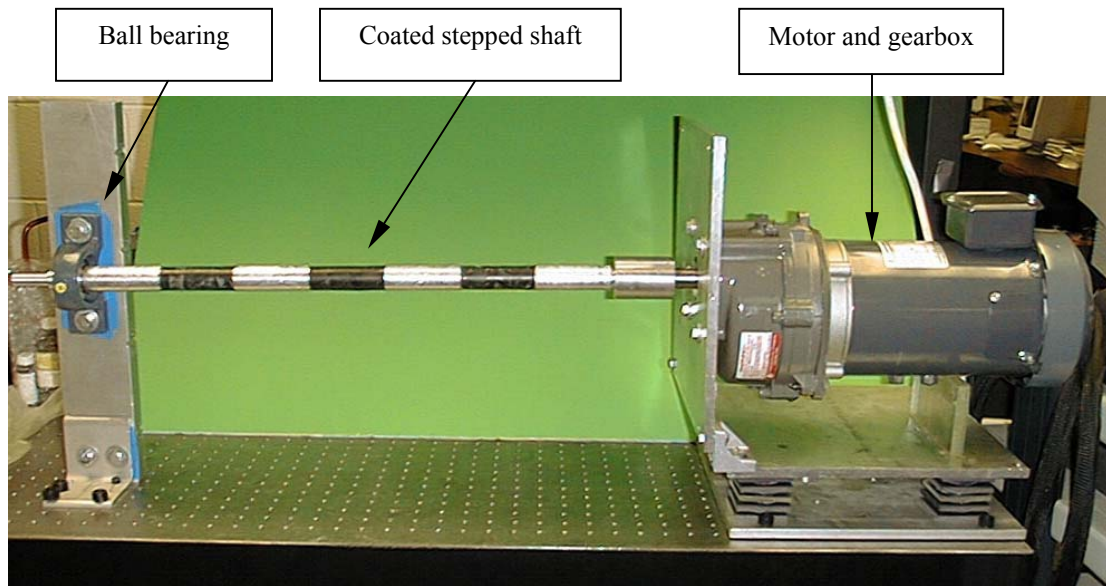


Figure 4.18: The rubber-coated rotor and the experimental setup for the rotating case.

A laser vibrometer (Polytech Vibrascan PSV200) is utilized to scan a mesh of about 200 points evenly distributed along the entire length of the shaft. A color-map displays a live picture of the displacements intensity on the scanned surface. The yellow color identifies the highest vibration intensity while quiet areas are in purple and blue.

Figure(4.19) gives the color-map distribution of the vibration of the three shafts. It is evident that the darker zones (low vibration zones) get wider as we move from the uniform profile to the periodic rotor, to the rubber-coated shaft.

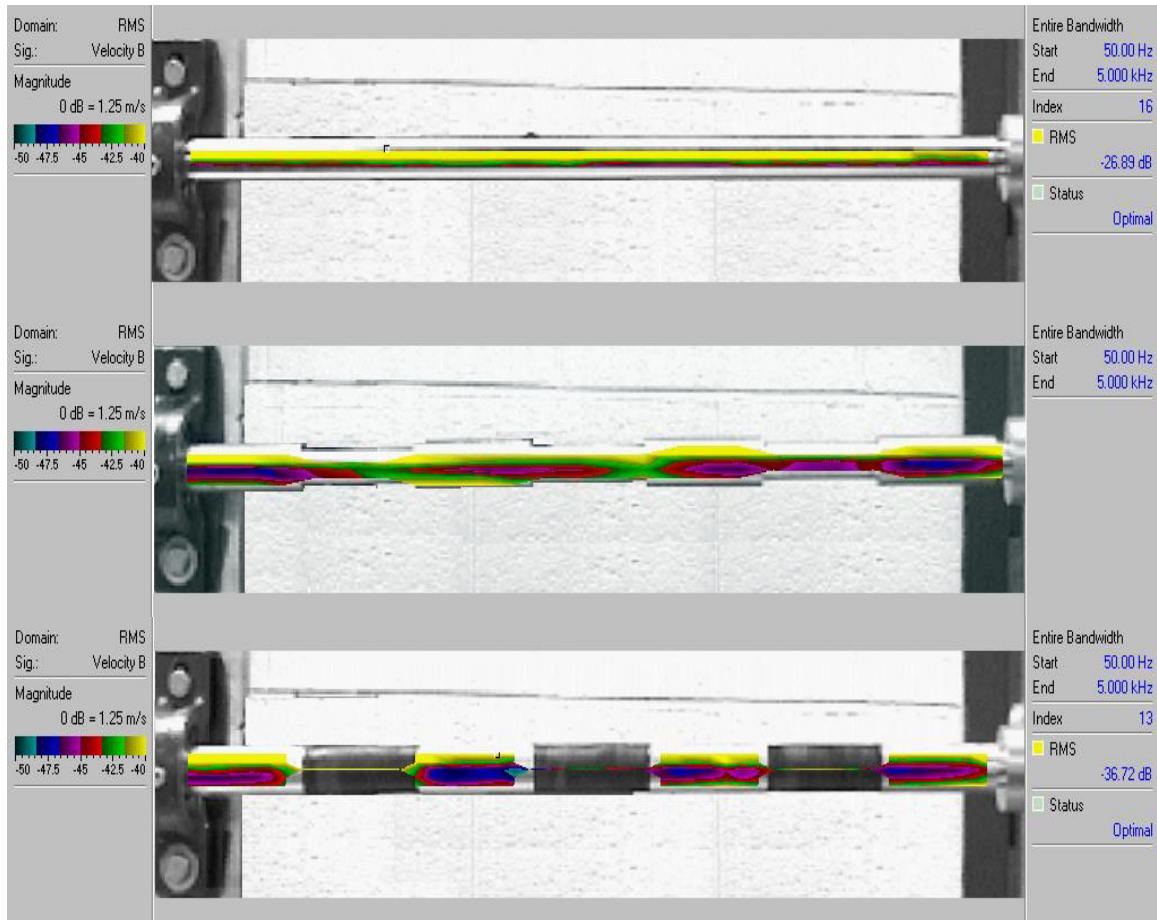


Figure 4.19: Rotating shaft: Frequency response of the periodic profile (solid) and uniform profile (dash).

The vibrometer also gives the average power spectrum of vibration of the scanned mesh of points. Figure (4.20) compares the power spectrum of each shaft with the numerical propagation characteristics with emphasis on the first stop-band. In comparison to the uniform shaft (dashed lines), a broadband attenuation is clearly visible for the rubber-coated shaft (thick solid line). A localized attenuation is difficult to identify in this picture.

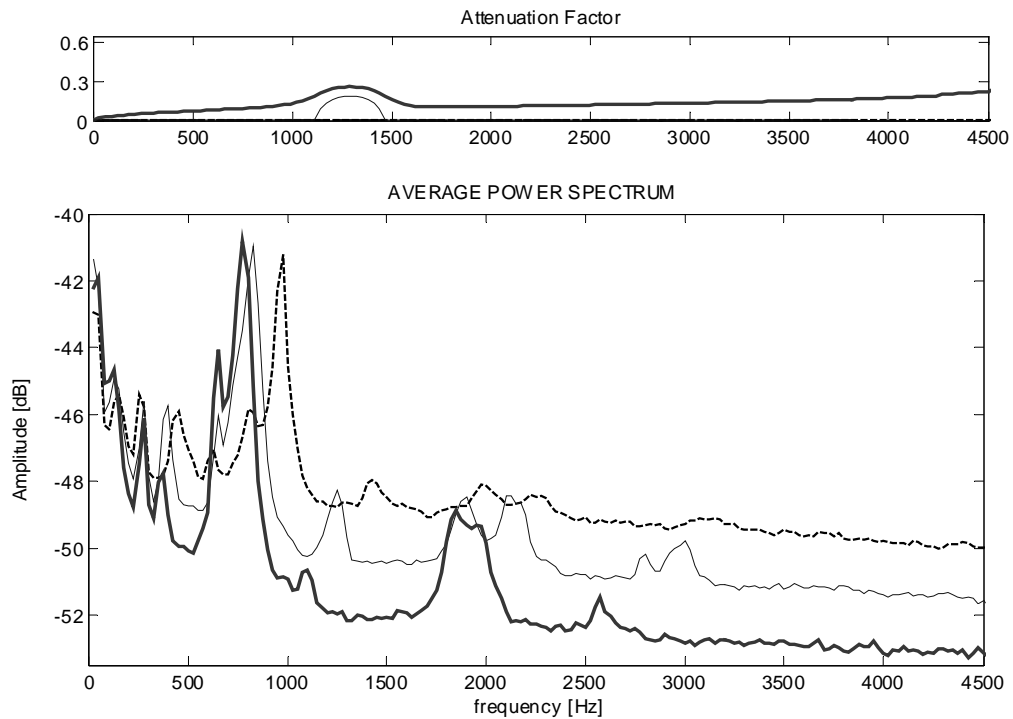


Figure 4.20: Attenuation factor and Average Power Spectrum of the rotating uniform shaft (dash), stepped periodic shaft (thin solid) and rubber-coated shaft (thick solid).

A sharper picture of the actual filtering characteristics of the two periodic profiles can be obtained by applying the Wavelet Transform [Appendix (A1)] to the power spectrum of Figure (4.20).

In the following Figures ((4.21)-(4.22)-(4.23)) red corresponds to the maximum intensity and blue to the lowest.

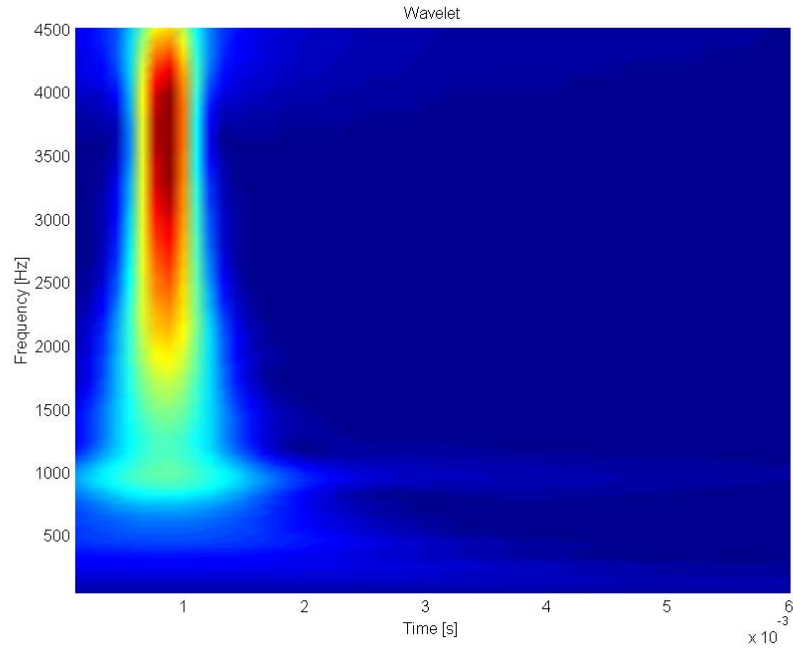


Figure 4.21: Wavelet Transform of the power density for the uniform shaft.

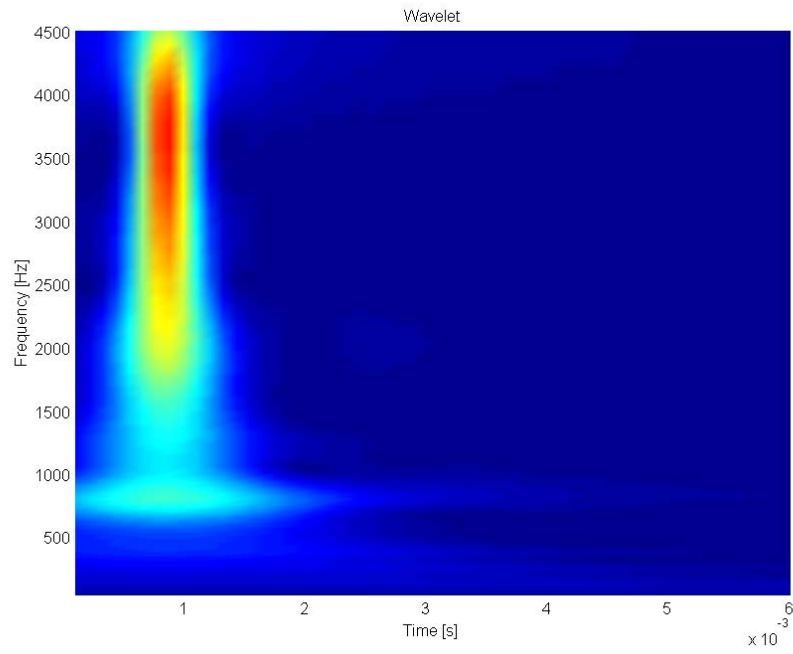


Figure 4.22: Wavelet Transform of the power density for the stepped shaft.

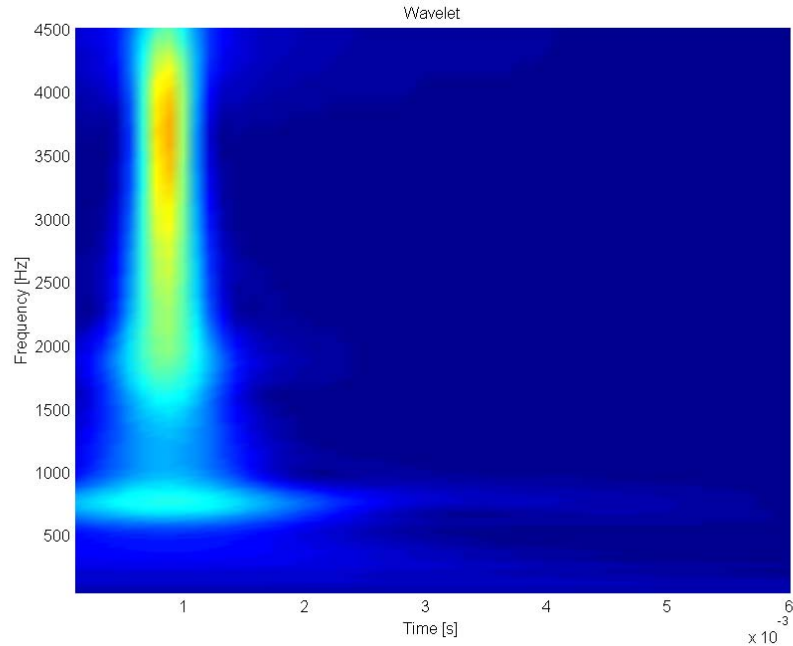


Figure 4.23: Wavelet Transform of the power density for the coated shaft.

Figure (4.21) shows the characteristics of the uniform shaft. The peak at 1kHz is continuously linked to the high frequency region, showing that the energy is evenly distributed along the whole bandwidth.

Figure (4.22) displays the energy distribution of the stepped rotor. It is clear that there is a gap between the higher frequencies and the lowest peak. The energy has redistributed itself away from the stop-band but the overall intensity of vibration is not significantly reduced (red spot)

Figure (4.23) presents the wavelet for the rubber-coated periodic shaft. The energy redistribution is even more evident than for the stepped rotor. First of all, the peak at 1kHz is completely separated from the higher energy spectrum, showing the predicted

local stop-band (Figure 4.20). Then, the absence of red spots exhibits the broadband energy dissipation characteristics typical of the viscoelastic material.

4.9 Conclusions

A simple case was practically investigated, where the rotor consists of a shaft with mass unbalance simply-supported by rigid bearings. The influence of tapered and periodic shapes was investigated to demonstrate their ability reduce vibration at certain frequency ranges (stop-bands). By combining tapered profiles and/or uniform elements and carefully tuning the element length and diameter ratio, the width and spectral location of the stop-bands of a specific rotor can be conveniently altered according to the application.

Experiments were conducted in order to validate the numerical predictions. These experiments confirmed the filtering characteristics of tapered and stepped periodic rotors with respect to cylindrical shafts.

The most important conclusion is that introducing rotation at constant speed does not appreciably affect the wave propagation characteristics of the rotor.

For the case of the tapered shaft, the Campbell diagram was compared to a uniform profile and no consistent changes were noticeable in the dynamic behavior except for a slight decrease of the critical speeds in the case of the tapered rotor.

Finally, the addition of viscoelastic materials to the periodic profiles was proved to be effective in adding a broadband attenuation to the already present local stop bands.

CHAPTER 5: ACTIVE CONTROL OF PERIODIC SHAFTS

5.1 Introduction

The previous chapter investigated the effectiveness of variable geometries on the wave propagation characteristics of rotating shafts. It was determined that periodically stepped shafts and tapered shaft transmit waves only in certain frequency bands (called pass bands) and impede the transmission over other frequency bands (stop bands).

This chapter introduces some active control capabilities to the passive periodic structure in order to enhance the tuning of the spectral width and location of the pass and stop bands.

Active control also allows for intentionally introducing the idea of “aperiodicity” in the periodic structure, in terms of the well-known phenomenon of *localization* [8, 31].

Emphasis is placed on investigating the effect of adding an active constant force on the shaft on the propagation characteristics and the Campbell diagrams.

Furthermore, a feedback active control is implemented to illustrate a broadband localization effect.

In this chapter, an introduction to the possible benefit of actively controlling a rotating periodic shaft has been given in Section 5.1. Section 5.2 addresses the modifications necessary to account for the active control into the mathematical model

that was already discussed in detail in Chapter 4, and describes the properties of the piezo-actuators used in this dissertation.

Section 5.5 compares the theoretical and experimental results obtained in Sections 5.3 and 5.4. It also validates the mathematical model for the controller. The drawn conclusions are summarized in Section 5.6.

5.2 Characteristics of periodic shafts with piezoelectric actuators

The periodic shaft considered in this chapter is an assembly of four aluminum rods (6 in. long, $\frac{3}{4}$ in diameter) connected together by three piezoelectric-actuator disks (0.4 in long, 2 in. diameter). A schematic drawing of the system is shown in Figure (5.1). The piezoelectric disks are included to provide a longitudinal force that is tuned by an electronic controller.

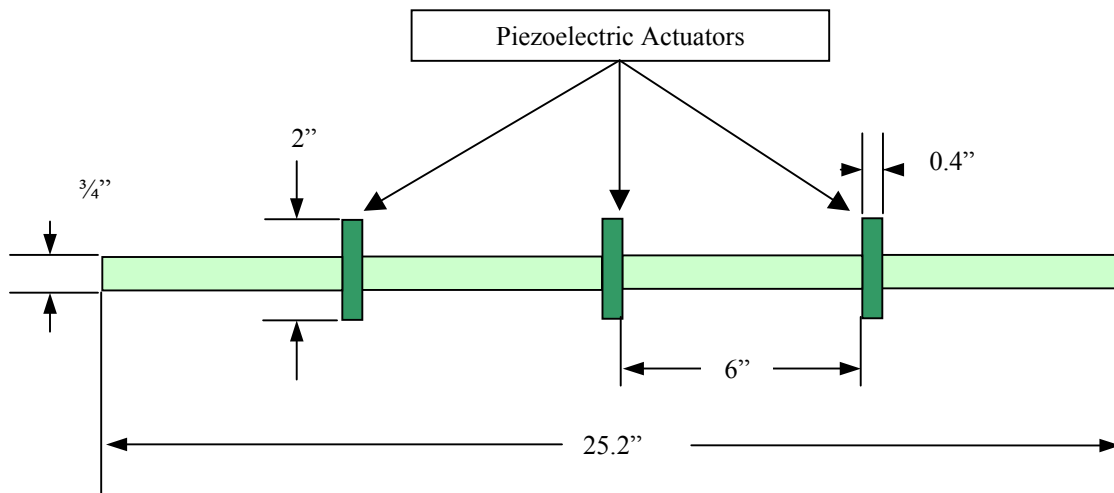


Figure 5.1: Schematic drawing of the active shaft assembly.

The numerical model of the system is derived from equations (4.19). Here, the generic longitudinal force F_0 , appearing in equation (4.19), is substituted by the actuator force F_p , which directly depends on the applied control voltage V_p .

When the control voltage V_p is generated according to a simple displacement and/or velocity control law

$$V_p = -(k_{prop} + k_{deriv}s) w_L \quad (5.1)$$

the formula for the actuator force becomes:

$$F_p = -K_g w_L \quad (5.2)$$

where $K_g = (k_{prop} + k_{deriv}s)$ is the control gain and w_L is the transverse displacement.

5.2.1 Characteristics of the piezoelectric actuators

In the present study, piezoelectric actuators (PCB Piezotronics, Model 712A02) are used. These inertial actuators (Figure (5.2)) provide high efficiency and force output over the middle- to high-frequency audio range. When compared to competing technologies, they are exceptionally efficient in generating dynamic force at frequencies above 150 Hz. When used as part of a closed-loop control system, the actuator provides high-authority canceling force to suppress vibration. Constructed with an all-welded titanium housings and hermetic connectors, they are exceptionally lightweight and they

particularly fit applications such as aircraft, helicopters, marine hulls and isolation mounts.



Figure 5.2: Piezoelectric actuator PCB Piezotronics Model 712A02.

Table (5.1) lists the main geometrical and performance parameters of the actuators.

Table 5.1: Piezo-actuator PCB 712A02 data sheet.

Dynamic Performance	Frequency Range, Hz		150 to 5000	
	Broadband Force (min), lb/volt		0.004	
Static Performance	Clamped Force, lb/volt		0.015	
	Free Displacement, μ in/volt		2.56	
Environmental	Temperature, $^{\circ}$ F		-10 to +150	
Electrical	Capacitance nF		65	
	Resistance ohm (min)		1×10^7	
	Input Voltage (max), Vpk	DC Excitation		-125 to 500
		AC Excitation (off resonance)		± 100
AC Excitation (on resonance)			± 80	
Mechanical	Weight, oz		1.27	
	Size, in	Height	0.4	
		Diameter	2.0	
	Electrical connector		BNC Plug	
	Mounting Thread		10-32 Male	
	Housing Material		Titanium	
	Sealing Type		Welded Hermetic	

Also, Figure (5.3) shows the frequency response characteristics of the actuator authority between 150-5000 Hz with a sensitivity of 0.015 lb/volt and a peak excitation voltage of 100 volts.

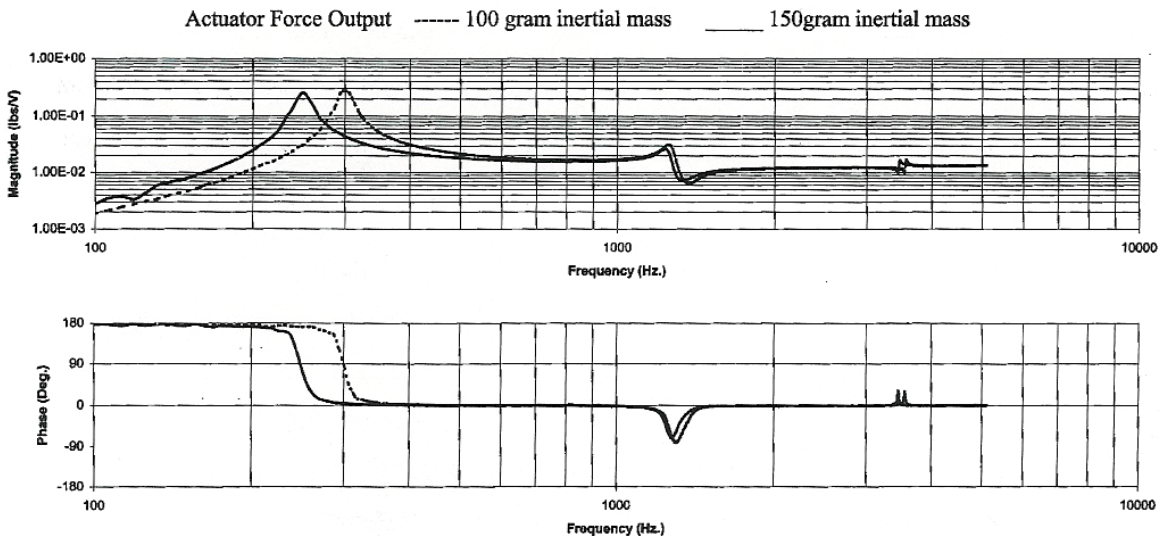


Figure 5.3: Actuator output force characteristics.

5.3 Numerical results

In this section, the propagation characteristics of the periodic shaft are first compared to the ones of the uniform shaft. Then, one piezo-actuator at a time is activated and finally all piezoelectric actuators are excited with constant voltage. Finally, active feedback is implemented on the piezo-actuator at the source location and the characteristics are discussed.

Figure (5.4) compares the frequency response and the Campbell diagrams of the shaft with the three periodic piezoelectric inserts (thick lines) to an equivalent uniform

aluminum shaft (thin lines). The figure demonstrates once again that material and geometry mismatch introduce effective localized energy redistribution in the structure, which does not allow transmission over certain frequency bands. A stop-band between 800Hz and 1500Hz is visible in the frequency response as well as in the Campbell diagrams of the periodic shaft (thick lines). Also, other redistribution can be seen around 3kHz and above 4.5kHz.

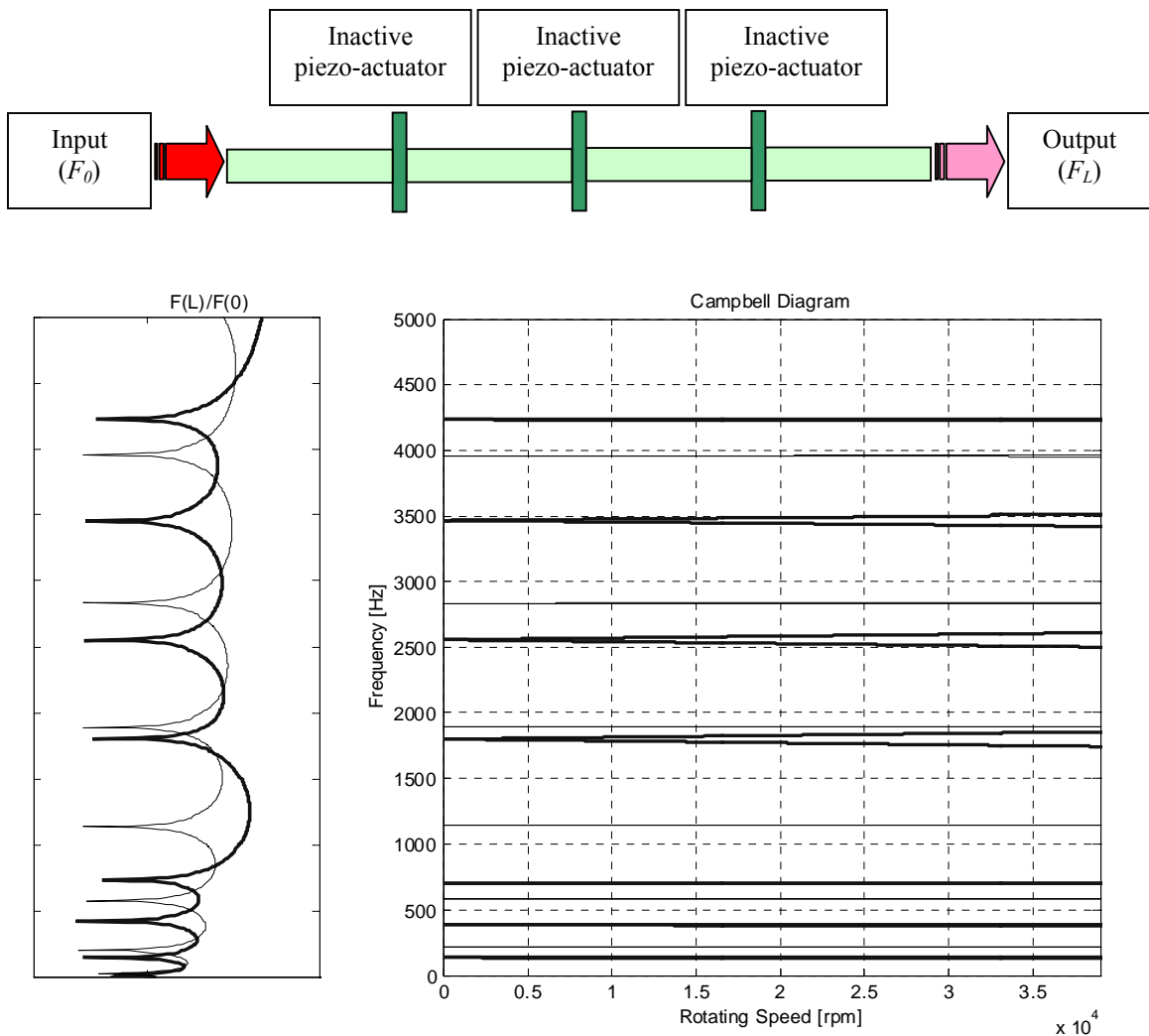


Figure 5.4: Frequency response and Campbell diagram for a uniform shaft (thin) and the passive periodic shaft (thick).

It can be summarized at this point that the critical speeds of rotating periodic shafts move away from the stop-bands and concentrate in the pass-band regions.

Activating the piezoelectric disks can enhance this interesting behavior because we can stretch and more carefully locate the stop-bands in the frequency spectrum. The effect of applying constant forces to the piezo-actuator is first evaluated, as it does not require the use of any sensors on the shaft. Compression and tension stresses are both taken into consideration, as they end up giving different energy redistribution patterns.

Figure (5.5) shows the periodic shaft where only the first piezo-actuator (near the input disturbance location) is activated. Thick lines correspond to the case where the piezo-actuator is subjected to positive voltage and tends to expand, while thin lines denoting the case of a shrinking piezo-actuator. The stop band at 1kHz now extends to 2kHz, while the redistribution effect around 3kHz is improved only when applying negative voltage to the piezo-actuator.

Activating the piezo-actuator at midspan further increases the width of the stop-band at 1kHz. Figure (5.6) shows that compressing the piezo-actuator (thin line) enlarges this stop-band from 800Hz to 2600Hz. A secondary stop-band appears now from 3000Hz to 4200Hz and also between 200Hz and 600Hz.

Figure (5.7) shows the corresponding characteristics when the piezo-actuator at the output location is activated. In this case, the behavior is similar to the characteristics of Figure (5.5) when the input piezo-actuator was active. We can still see a large stop-band between 1-2kHz and some redistribution effect around 3000Hz.

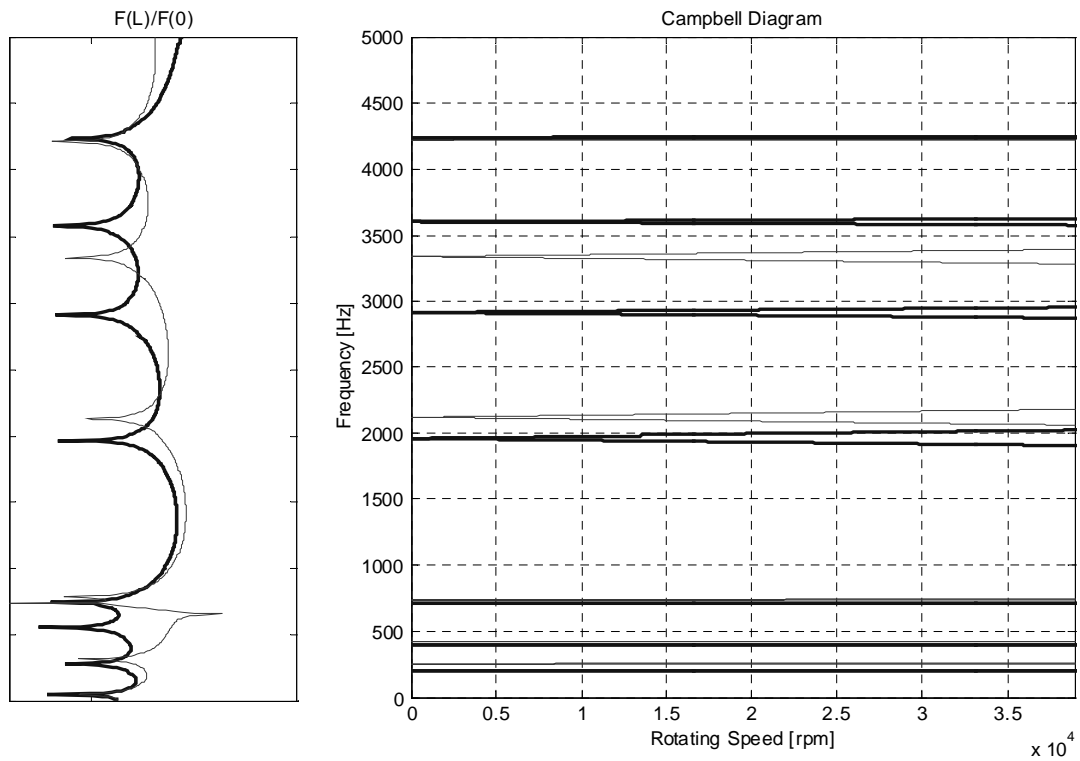
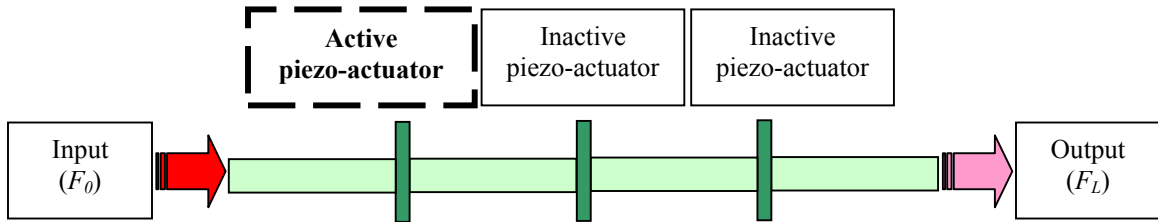


**Figure 5.5: Frequency response and Campbell diagram for the active periodic shaft:
compressive load (thin), tensile load (thick) at input location.**

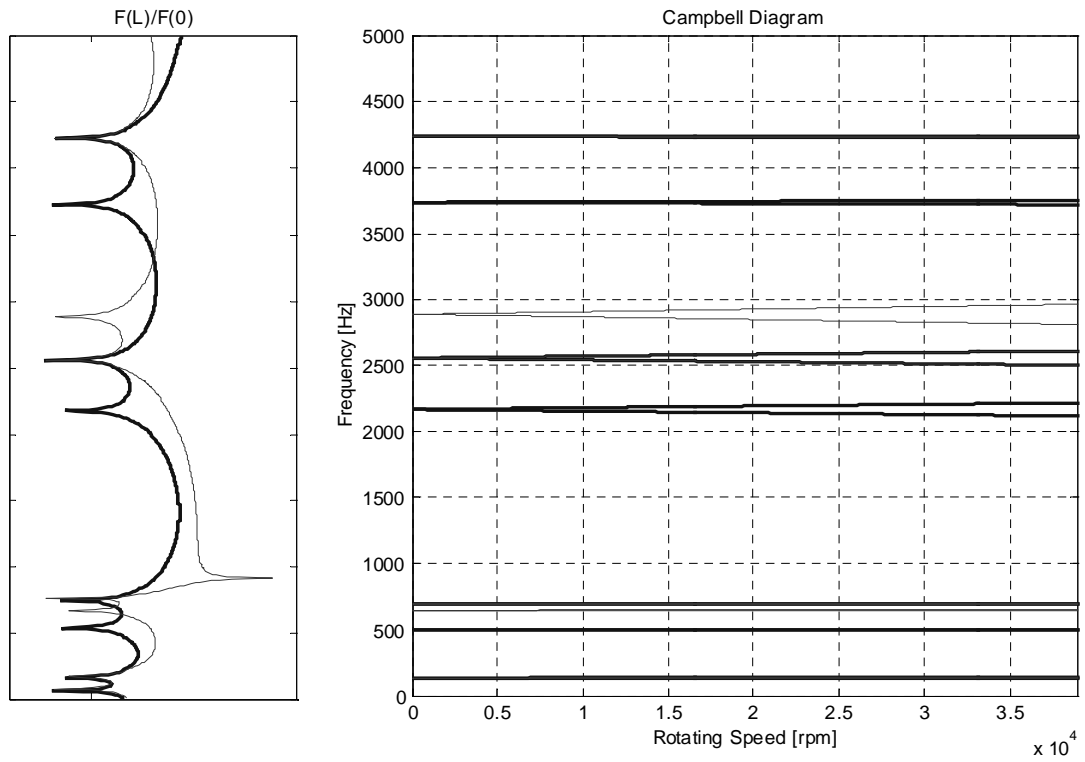
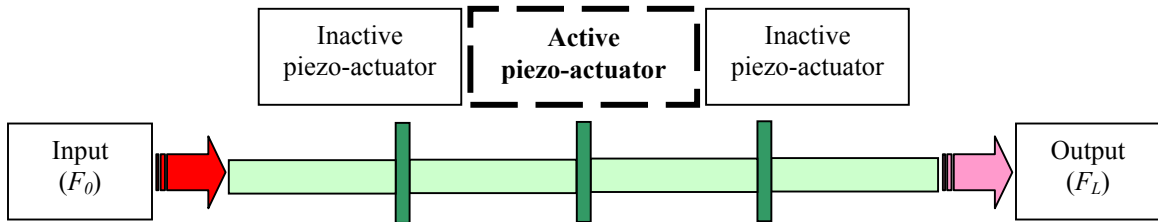


Figure 5.6: Frequency response and Campbell diagram for the active periodic shaft: compressive load (thin), tensile load (thick) at midspan location.

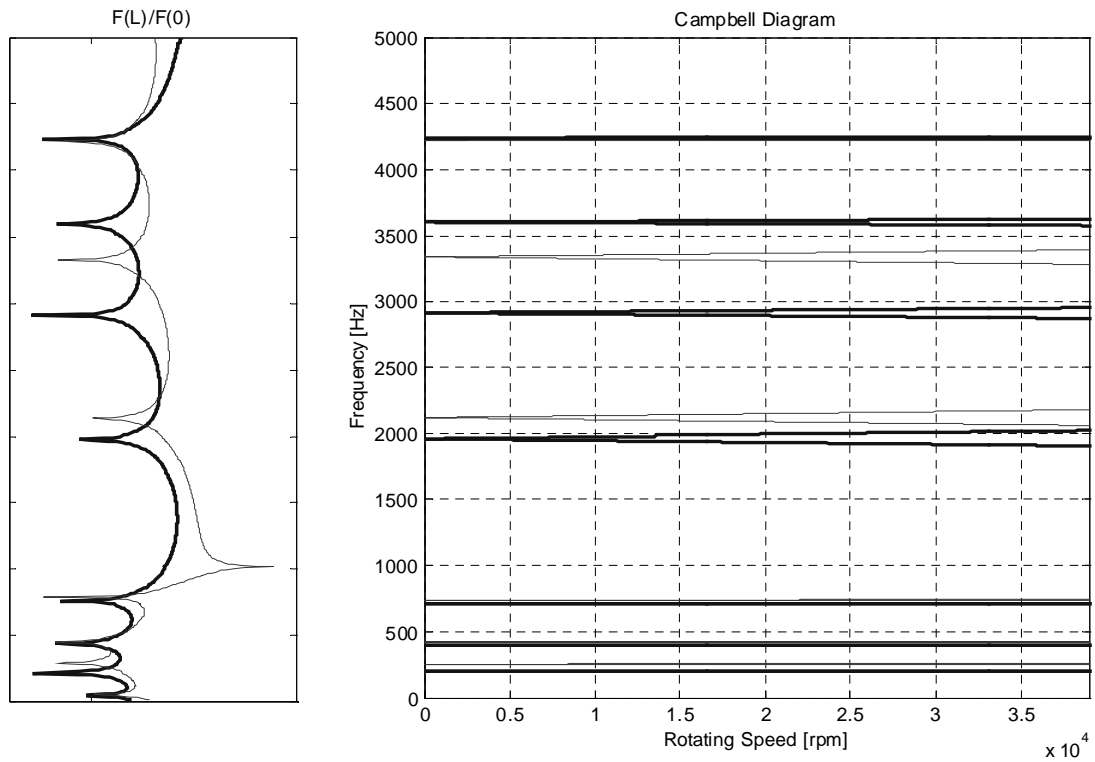
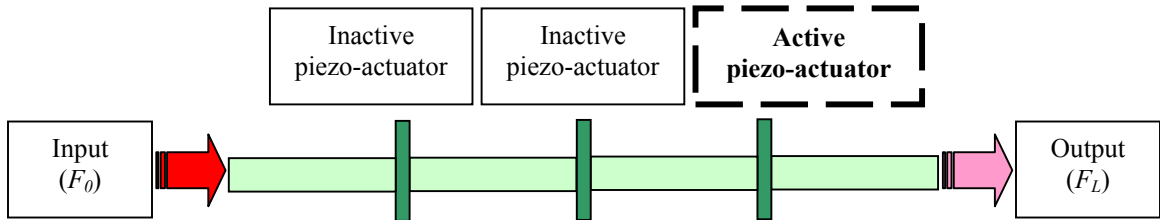


Figure 5.7: Frequency response and Campbell diagram for the active periodic shaft: compressive load (thin), tensile load (thick) at output location.

Figure (5.8) shows the case of a periodic active shaft, when all three piezo-actuator are activated. In this case, the advantage of applying a negative voltage is very

clear: the characteristics of the shaft with shrinking piezo-actuators show a broadband stop-band from 800Hz to 4300Hz. In this region, no critical speeds appear in the Campbell diagram either. When applying a tensile load on the piezo-actuators we can still obtain a wide stop-band between 800 and 2600Hz, but in this case no other secondary stop-bands can be observed.

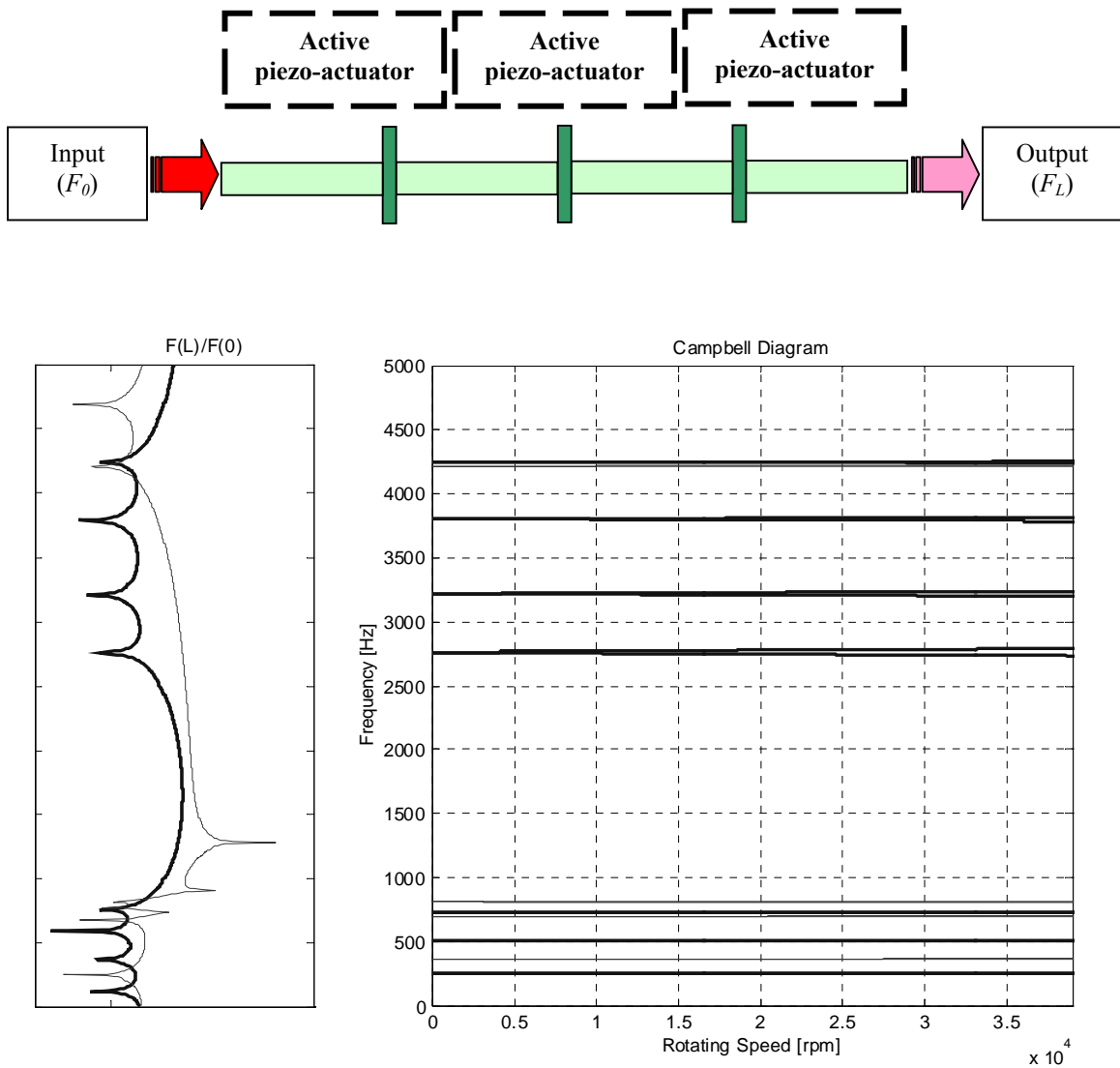


Figure 5.8: Frequency response and Campbell diagram for the active periodic shaft: compressive load (thin), tensile load (thick) at all locations.

We can therefore conclude that applying tensile stresses along the periodic shaft significantly improves the filtering capabilities of the system. The most benefit can be gained when a negative constant voltage actively excites all the actuators.

Another powerful tool that can drastically enhance the vibration confinement of the structure is using an electronic active feedback controller. This technique needs a sensor to be placed on the shaft, which reads the local transmitted disturbance and it feeds it back to the controller. Interfering waves can then be introduced in the structure through the piezo-actuator actuators. This configuration introduces a broadband attenuation effect along the whole frequency spectrum, which makes it very interesting.

The propagation characteristics of the active shaft of Figure (5.9) present a broadband stop-band in addition to the local stop-bands that we can see also in the passive periodic shaft of Figure (5.10).

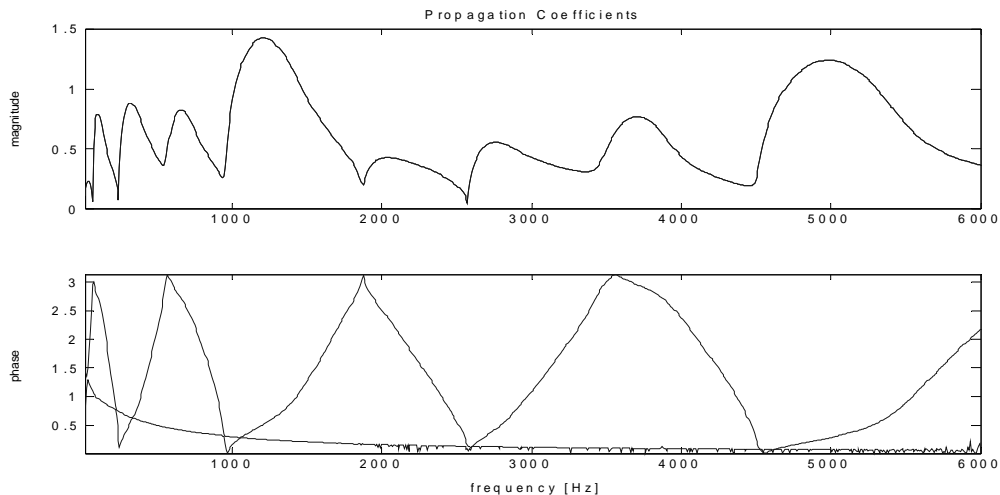


Figure 5.9: Propagation coefficients for the active periodic shaft.

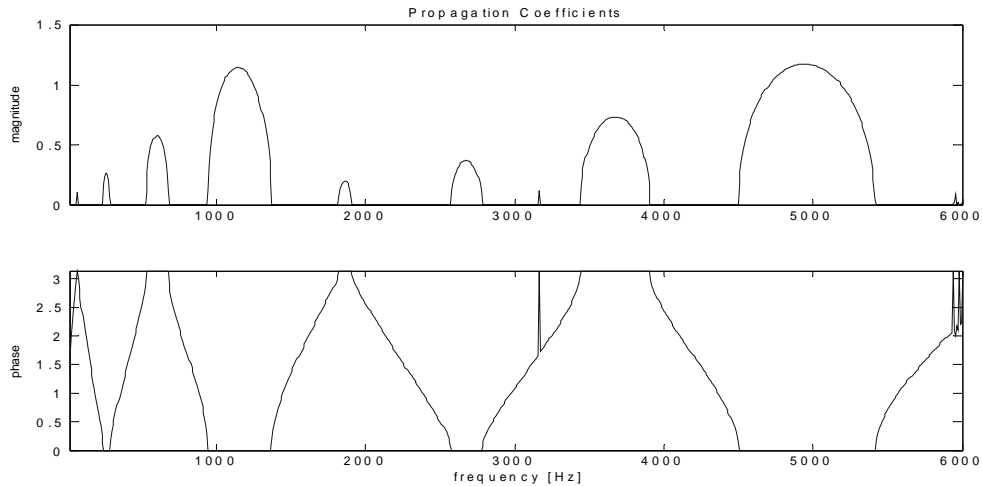


Figure 5.10: Propagation coefficients for the passive periodic shaft.

5.4 Experimental results

The practical inspiration of this set of experiments is to test the transmission of gearbox-motor induced vibrations to the tail rotor of a helicopter through different types of rotating shafts in order to evaluate the filtering capabilities of the periodic shaft with active feedback control.

The setup of the experiment is displayed in Figure (5.11a-b). The output of the epicyclic gearbox (Toledo Gearmotor Co. Model M164-A, ratio $\frac{1}{2}$), driven by an asynchronous AC motor (GE Industrial Systems Model D285, $\frac{1}{2}$ HP@2450rpm). The motor is directly linked to one end of the shaft with a rigid connecting sleeve, while a slip-ring (Airflyte Electronics Model CAY125-10-1, 4 channels) is located at the opposite side of the shaft and carefully aligned to the axis of the motor. A Variac device (Dayton

SCR) allows for adjusting the rotating speed by varying the AC input voltage to the motor.

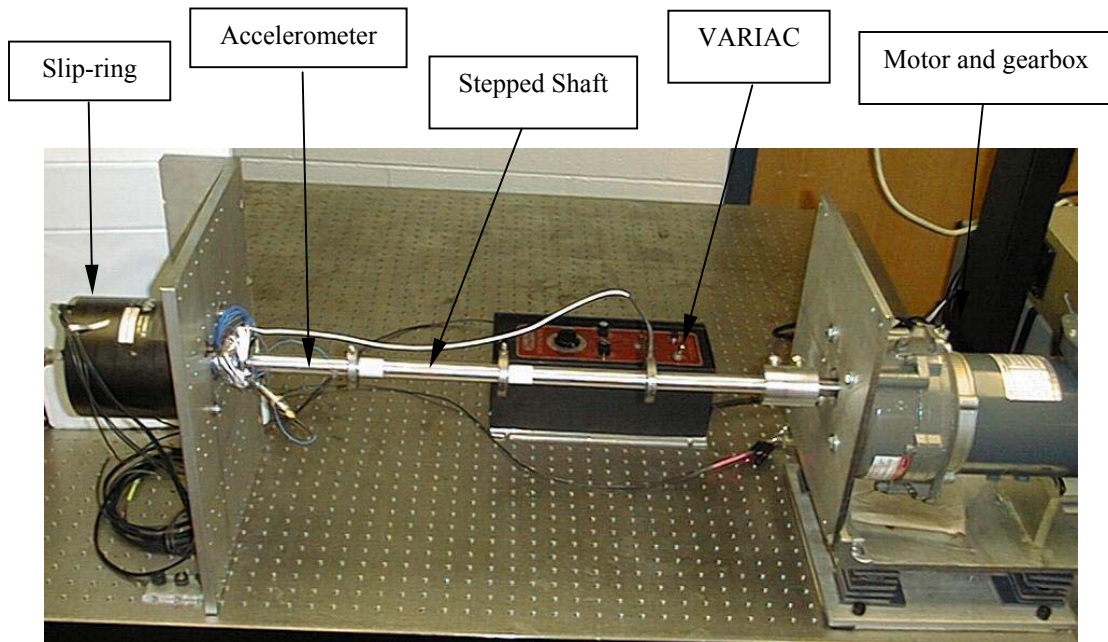


Figure 5.11a: Experiment setup.

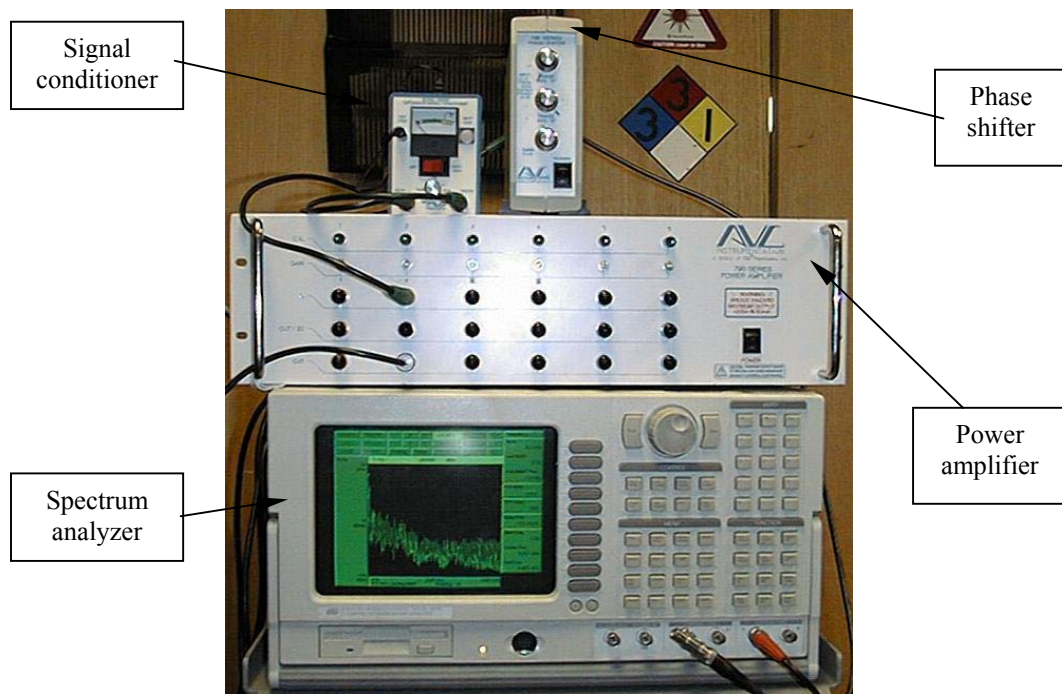


Figure 5.11b: Spectrum analyzer and active controller.

An accelerometer (PCB Model 303A03) is placed at the end of the shaft. Its signal flows through the slip ring to the signal conditioner (PCB Model 480E09) and it is read by the frequency analyzer (SRS Model SR780). The control unit consists of a phase shifter pre-amplifier (PCB Model 780A01) and a high voltage power amplifier (PCB Model 790A06).

Experiments at different rotating speeds are carried out in order to evaluate the effectiveness of the controller over various excitation intensities.

Figure (5.12) shows the experimental frequency response transmitted to the end tip of the shaft in the case when all the actuators are open circuit. Three different rotating speeds are represented in the graph:

- minimum speed: 15% voltage (thick solid line)
- medium speed: 60% voltage (dashed line)
- maximum speed: 100% voltage (thin solid line)

Higher rotating speeds involve a stronger vibration transmission along the structure. However, even under such conditions, it is still easy to identify the spectral regions where the disturbance is free to propagate and the frequency bands where attenuation occurs. By comparing the experimental frequency response to the theoretical propagation constants one can spot two main stop-bands at 800-1400Hz and 4.5-5.3kHz and some more attenuation around 500Hz and between 3.4-3.9kHz.

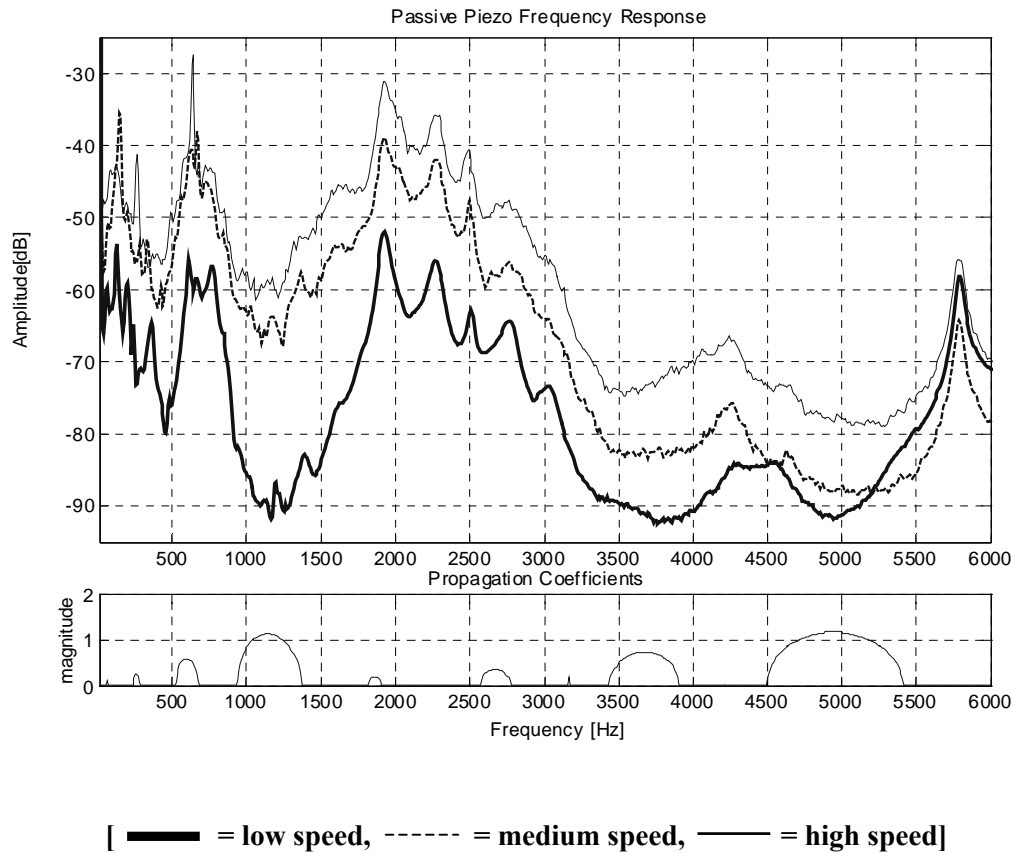


Figure 5.12: Experimental frequency response and propagation coefficients of the passive periodic shaft

Figure (5.13) displays the frequency response of the periodic shaft when the piezo-actuator near the gearbox-motor is actively controlled by a proportional feedback.

It is clear at this point that the controller is capable of consistently reducing the disturbance without being influenced by the rotating speed. By comparing Figure (5.13) to Figure (5.12), one can see that the active shaft rotating at the maximum speed transmits vibration amplitudes similar to those transmitted by the passive shaft when

rotating at the lower possible speed. This accounts for an average broadband reduction of about 15-20 dB.

A broadband attenuation along the whole spectrum of frequencies is evident especially at low rotations. Now the major local stop-bands are effective between 800-1800Hz and between 2.5-5.5kHz. But, because of the nature of the actuators (see Section 5.2.1) it was not possible to obtain good performance below 200Hz.

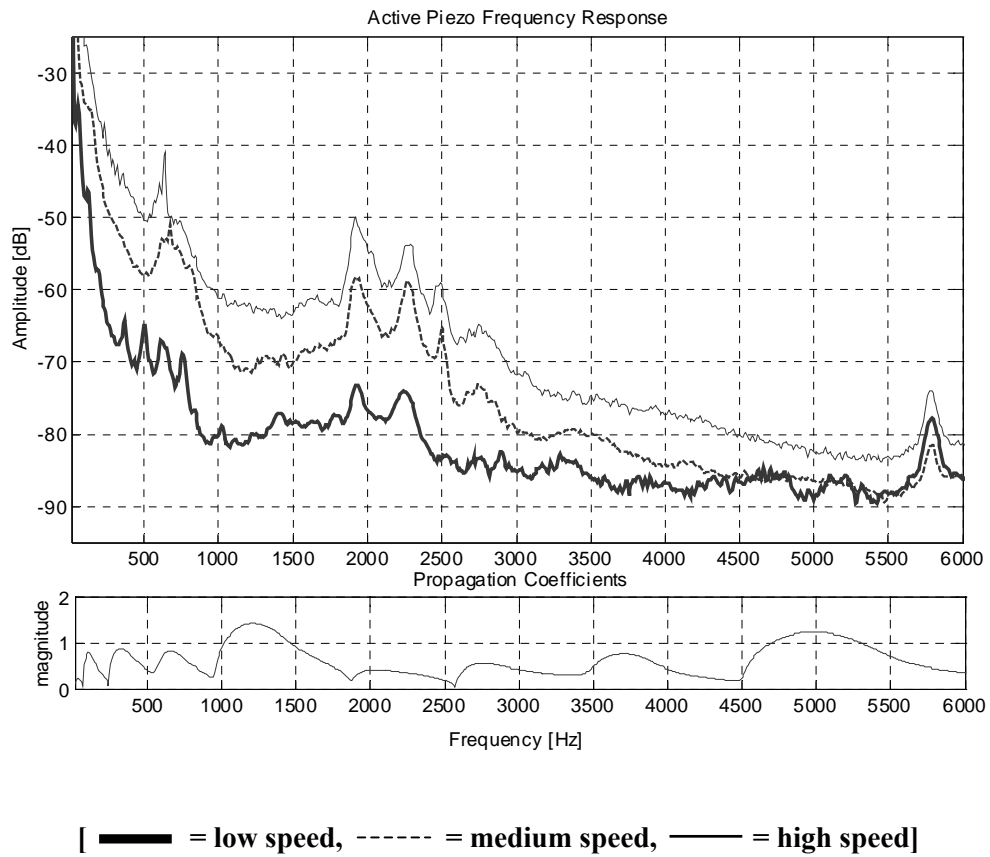


Figure 5.13: Experimental frequency response and propagation coefficients of the active periodic shaft.

More experiments are carried out activating also the piezo-actuator at the midspan and at the end tip of the shaft for different rotation speeds. For all these different cases, the transfer functions of the control gain and phase shift are recorded in order to be able to compare the experimental results with the mathematical model.

Figures (5.14) through (5.16) show the controller transfer function for the three different piezo-actuator positions at all different rotation speeds.

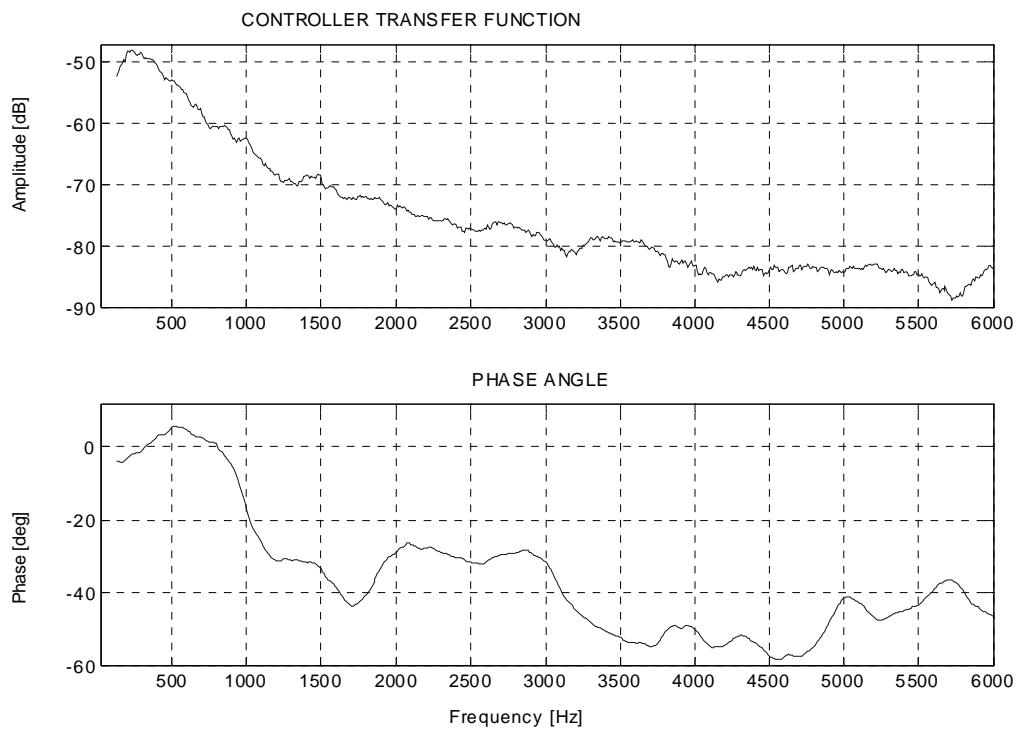


Figure 5.14: Control gain for the active shaft: piezo-actuator at input position.

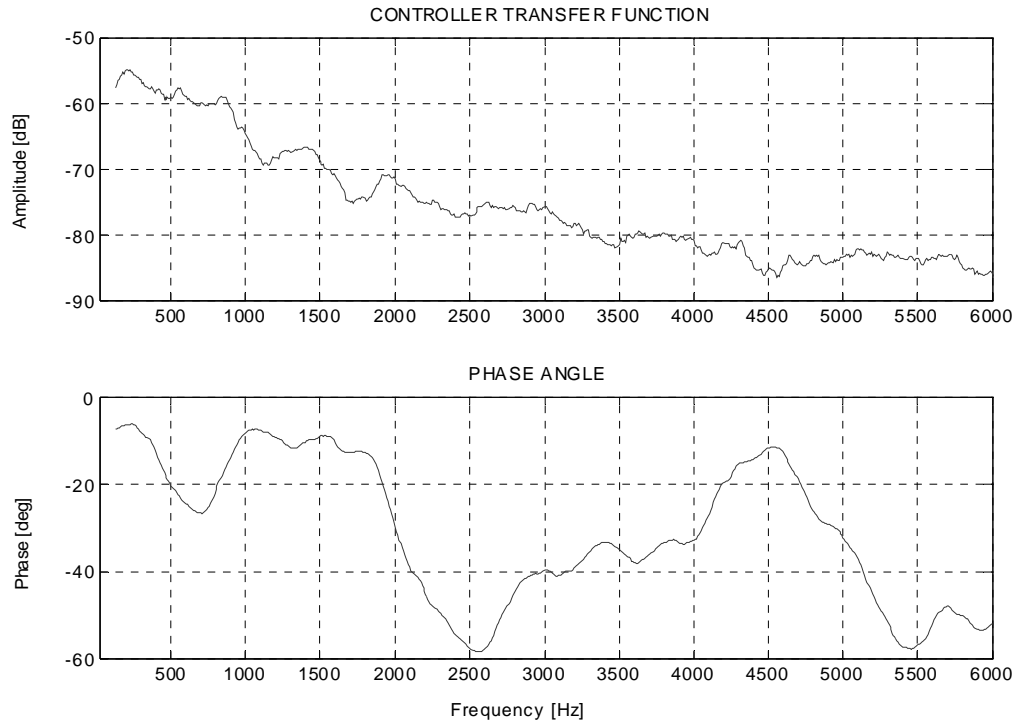


Figure 5.15: Control gain for the active shaft: piezo-actuator at midspan position.

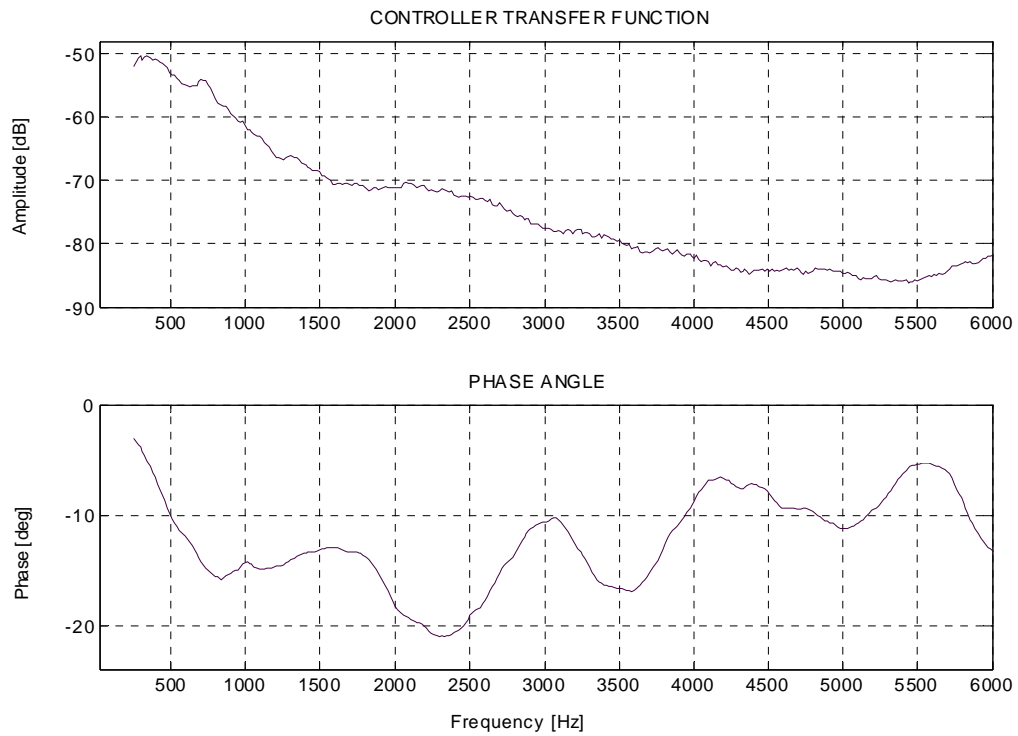


Figure 5.16: Control gain for the active shaft: piezo-actuator at output position.

As it turns out, the optimal gain and phase adjustments are the same for all rotations, so only one curve for each actuator appears in each of the graphs above.

In our case, Figure (5.16), which pictures the output piezo-actuator gain values, is the collocated actuator-sensor system configuration, because the accelerometer is placed right next to it (Figure (5.11a)), but, as we already pointed out in the previous section, there is not much difference in controlling this piezo-actuator or the piezo-actuator at the input side of the shaft. The attenuation levels in all cases are comparable and they all extend from 50 to 90 dB.

5.5 Comparisons between theory and experiments

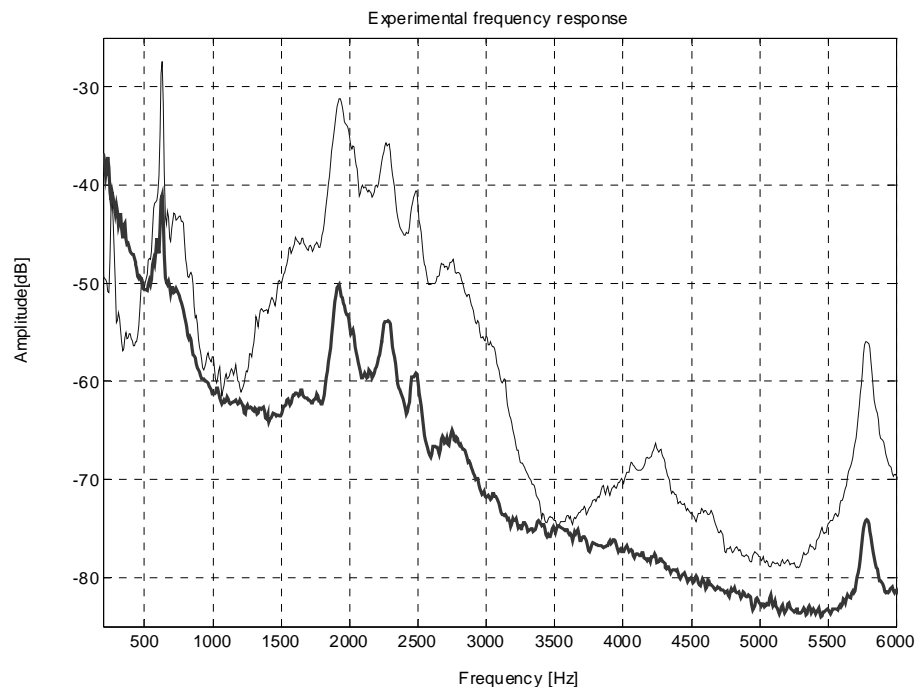


Figure 5.17: Experimental frequency response for the passive shaft (thin) and active shaft (thick): piezo-actuator at input position.

Figure (5.17) compares the effect of the feedback control on the experimental frequency response of the periodic shaft. The implemented proportional active control is very effective in attenuating the peaks of resonance and it also tends to enlarge the effect of the stop-bands: the propagation bands are now restricted to the region between 500-800Hz and at 1800-2700Hz. These results agree also with the theoretical frequency response obtained by substituting the experimental control gain into the FEM model. Figure (5.18), which uses the control law of Figure (5.14), verifies how the controller reduces the pass-bands to the region around 500Hz and in the region between 1.7-2.4kHz in the case when the piezo-actuator at the input position is activated.

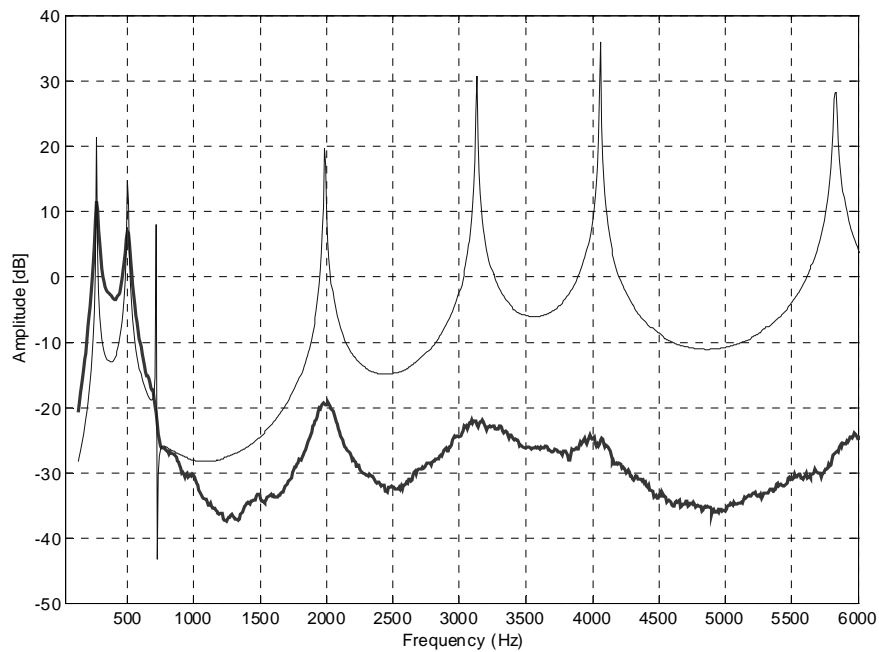


Figure 5.18: Theoretical frequency response for the passive shaft (thin) and active shaft (thick) piezo-actuator at input position.

By substituting the control gain for the other piezo-actuator, one can also test the effectiveness of the remaining actuators on the frequency response.

Figure (5.19) shows that the actuator at midspan only gives a slightly better performance at the lower frequencies below 500Hz, while everything else looks very similar to the previous case. The gain law for this actuator was reported in Figure (5.15).

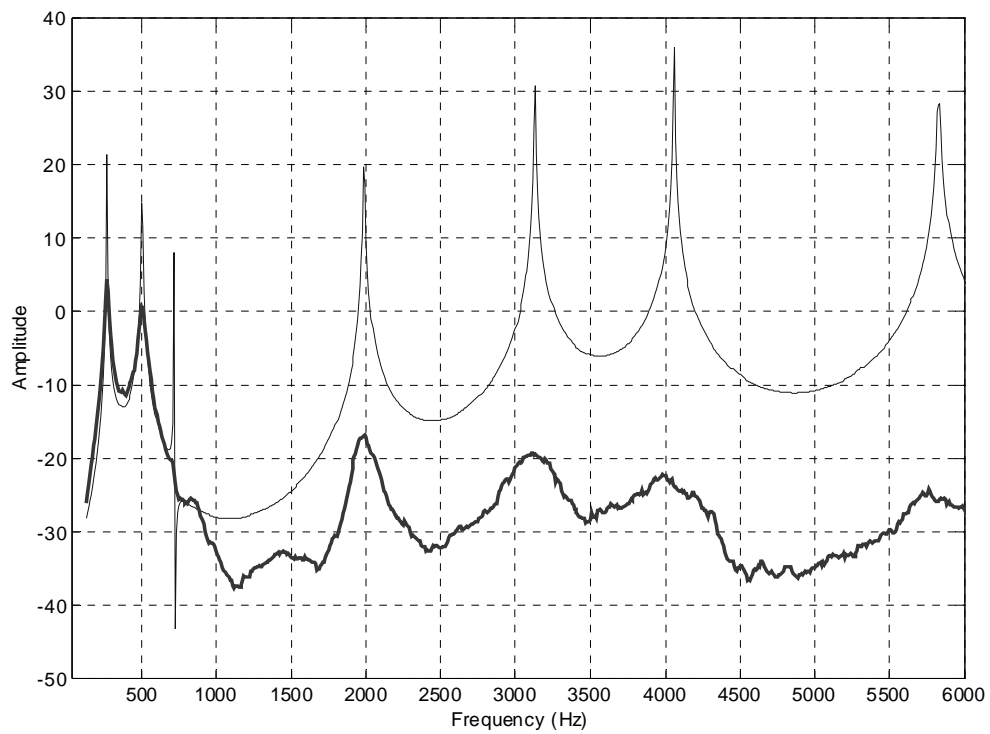


Figure 5.19: Theoretical frequency response for the passive shaft (thin) and active shaft (thick): piezo-actuator at midspan position.

Finally, Figure (5.20) excites the actuator next to the slip ring. This configuration brings the same attenuation pattern as the response of the piezo-actuator at the source location (Figure (5.18)).

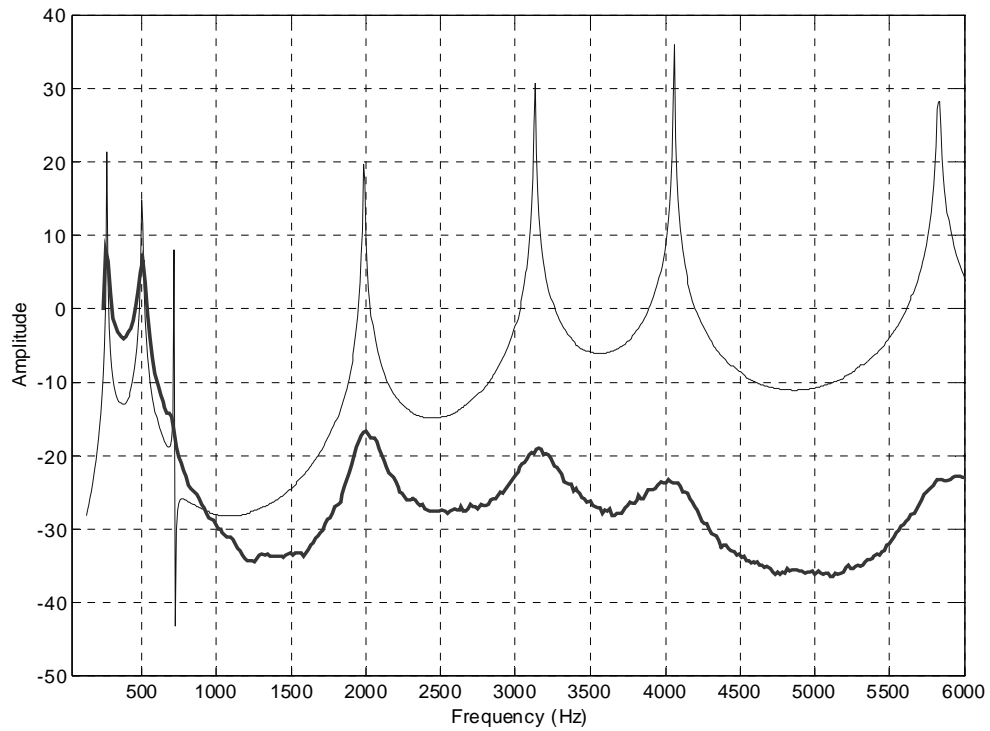


Figure 5.20: Theoretical frequency response for the passive shaft (thin) and active shaft (thick): piezo-actuator at output position.

5.6 Conclusions

In this chapter the performance of a periodic rotating shaft with three actively controlled piezoelectric disks was analyzed. The propagation characteristics, the frequency response and the Campbell diagrams were compared and evaluated. Constant voltage was first applied to the actuators: a tensile load on the shaft appears to be the preferable solution in order to modify the location and width of the stop-bands. The most effective configuration turned out to be when all three piezo-actuator are subjected to negative voltage.

A further enhancement of these results was obtained by applying active feedback control on one of the actuators. No appreciable difference was observed when controlling a collocated system (piezo-actuator at output location) or a non-collocated system (piezo-actuator at input location). It is noticeable that the feedback control only on the input piezo-actuator (Figure (5.18)) gives very similar results in term of energy redistribution as controlling all three piezo-actuator with constant negative voltage (Figure (5.8)), therefore it is understood to be the most cost effective solution for our purposes.

CHAPTER 6: SUMMARY AND RECOMMENDATIONS

6.1 Summary

In this work, we developed a theoretical method was developed based on the “Transfer Matrix” Formulation and the Wavelet Transforms that effectively investigates the influence of periodicity, variable geometry and graded material properties on the wave propagation characteristics of rods, shells and rotating shafts. Several experiments were carried out in order to verify the numerical predictions, and the Wavelet Transform proved to be a very powerful tool to uniquely identifying and compare the energy spectral distribution in the time-frequency domain.

It can be summarized here that, in the case of longitudinal wave-guides, tapered profiles introduce a *cutoff frequency* below which no disturbance can travel in the structure, and the main parameter that affects the spectral location of this cutoff frequency is the ratio between the cross sections at the end of the element. Rods with tapered profile shift the energy spectrum to a higher frequency range and hence behave as a simple high-pass mechanical filter.

Thin shells can be modeled as two-dimensional wave-guides, where the propagation of the longitudinal waves can interfere with the flexural (radial) waves. A much richer scenario comes out as a result of this. Variations of the wall thickness,

medium radius and element length of the shell can effectively filter out undesirable bands of frequencies from the longitudinal and/or the transverse wave patterns. Still, the principal parameter that influences the width of the stop bands is the ratio between the cross sections at the two ends of the shell element.

It was also observed that there are no significant improvements in the propagation characteristics when more exponential profiles were implemented instead of simple linear polynomials.

Very similar results were obtained with *functionally graded materials*, and it is easier to obtain much higher ratios. Finally, by combining the two effects one can obtain the flexibility needed for some very demanding applications.

Different types of periodic taper configurations proved to have complementary effects on the wave characteristics. Combinations of these complex geometries (*bi-periodic tapered cells*) produce the most effective energy redistribution.

For the case of simple rotors (axisymmetric shaft with mass unbalance and rigid bearings), tapered and periodic profiles were tested in their ability to redistribute the energy away from specific frequency ranges (stop-bands). The most important observation is that introducing rotation at constant speed does not appreciably affect the wave propagation characteristics of the rotor. We also demonstrated that by carefully tuning the element length and diameter ratio of periodic elements one has the possibility to conveniently shape and locate the stop-bands of a specific rotor.

The Campbell diagrams of tapered and periodic shafts showed that the propagation characteristics of the static rotor extend to the case when the shaft is rotating

at constant speed: the critical speeds move away from the stop-bands and concentrate around the regions of frequencies that allow transmission (pass-bands).

Also, the addition of viscoelastic materials to periodic profiles has proved to have a great potential in adding broadband attenuation to the already present local stop bands.

Finally, we established that the application of active constant forces on the shaft enlarges the regions of interference especially when the shaft is subjected to tensile forces. Active feedback control of one actuator introduces significant broadband attenuation that adds up to the local stop-bands and most effectively proved to trap the vibrational energy at the source location (localization effect).

6.2 Recommendations

Two areas of improvement of the results accomplished can certainly be identified: a more detailed investigation of viscoelastic inserts in combination with active control would further improve the broadband attenuation of vibrations, and also the implementation of FGM needs to be fully investigated because they would require no external source of power.

APPENDIX A1: The Wavelet Transform

The Wavelet Transform (WT) of a signal $x(t)$ is an example of a time-scale decomposition obtained by dilating and translating along the time axis a chosen analyzing function (wavelet) [9]. The integral or continuous WT relative to some basic wavelet $\psi(t)$ is defined as:

$$W_{\psi}(a,b) = \frac{1}{\sqrt{a}} \int_{-\infty}^{+\infty} x(t) \cdot \psi^* \left(\frac{t-b}{a} \right) dt \quad (\text{A.1})$$

where b is a translation parameter used for positioning the function $\psi(t)$ over the time domain, and $a > 0$ is a scaling parameter dilating or contracting the function $\psi(t)$. The WT provides a flexible time-frequency window, which automatically narrows when observing high frequency phenomena and widens when studying low frequency components [9]. The wavelet function used in this work is the Morlet wavelet, defined in the time domain as:

$$\psi(t) = e^{-\frac{t^2}{2}} \cdot e^{j \cdot \omega_w \cdot t} \quad (\text{A.2})$$

The Morlet wavelet is a sinusoidal function, oscillating at the frequency ω_w , modulated by a gaussian envelope of unit variance. Being composed of a modulated sinusoidal function, the Morlet wavelet is well suited for reproducing and analyzing signals in many applications and particularly in this work.

As signal decomposition, the WT cannot be directly compared to a time-frequency representation. However, it can be shown that b represents a time parameter and that the dilation parameter a is strictly related to frequency [37 and 43]. In the frequency domain, the Morlet wavelet becomes:

$$\Psi(\omega) = \sqrt{2 \cdot \pi} \cdot e^{-\frac{1}{2}(\omega - \omega_w)^2} \quad (\text{A.3})$$

Equation (A.3) shows that the frequency domain formulation of the Morlet wavelet is a gaussian function centered at $\omega = \omega_w$. Its dilated version is expressed as:

$$\Psi(a \cdot \omega) = \sqrt{2 \cdot \pi} \cdot e^{-\frac{1}{2}(a \cdot \omega - \omega_w)^2} \quad (\text{A.4})$$

whose maximum is located at $a \cdot \omega = \omega_w$. Since $\omega_w = 1.875\pi$ is a fixed parameter defining the wavelet function [37], the center of the gaussian curve and therefore the frequency of the analysis can be located by changing the dilation parameter as follows:

$$\omega = \frac{\omega_w}{a} \quad (\text{A.5})$$

The scale parameter can be hence considered as the inverse of a frequency parameter and thus the WT can be classified as a time-frequency transform.

An alternative formulation of the continuous WT can be obtained transforming both the signal $x(t)$ and the wavelet function $\psi(t)$ in the frequency domain:

$$W_g(a, b) = \sqrt{a} \cdot \int_{-\infty}^{+\infty} X(\omega) \cdot \Psi^*(a \cdot \omega) \cdot e^{j \cdot \omega \cdot b} \cdot d\omega \quad (\text{A.6})$$

being $X(\omega)$ and $\Psi^*(a\omega) \cdot e^{j\omega_0 b}$ the Fourier transforms of $x(t)$ and $\psi^*\left(\frac{t-b}{a}\right)$ respectively.

This formulation of the WT can be expressed in a discrete form as:

$$W(m, n) = \sqrt{m \cdot \Delta a} \sum_n X(f_n) \cdot \Psi^*(m \cdot \Delta a \cdot f_n) \cdot e^{j \cdot 2 \cdot \pi \cdot f_n \cdot n \cdot \Delta b} \quad (\text{A.7})$$

where f_n is the discrete frequency and Δa and Δb are discrete increments of dilation and translation parameters. Equation (A.7) allows an easy implementation of the WT. The frequency domain formulation of the WT is particularly convenient when the signal to be analyzed is expressed in the frequency domain.

REFERENCES

1. **Abrate, S.**, “Vibration of Non-uniform Rods and Beams”, *Journal of Sound and Vibration* **185**(1), 185-189, 1995.
2. **Agnes, G.**, “Piezoelectric Coupling of Bladed-Disk Assemblies”, *Proc. Of Smart Structures and Materials Conference on Passive Damping*, Newport Beach, CA, SPIE-3672, pp. 94-103, 1999.
3. **Asiri, S.**, *Isolation of helicopter gearbox vibration using periodic support struts*, Ph.D. Thesis, Department of Mechanical Engineering, University of Maryland, 2003.
4. **Banerjee, J.R., and Williams, F.W.**, “Exact Bernoulli-Euler Dynamic Stiffness Matrix for a Range of Tapered Beams”, *International Journal for Numerical Methods in Engineering* **21**, 2289-2302, 1985.
5. **Bapat, C. N.**, “Vibration of Rods with Uniformly Tapered Sections”, *Journal of Sound and Vibration* **185**(1), 185-189, 1995.
6. **Baz, A.**, “Active Control of Periodic Structures”, *ASME – Journal of Vibration and Acoustics* **123**, 472-479, 2001.
7. **Brillouin, L.** Wave propagation in periodic structures, 2nd ed., Dover, 1946.
8. **Cai, G and Y. Lin**, “Localization of Wave Propagation in Disordered Periodic Structures”, *AIAA Journal*, **29**, 3, pp. 450-456, 1990.
9. **Chui, C. K.**, *Wavelets Analysis and Applications: An Introduction to Wavelets*. Vol. 1, Academic Press Inc., 1992.

10. **Curti, G., Raffa, F. A., and Vatta, F.**, “Steady-State Unbalance Response of Continuous Rotors on Anisotropic Supports”, *ASME – Vibration of Rotating Systems*, **60**, 27-34, 1993.
11. **Doyle, J. F.**, “A Spectrally Formulated Finite Element for Longitudinal Wave Propagation”, *Journal of Modal Analysis* **29**, 1-5, 1988.
12. **Eisenberger, M.**, “Exact longitudinal vibration Frequencies of a Variable Cross-section Rod”, *Applied Acoustics* **34**, 123-130, 1991.
13. **Flugge, W.**, *Stresses in Shells*. Springer-Verlag, Berlin, 1973.
14. **Genta, G.**, *Vibrations of Structures and Machines: practical aspects*, Springer-Verlag, New York, 1995.
15. **Graff, K. F.**, *Wave Motion in Elastic Solids*. Dover Publications, New York, 1975.
16. **Gunter, E. J., and Trumpet, P. R.**, “The Influence of Internal Friction on the Stability of High Speed Rotors with Anisotropic Supports”, *ASME – Vibr. 2*, **69**, 1-13, 1969.
17. **Han, R. P. S., and Liu, J. D.**, “Free Vibration Analysis of a Fluid-Loaded Variable Thickness Cylindrical Tank”, *Journal of Sound and Vibration* **176**(2), 235-253, 1994.
18. **Irie, T., Yamada, G., and Kaneko, Y.**, “Free Vibration of a Conical Shell with Variable Thickness”, *Journal of Sound and Vibration* **82**, 83-94, 1982.
19. **Kang, B., and Tan, C. A.**, “Elastic Wave Motion in an Axially Strained, Infinitely Long Rotating Timoshenko Shaft”, *Journal of Sound and Vibration* **213**(3), 467-482, 1998.

20. **Kang, J. H., and Leissa, A. W.**, “Three-Dimensional Vibration of Hollow Cones and Cylinders with Linear Thickness Variations”, *Journal of Acoustical Society of America* **106**(2), 748-755, 1999.
21. **Kim, W., Argento, A., and Scott, R. A.**, “Free Vibration of a Rotating Tapered Composite Timoshenko Shaft”, *Journal of Sound and Vibration* **226**(1), 125-147, 1999.
22. **Kolsky, H.**, *Stress waves in solids*, Dover Publications, New York, 1963.
23. **Kramer, E.**, *Dynamics of Rotors and Foundations*, Springer-Verlag, New York, 1993.
24. **Kuang, W, and Tan, C. A.**, “Vibration of a Rotating Stepped Beam by the Distributed Transfer Function Method”, *ASME – Vibration of Rotating Systems*, **60**, 219-227, 1993.
25. **Kumar, B. M., and Sujith, R. I.**, “Exact Solutions for the Longitudinal Vibration of Non-Uniform Rods”, *Journal of Sound and Vibration* **207**(5), 721-729, 1997.
26. **Lalanne, M., and Ferraris, G.**, *Rotordynamics Prediction in Engineering*, John Wiley, New York, 1998.
27. **Lau, J. H.**, “Vibration Frequencies for a non-uniformed Beam with End Mass”, *Journal of Sound and Vibration* **97**, 513-521, 1984.
28. **Leissa, A. W., and So, J.**, “Three-Dimensional Vibration of Hollow Cones and Cylinders with Linear Thickness Variations”, *Journal of Acoustical Society of America* **106**(2), 748-755, 1999.

29. **Leissa, A. W.**, *Vibrations of Shells*. (NASA SO-288), U.S. Government Printing Office, Washington D.C., 1973.
30. **Li, Q. S.**, “Exact Solutions for Free Longitudinal Vibration of Non-Uniform Rods” *Journal of Sound and Vibration* **234**(1), 1-19, 2000.
31. **Luongo, A.**, “Mode Localization by Structural Imperfections in One-Dimensional Continuous Systems”, *Journal of Sound and Vibration*, **155**, 2, pp. 249-271, 1992.
32. **Mead, D. J.** “Vibration Response and Wave Propagation in Periodic Structures” *ASME Journal of Engineering for Industry*, **93**, pp. 783-792, 1971.
33. **Mead, D. J. and Markus, S.** “Coupled Flexural-Longitudinal Wave Motion in a Periodic Beam” *J. of Sound and Vibration*., **90**, 1, pp. 1-24, 1983.
34. **Meirovich, L.**, *Principles and Techniques of Vibrations*, Prentice Hall, New Jersey, 1997.
35. **Millott, A., and Welsh, W.**, “Helicopter Active Noise and Vibration Reduction” *25th European Rotorcraft Forum*, pp. G23 (1)-G23 (13), September 14-16, 1999.
36. **Murphy, B. T.**, “Improved Rotordynamic Unbalance Response Calculations using the Polynomial Method”, *ASME – Vibration of Rotating Systems*, **60**, 35-42, 1993.
37. **Onsay, T., and Haddow, A. G.**, “Wavelet Transform Analysis of Transient Wave Propagation in a Dispersive Medium”, *Journal of Acoustical Society of America* **95**(3), 1441-1449, 1994.
38. **Orris, R. M., and Petyt, M.**, “A Finite Element Study of Harmonic Wave Propagation in Periodic Structures”, *J. of Sound and Vibr.* **33**(2), 223-237, 1974.

39. **Penzes, L. E., and Padovan, J.**, “Maxi-Element Analysis for Free Vibration of Orthotropic Shells of Revolution”, *Journal of Sound and Vibration* **54**(2), 249-26, 1977.
40. **Rankine, W. J. M.**, “On the Centrifugal Force of Rotating Shafts”, *The Engineer*, 27, April 9, 1869.
41. **Richards, D. A.**, *Passive Gear Mesh Vibration Reduction Using an Isotropic Periodic Shaft*, M.S. Thesis, Department of Aerospace Engineering, University of Maryland, 2000.
42. **Roy, A. and R. Plunkett**, “Wave Attenuation in Periodic Structures”, *J. of Sound and Vibration*, **114**, 3, pp. 395-411, 1986.
43. **Ruzzene, M., Gu, Z., and Baz, A.**, “Wavelet Analysis of Wave Propagation in Shells with Periodic Stiffeners”, *Journal of Sound and Vibration*, (to be published).
44. **Scott, R. A., and Kim, W.**, “Harmonic Wave Propagation in an Infinite Rotating Composite Timoshenko Shaft”, *Journal of Sound and Vibration*, **243**(4), 763-768, 2001.
45. **Sen Gupta, G.**, “Natural Flexural Waves and the Normal Modes of Periodically-Supported Beams and Plates”, *J. of Sound and Vibration*, **13**, pp. 89-111, 1970.
46. **Sivadas, K. R., and Ganesan, N.**, “Axisymmetric Vibration Analysis of Thick Cylindrical Shell with Variable Thickness”, *Journal of Sound and Vibration* **160**(3), 387-400, 1993.
47. **Sivadas, K. R., and Ganesan, N.**, “Free Vibration of Circular Cylindrical Shells with Axially Varying Thickness”, *J. of Sound and Vibration* **147**(1), 73-85, 1991.

48. **Staple, A. and Wells, D.**, "The Development and Testing of an Active Control of Structural Response System for the EH101 Helicopter," *Proceedings of the 16th European Rotorcraft Forum*, pp. III.6.1.1.
49. **Stoneking, J. E.**, "Free Vibrations of Shells of Revolution with Variable Thickness" *Journal of Nuclear Engineering and Design* **24**, 314-321, 1973.
50. **Suzuki, K, Kosawada, T., Shikanai, G., and Hayashi, K.**, "Vibrations of Rotating Circular Cylindrical Shell with Varying Thickness", *Journal of Sound and Vibration* **166**(2), 267-282, 1993.
51. **Suzuki, K, Takahashi, S, Anzai, E., and Kosawada, T.**, "Vibration of a Cylindrical Shell with Variable Thickness Capped by a Circular Plate", *JSME* **26**(220), 1775-1782, 1983.
52. **Takahashi, S., Suzuki, K., and Kosawada, T.**, "Vibrations of a Conical Shells with Variable Thickness", *JSME* **29**, 4306-4311, 1986.
53. **Takahashi, S., Suzuki, K., Anzai, E., and Kosawada, T.**, "Axisymmetric Vibrations of a Conical Shells with Variable Thickness", *JSME* **25**, 1771-1780, 1982.
54. **Tan, C. A., and Kang, B.**, "Wave Reflection and Transmission in an Axially Strained, Rotating Timoshenko Shaft", *Journal of Sound and Vibration* **213**(3), 483-510, 1998.
55. **Wang, G. Y.**, *Vibration of Building and Structures*. Science and Technology Press, Beijing, 1998.